IMAGING OF SPECIAL NUCLEAR MATERIALS USING MONOCHROMATIC GAMMA RAYS FROM LOW-ENERGY NUCLEAR REACTIONS

A Dissertation
Presented to
The Academic Faculty

By

Paul Brian Rose Jr

In Partial Fulfillment
of the Requirements for the Degree
Doctor of Philosophy in
Nuclear and Radiological Engineering

Georgia Institute of Technology

May 2017

IMAGING OF SPECIAL NUCLEAR MATERIALS USING MONOCHROMATIC GAMMA RAYS FROM LOW-ENERGY NUCLEAR REACTIONS

Approved by:

Dr. Anna S Erickson, Advisor, Chair
Nuclear & Radiological Engineering
Georgia Institute of Technology

Dr. Nolan Hertel
Nuclear & Radiological Engineering
Georgia Institute of Technology

Dr. C.K Chris Wang
Nuclear & Radiological Engineering
Georgia Institute of Technology

Dr. Michael Shannon
Advanced Concepts Laboratory
Georgia Tech Research Institute

Dr. Igor Jovanovic
Nuclear Engineering & Radiological Sciences
University of Michigan

Date Approved: January 6, 2017

ACKNOWLEDGEMENTS

Special thanks to Peter Binns of MIT Bates Linear Accelerator Center for help with operating the accelerator and going the extra mile to make sure things run smoothly. You are an invaluable asset at the facility and a good friend. Thanks to all the Bates crew who have participated and supported in my experimental efforts.

Thanks to the Achievement Rewards for College Scientists (ARCS) foundation for recognition and financial support. Also, thanks to the Roy G Post Foundation for recognition and financial support.

I gratefully acknowledge the support from the National Science Foundation under Grant No. ECCS-1348366 and by the U.S. Department of Homeland Security under Grant Award Number 2014-DN-077-ARI079-02. The views and conclusions contained in this document are those of the authors and should not be interpreted as necessarily representing the official policies, either expressed or implied, of the U.S. Department of Homeland Security.

TABLE OF CONTENTS

LIST OF TABLES

LIST OF FIGURES

SUMMARY

The pursuit of shielded special nuclear material in cargo can be facilitated by active interrogation employing discrete energy photons. A variety of detectors can be used for imaging cargo contingent upon the energies and fluence used in the interrogation. If the gamma ray energies are sufficiently well separated, as the case in ^{11}B(d,n-γ)^{12}C reaction resulting in photons of numerous energies up to 15.1 MeV, spectral analysis is possible with a variety of detector technologies. Identifying and characterizing a source like this one is crucial to produce a fieldable active interrogation system capable of imaging and identification of special nuclear material. Spectral analysis of the image can be used to confirm the presence of high-Z materials by analyzing the relative transmission of the two main energies emitted by exploiting the large difference in Compton scatter and pair production cross sections. Cherenkov detectors offer a low-cost solution but require a special approach to design and energy calibration due to the lack of resolution in order for spectral analysis to take place. High-density scintillators or semiconductor detectors can yield much better spectral information, but are considerably more expensive. Intermixing detector technologies in a compact array, such as silicon photomultipliers, can lead to data fusion techniques when coupled with the proper electronics. This thesis addresses the source characterization as well as imaging with a variety of detectors for active interrogation with monoenergetic photons and compares the imaging and material identification performance.

CHAPTER 1

INTRODUCTION AND BACKGROUND

A nuclear attack carried out on American soil has been one of the largest national security concerns since the mere idea of the atomic bomb. The concern is growing not only domestically, but also globally with the ever expanding presence, ambition, and sophistication of terrorist organizations. The ability to effectively detect and intercept illicit special nuclear material (SNM) is one of the grand technical challenges facing nuclear security today. Approximately 11 million cargo containers per year enter the United States through sea ports along with another 11 million by truck and 2.7 million by rail according to U.S. Customs and Border Patrol [1]. These seaports are hubs of economic activity, generally placing them in large cities as in Figure 1.1.

Figure 1.1: Manila International Container Terminal

Once the containers are off loaded from the ship, they are put on trucks or trains and transported to every corner of the country. Physically, opening and inspecting each con-

tainer is simply not an option. Inspecting the container without opening it generally involves measurement of radiation in heavily shielded, challenging environments. Further compounding the difficulty is the need for space and scan speed, for example entry ports with a requirement for two-minute scan per 40-foot container [2, 3, 4]. Passive detection falls short when materials of interest are shielded, requiring an external source of radiation in order to probe the material, a method referred to as active interrogation [5].

Active interrogation techniques currently available vary wildly depending on sophistication and capability. These systems usually involve accelerators generating large amounts of radiation creating harsh environments for detectors, electronics, operators, the cargo itself, and potential stowaways. Addressing all of these problems simultaneously is an arduous task which results in incremental improvements in one component of the current state of the art systems. An entirely new system and approach is needed in the attempt to make significant progress.

1.1 Research Significance

Applying active interrogation techniques to search for SNM is not a new concept, but generally the source of radiation is high energy neutrons from a D-T source or bremsstrahlung x-ray beams. Imaging using broad energy bremsstrahlung beams has been successfully proven, including some coarse elemental discrimination, but large doses imparted to the cargo are yet to be addressed. The use of monoenergetic photons from low energy nuclear reactions is a fairly new concept in active interrogation and has never been demonstrated for use in cargo imaging systems. The ^{11}B(d,nγ)^{12}C reaction has been identified as capable of producing highly penetrating gamma rays that could be used in active interrogation, but most of the research has been applied to cross section as a function of deuteron energy [6].

The research performed here seeks to make some fundamental advancements that can later be applied to patch a potential vulnerability at ports of entry to the United States where SNM may be hidden inside a cargo container as it enters the country. The work in this

thesis will be combined with other research aimed to identify new detector technologies, accelerator based radiation sources of high energy gamma rays, and novel imaging and analysis methods for active interrogation applications. The overall project should culminate in a proof of concept active interrogation system that consistently detects 100 cm^3 of SNM while imparting less radiation dose to the cargo than current methods in a cost effective manor. The conceptual imaging system employed in this work is illustrated in Figure 1.2.

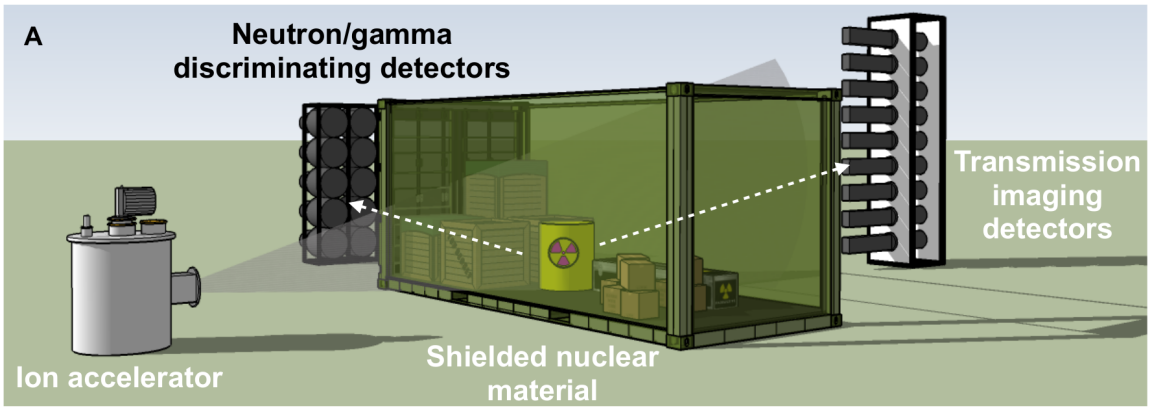

Figure 1.2: Conceptual depiction of proposed imaging system using a compact accelerator driven low energy nuclear reaction source and an array of detectors to measure photon transmission through the cargo and create images. The concept also includes a set of detectors capable of detecting neutrons and gamma rays to monitor for delayed radiation resulting from fission. Reproduced with permission from Rose et al. [7].

Low-energy nuclear reaction based sources are driven by ions accelerated to MeV-scale energy using a compact accelerator before they impinge on a target causing nuclear reactions that leave the product nuclei in highly excited states as well as stripping reactions. These excited nuclei quickly return to ground state emitting gamma rays of discrete energy, and sometimes neutrons, that are dependent on the incident particle and energy as well as the elemental composition of the target. Collimation results in a fan beam of highly penetrating radiation from the discrete energy photon source to interrogate the contents of the cargo container. This beam is used to perform transmission radiography producing high contrast, two-dimensional images as well as providing elemental discrimination in search of shielded SNM. The transmission imaging detector array must be comprised of sensors

capable of operating in high flux situations while still providing some level of spectroscopy. Design considerations for this array should focus on cost, speed, and resistance to neutrons, low energy background and scatter effects. Another set of neutron – gamma ray discriminating detectors will be designed to monitor for beta delayed radiation signatures from the cargo, thus confirming the presence of SNM.

This thesis presents a novel approach to address some of the challenges facing detection and imaging of shielded special nuclear materials in cargo. A multi-particle (high-energy monoenergetic photon and neutron) interrogation source based on a low energy nuclear reaction, the ^{11}B(d,nγ)^{12}C reaction [8, 7], is combined with a new class of radiation detectors and data acquisition methods designed for optimal operation in conjunction with this source. The detectors address several limitations encountered by standard alternatives, including the cost of coverage for imaging on the scale of standard shipping containers, robustness in high radiation environments, and particle identification in mixed radiation fields. This imaging method will be used to demonstrate desirable capabilities such as significant penetration through high areal density objects and physics based elemental discrimination mechanisms. While this work is not intended to demonstrate actual cargo scanning, it is intended to show a proof of concept of detector performance, imaging methodology, elemental identification, and source characterization of the major nuclear reactions taking place in the source that can later be scaled up for development into a fully deployable scanning system.

1.2 Objectives and Structure

The principle scientific purpose of this thesis is to investigate, evaluate, and validate three major components of the final system; detectors for an imaging array, an accelerator driven low energy nuclear reaction radiation source for discrete energy gamma rays, and imaging and analysis methods to quickly provide coarse material identification to detect potential SNM. Two key design considerations that are not part of this thesis are the dose calcu-

lation analysis and neutron detection systems for beta delayed radiation which are being addressed [9, 10, 11].

The proposed work expands on the analysis and characterization of the ^{11}B(d,n-γ)^{12}C source by attempting to gather the gamma spectrum with sufficient energy resolution and relate it back to the quantum states of the product nuclei as well as secondary nuclear reactions. Precisely identifying the gamma ray energies resulting from the source will lead to spectroscopic analysis of the photons transmitted through the cargo to unfold the Z_{eff} of the traversed material to identify illicit special nuclear material. Multiple detector technologies will be investigated to determine the feasibility and field-ability in an imaging array exposed to potentially harsh radiation environments. A custom array will be constructed fusing the most promising technologies with advanced data acquisition methods.

The structure of this thesis will address each of these challenges in-depth in separate chapters, each one meant as a self contained document yet building on the previous. Advancements resulting from this work can be applied to more that just cargo imaging applications, extending to many applications that require high energy photons or detection systems in harsh environments. The structure of each chapter will follow a sound scientific approach: motivation, formulation, implementation, validation with experimental results, and future work.

CHAPTER 2

DETECTION SYSTEMS IN ACTIVE INTERROGATION

Active interrogation applications routinely expose radiation detectors to challenging operating conditions. One of the largest vulnerabilities of detectors is damage due to harsh radiation environments, often consisting of mixed radiation fields, caused by the interrogating beams [12]. Commercially available detectors are usually made to operate in laboratory settings where the environment is stable against temperature fluctuations and radiation intensity is significantly lower.

High radiation flux applications, such as active interrogation systems, pose intricate detector challenges. In order to have a viable imaging system, the detectors must be scalable, customizable, economical, resistant to undesired radiation, and capable of processing high interaction rates. A deployable system should not be significantly affected by temperature fluctuations or other potential outdoor effects to maximize consistency.

This chapter focuses on select gamma ray and gamma – neutron discriminating detectors and their viability in the proposed active interrogation system as well as the associated readout electronics. A wide variety of detectors have been employed in these studies ranging from ultra-high energy resolution, high purity germanium (HPGe), to custom designed Cherenkov detectors with crude spectroscopic abilities. Both organic and inorganic scintillators are also included as potential candidates for use in the final system.

The spatial resolution of the transmission imaging system is fixed by the size of the detectors and the location of the imaged object relative to the source and detector array. The objects to be interrogated should be held at a constant distance from both so the real consideration here is the surface area of the detector perpendicular to the incident radiation. High spatial resolution requires a large amount of small detectors packed closely together which imposes additional concerns such as radiation cross talk, a process where incident

radiation in one detector interacts then causes signal in a neighboring detector.

This chapter will cover both commercially available detectors as well as some that are custom designs and manufactured in the laboratory. Not all of the detectors discussed are intended for use as the imaging system, but will be used in the accelerator driven environment for other purposes. A brief list of the commercially available detectors employed through out this work can be found in Table 2.1 including the manufacturer, part number, and geometry for reference.

Table 2.1: Selected commercially available detectors evaluated as part of this work with part numbers and geometry.

Material	Manufacturer	part number	length	width	height	diameter
NaI	Canberra	802-2X2			5.08 cm	5.08 cm
NaI	Saint-Gobain	2X4H16/2SS	40.64 cm	10.16 cm	5.08 cm	
LaBr	Canberra	1.5X1.5			3.81 cm	3.81 cm
EJ-309	Eljen	EJ309-3			7.62 cm	7.62 cm
EJ-299	Eljen	EJ-299-33	10.16 cm	2.54 cm	2.56 cm	
HPGe (80%)	Canberra	GC8021			7.62 cm	7.37 cm
HPGe (40%)	Canberra	GC4020			6.00 cm	5.79 cm

2.1 Electronics and Data Acquisition

Advances in signal processing technology have taken large scale detection down a new path. Traditionally, NIM bins or VME crates full of analog equipment would be used to acquire data and communicate to a single point of contact. These are large and bulky and often times introduce unnecessary noise to the signals. Each component of a readout system between the pulse generated inside the detector and the final conversion of that signal into quantified data adds more connections and complexity to the overall system. Simplicity and compactness are highly desirable in large scale systems because the more complex systems are more prone.

This research will use all digital data acquisition systems (DAQ) to maximize the spatial

density off the detectors while reducing the over all footprint and power requirements of such a system. Space is at a premium at ports of entry, so any footprint reduction is a positive point to a deployable system.

The digitizers considered here use on board field programmable gate arrays (FPGAs) to convert the detector signal from analog to digital and quickly process them on board. Most modern digitizers include memory buffers to store any events that may happen while the previous events are being processed. This technology virtually eliminates deadtime due to acquisition electronics yielding an over all improvement in the events per unit time possible in a system.

The most commonly used digitizer in this thesis is the CAEN x730 family of equipment. Both VME versions, consisting of 16 channels, and desktop versions, 8 channels, have been used for acquiring and saving raw waveforms, time-stamped list mode data, and processed multichannel analyzer (MCA) histograms. The x751 and x720 desktop digitizers from CAEN were also tested, a brief specification comparison of the desktop digitizers can be found in Table 2.2.

Table 2.2: Selected CAEN digitizers and relevant properties

Property	DT5720	DT5730	DT5751	DT5724
Sampling frequency (MS/s)	250	500	1000/2000	100
Input channels	4	8	4/2	4
Input impedance (Ω)	50	50	50	50
Input dynamic range (Vpp)	2	0.5/2	1	0.5/2.25/10
Bandwidth (MHz)	125	250	500	40

These digitizers allow for multi-board synchronization and system scalability through optical link protocols while the VME versions can leverage the built in back plans or the optical links. The physical footprint of these units measures just 15.4 x 5.0 x 16.4 cm and they can be easily stacked on top of each other. Digital pulse processing is performed on-board to reduce the amount of data transferred from the units to a central computer.

The pulse shape discrimination (PSD) firmware and software is the preferred processing method for this thesis because it it the most flexible in terms of detector types and desired data yet is also faster than other available firmware.

All of the detectors evaluated were connected directly to the digitizer from the anode output of the photomultiplier (PMT) eliminating the need for additional connections, even the preamplifier. This reduces the connections down to just the high voltage supply and a single wire per detector for the output signal simplifying the system. The x730 family of digitizers was chosen for subsequent studies due to the combination of sampling frequency, input sensitivity, bandwidth, and channel density.

The sampling frequency and input sensitivity are highly important for Cherenkov applications because the pulses are ultra fast with the length mainly depending on the electron transit time of the PMT. Cherenkov radiation is released in a near instantaneous burst of optical photons, increasing the number of samples of the waveform increases the energy resolution of the acquired pulse. The 2GS/s sampling frequency of the x751 series would be beneficial, however is significantly more expensive and contains less input channels. The x720 and x724 perform well for scintillator based detectors with moderate to long decay times but result in under-sampling of the Cherenkov pulses. The x730 series offers the best combination of channel density, sampling frequency, and lowest input sensitivity so no additional amplification of the Cherenkov pulses are necessary.

2.2 Scintillators

The detector investigation begins with scintillator based materials coupled with PMTs since they are the most widely used detectors due to their versatility. The physics of the scintillation process is well understood, characterized, and documented in many textbooks so this discussion will skip to the relevant considerations for active interrogation use. Of particular interest here is the performance in high flux situations with gamma rays ranging up to 15.1 MeV including decay times, temperature dependence, cost, scalability, energy resolution,

susceptibility to moisture, and intrinsic efficiency. These detectors are highly sensitive to natural background as well as low energy activation products which add enormous overhead demands to an active interrogation system. A summary of relevant properties of select scintillators explored as part of this work can be found in Table 2.3.

The physics behind scintillation light induces a dependency on decay times and light output per unit energy which can fluctuate heavily depending on temperature as shown in Figure 2.1. Temperature effects are very important as an active interrogation system typically needs to be able to operate consistently and reliably under exposure to various weather conditions. Operation strictly in a climate controlled environment at all times is not feasible; therefore, temperature effects must be minimized or eliminated.

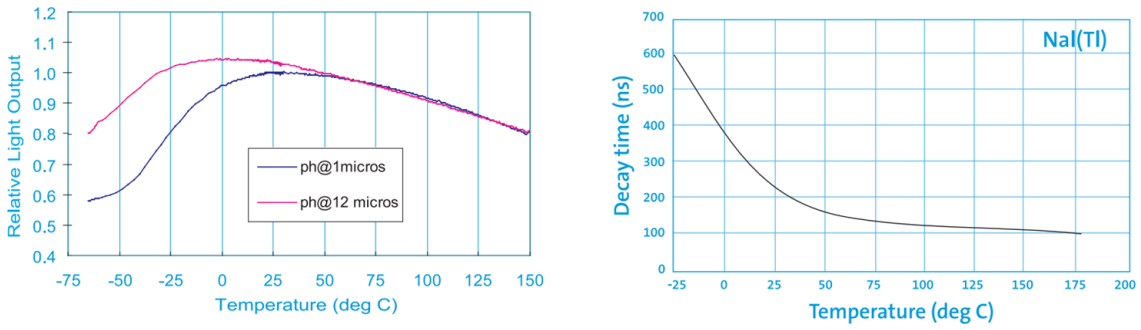

Figure 2.1: NaI decay and light output as a function of temperature. (Left) light output of NaI as a function of temerature; (Right) variation in scintillation decay constant, 1/e dependence, as a function of temperature taken from Saint Gobain product brochure [13].

Table 2.3: Selected scintillators and properties considered for use in active interrogation.

Property	LYSO	BGO	CsI	LaBr	NaI	EJ-309	$CdWO_4$	EJ-299-34	Stilbene
Density (g/cm^3)	7.15	7.13	4.51	5.10	3.67	0.96	7.90	1.08	1.15
Decay time (ns)	42	300	980	30	250	3.5	12,000	13, 35, 270	4.50
Intrinsic Radioactivty	Yes	No	No	Yes	No	No	No	No	No
Hygroscopic	No	No	No	Yes	Yes	N/A	No	No	Yes
Luminosity (photons/MeV)	24,000	8,000	55,000	75,000	45,000	12,300	7,800	8,600	8,700
Energy resolution (@ 661 keV)	7.1%	12%	5.7%	2.9%	7.0%	>20%	>20%	>20%	>20%
Reference	[14]	[15]	[16]	[17]	[18]	[19]	[20]	[21]	[22]

Figure 2.1 shows the light output (left) and decay time (right) as a function of temperature for typical NaI crystals. Temperatures around freezing, $0\,^{\circ}$C, are common in most geographical regions of the U.S. depending on the time of year which poses a large problem for NaI detectors as the decay time nearly doubles with respect to room temperature, and the light output per incident energy significantly decreases. As the temperature changes throughout the day, this detector will have to be constantly re-calibrated, and the analysis of the signal must change as well. The increased decay time will lead to more pulse pileup and dead time that must be accounted for.

2.2.1 Inorganic

The most popular scintillator used today for general purposes is NaI(Tl). This material is fairly inexpensive and comes in many form factors such as the 5.08 cm long, 5.08 cm diameter cylinder and 5.08 x 10.16 x 40.64 cm ingot like crystals. Both of these form factors were used in studies relating to active interrogation. The larger crystals were designed and built specifically for other nuclear security applications that require large coverage detectors. The size of these crystals presents a limit of the spatial resolution available as the smallest face is 5.08 x 10.16 cm which dictates the smallest pixel size possible in an imaging application. This detector is highly efficient with high energy gamma rays due to the 40.06 cm length of the crystal; however, a crystal this large can cause deterioration of energy resolution due to optical photon re-absorption. NaI also has a characteristic decay time of 250 ns, which can easily lead to pulse pile up in high flux situations resulting in event rejection or mis-classification.

One material showing promise over NaI is $LaBr_3$(Ce) for the increased density and superior energy resolution combined with a much shorter decay time. The material evaluated here, BrilLanCe 380 manufactured by Saint Gobain, was purchased as a detector assembled by Canberra, LABR 1.5X1.5. The geometry of this crystal, 3.81 cm diameter and 3.81 cm in length, results finer pixel density than the NaI detectors. One drawback of this

detector for imaging is the relatively short length of the crystals which will result in lower efficiency. Larger crystals can be made; however, the material is intrinsically radioactive which poses a limit on the size of the crystals based on the radioactivity per gram. Smaller diameter crystals that are longer could be a good trade off; however, this material is still fairly new, and custom geometries are expensive.

The NaI and LaBr materials are both hygroscopic: they absorb moisture from the air, so they must be assembled in inert environments and kept sealed which is not conducive to custom detector development. Nonhygroscopic materials such as LYSO, BGO, and CsI can be ordered from various manufactures in custom sizes and assembled in the laboratory. Ingots of each measuring 6 x 6 x 50 mm were acquired and evaluated side by side in the quest for building an array with high pixel density using the 6 x 6 mm faces. CsI is attractive due to the moderately high density and energy resolution, yet prove to be unusable in this type of system due to the extremely long decay times. The intrinsic efficiency of BGO and LYSO will be higher than all the other crystals tested because of the high density, over double that of NaI. LYSO exhibits a much shorter decay time than BGO meaning it is capable of processing more photons in the same amount of time which leads to a reduction in pulse pile up. The increased luminosity of LYSO results in improved energy resolution over the BGO as well.

Some imaging systems use $CdWO_4$ detectors which prove to be highly efficient due to the high density, about 7.9 g/cm^3, of the crystals [23]. While they are great for raw counting of gamma- or x- rays in Geiger mode, they lack good spectroscopic capabilities. The scintillation decay time is comprised of two parts consisting of 5,000 and 20,000 ns decay constants [24] which is too long for the proposed high flux active interrogation system.

2.2.2 Organic

Organic scintillators, such as EJ-309 made by Eljen Technologies, usually exhibit much faster decay times than their inorganic counterparts. EJ-309 is a liquid scintillator that can

be made into containers of various geometries customized to the application. The detectors used as part of this work were 7.62 cm diameter cells, 7.62 cm in length. Another Eljen product, EJ-299-33, was also investigated because it is a solid plastic scintillator 2.54 cm square face and 7.12 cm in length. The solid nature of this product is favorable to form an array because it can easily be made into uniform ingots and does not require a glass enclosure. EJ-299 is physically robust, reliable, inexpensive, and easily fabricated into desired shapes. The last inorganic scintillator applied to this work is a monolithic Stilbene crystal from Inrad Optics. This crystal measures 1.2 cm square on the face and 8.0 cm in length and is wrapped in PTFe reflector tape. One added benefit of these detectors is that they can all be used to detect neutrons through pulse shape discrimination techniques.

The biggest drawback of organic sctinillators is the extremely low density compared to the inorganic crystals resulting in poor efficiency for detecting gamma rays and the lack of energy resolution. Many also suffer from radiation damage, aging, and they are not resistant to elevated temperatures. Another consideration is the additional gamma rays introduced in to the detection system from neutron capture in hydrogen resulting in a 2.2-MeV gamma ray.

2.3 Custom Cherenkov Detectors

Cherenkov detectors are well suited for the challenges involved in active interrogation, especially when high energy resolution is not a priority. It has been shown that Cherenkov detectors can provide crude spectroscopy when properly designed and implemented [25]. This type of detector can be considerably less costly than its scintillator counterparts [26]. Cherenkov radiation is an instantaneous burst of electromagnetic radiation, released in the form of optical photons, resulting from charged particle motion in a dielectric medium where the velocity of the charged particle, v, is greater than the phase velocity of light in that medium [27, 28]. This is an important physics process because it means there is an inherent energy threshold for emission based on the refractive index, n, of the material and

the charged particle type and velocity [29] as described in Equation 2.1.

$$v > \frac{c}{n} \tag{2.1}$$

One popular material used for Cherenkov detector applications is leaded glass. This material has a high density relative to other glass due to the lead dopant. Leaded glass comes in many varieties and is frequently used as radiation shielding windows in keV–range x-ray applications. The material considered here is SF57 manufactured by Schott with a density of 3.53 g/cm^3 and a refractive index of n = 1.84. Cross sections for this particular material have been compiled from NIST XCOM and can be found in Figure 2.2.

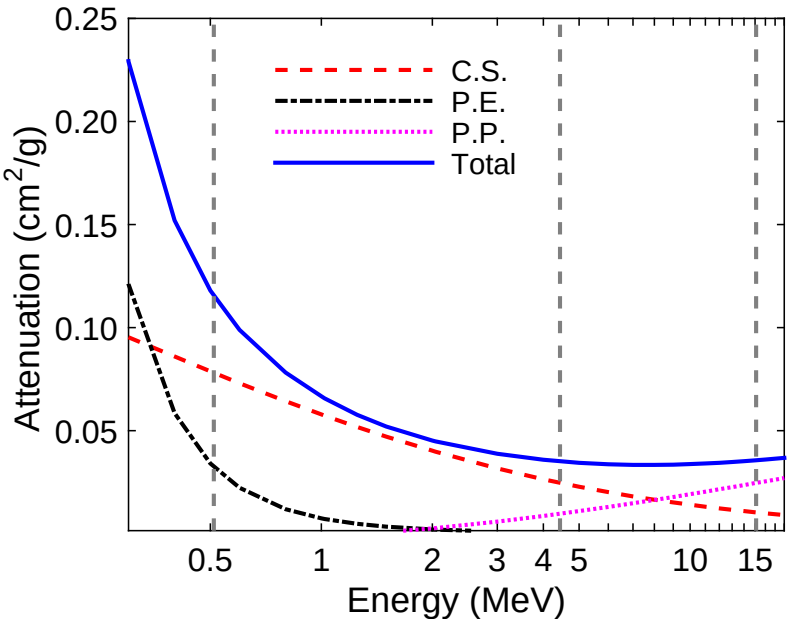

Figure 2.2: Schott SF57 leaded glass attenuation coefficients as a function of energy. Data downloaded from NIST XCOM [30] and replotted.

An alternative to leaded glass is high purity quartz, SiO_2. This material is optically clear and exhibits great optical light transmittance making it popular for applications such as microscope slides and optical lenses. The density of this material is lower at 2.2 g/cm^3 for GE-214 from Momentive, and has a refractive index of n = 1.45. The cross sections for this material have also been compiled neglecting impurities below 0.001 ppm by weight

and can be found in Figure 2.3.

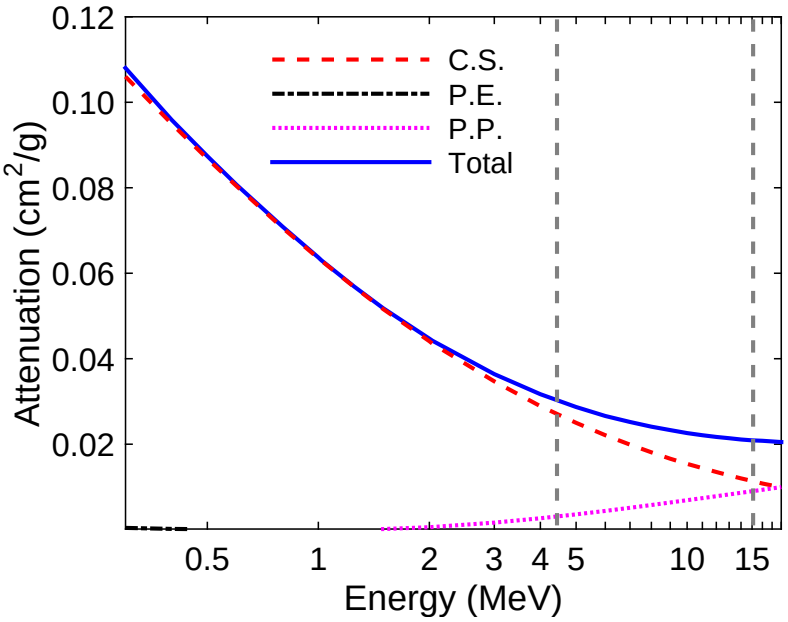

Figure 2.3: High-purity quartz (SiO_2) glass attenuation coefficients as a function of energy. Data originally downloaded from NIST XCOM [30].

Energy resolution is not easily quantifiable when using Cherenkov detectors as there are no photopeaks to determine resolution in the usual way due to the continuous nature of the optical photon emission. While the energy resolution, or spectral features such as Compton edges and shoulders, of small volumes of leaded glass is slightly better due to the increased density, the UV–blue light absorption is significantly higher which hinders larger crystals. The internal light transmittance of this material is high in the red and IR range, but is only 0.3% at 365 nm which is the UV cutoff as shown in Figure 2.4. This poses a significant problem as the Cherenkov emission spectrum is generally concentrated in the UV region. The intrinsic efficiency and resolution gains of this material are negated by the reduced optical transmission efficiency.

Quartz, GE-124, has superior light transmittance over the SF57 leaded glass in the UV – deep blue region, 160 – 360 nm. Cherenkov light collection is challenging yet important in this region. Optimizing the collection of optical photons is crucial to consistently separate

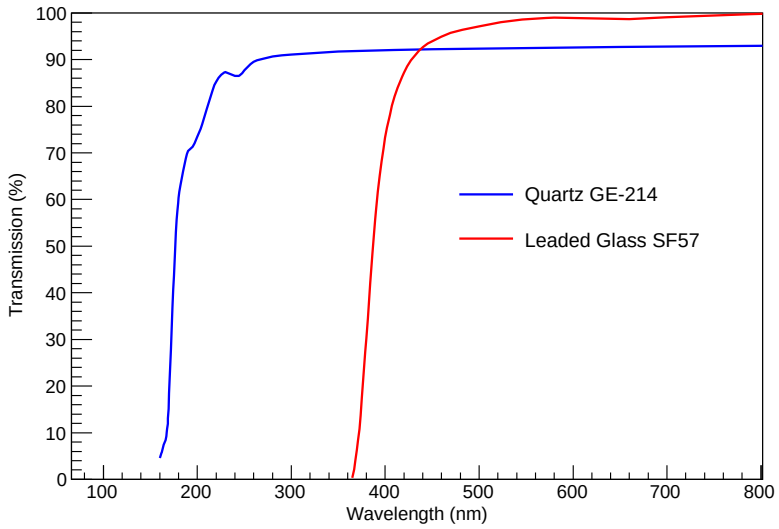

Figure 2.4: Comparison of light transmission from two potential Cherenkov radiating materials, GE-214 quartz (blue) and SF57 leaded glass (red). Plot produced from transmission date published by the manufactures, Momentive [31] and Schott [32] respectively.

Cherenkov events from PMT noise and the integrity of spectroscopic information.

One of the largest drawbacks of leaded glass in this case is the larger photoelectric cross-section as compared to quartz. The presence of lead in the glass introduces a significant increase in photoelectric cross-section causing increased signal in the lower energy range. The light produced from the photoelectric interactions in Cherenkov counters is useful if operating in Geiger mode (looking for total counts), but hinders the spectral features if spectroscopy is the goal.

One of the main focuses in this research is to reduce the data collection overheads to the electronics allowing the use of higher interrogating beam current in order to reduce the scan times needed. In addition to higher photoelectric cross section, leaded glass also has a much higher refractive index which results in a lower kinetic energy threshold to generate Cherenkov radiation. The quartz selected has a kinetic energy threshold for electrons of 336 keV while the threshold of SF57 glass is 214 keV as shown in Figure 2.5.

The higher energy threshold of quartz is preferable to avoid contribution from low energy background, including environmental products induced by the accelerator. The thresh-

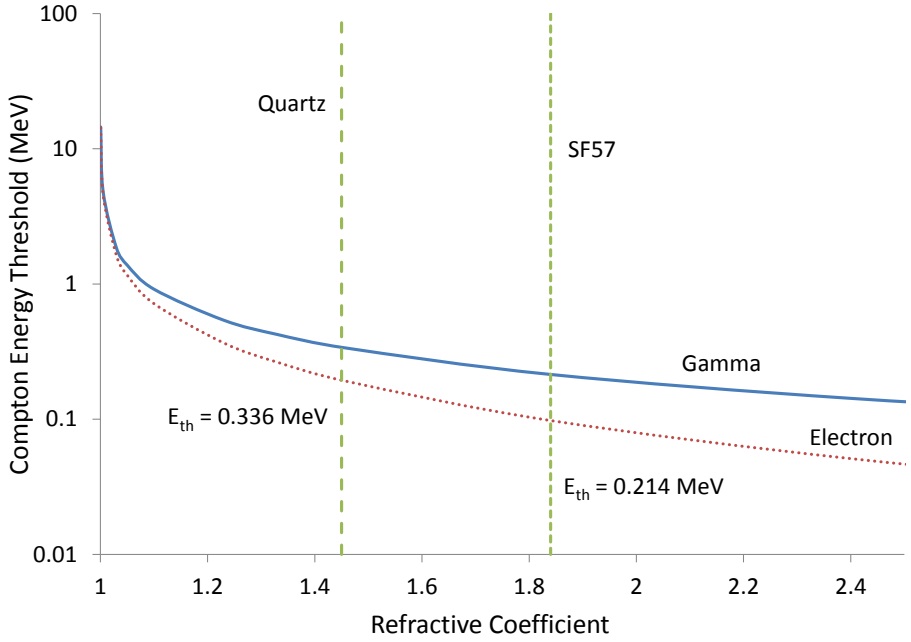

Figure 2.5: Compton electron energy threshold for Cherenkov light production as a function of refractive index and corresponding minimum gamma ray energy.

old of leaded glass also presents a problem for pair production events. The maximum energy transferred to a Compton electron from a 511 keV annihilation photon is 314 keV. This is below the kinetic energy threshold of quartz, but can radiate Cherenkov light in the leaded glass. Signal resulting from this in the leaded glass is indistinguishable from the photoelectric signal reducing the ability to use spectral features. Photons of 511 keV are frequently emitted from activation products and other reactions that will only compound the problem. These photons are also one of the main sources of detector crosstalk when using high energy gamma ray beams.

Multiple Cherenkov detector designs have been implemented as part of this thesis falling in to two main categories based on the photo sensor, PMTs and silicon photomultiplers (SiPMs). Evaluation of multiple Cherenkov radiating materials resulted [26] in the selection of a high purity SiO_2 quartz material, GE-214, for use in this system. Quartz is a rugged material, resistant to radiation damage, and virtually immune to temperature ef-

fects over the expected range of an active interrogation system. These detectors will not be affected by low energy background, activation, or the 511–keV photons from positron annihilation significantly reducing the detection system overhead and increasing the possible number of high energy gamma ray events recorded per unit time.

Three Cherenkov detector designs based on PMTs were constructed and applied for these studies: (1) 5.08-cm long quartz crystal coupled to a Hamamatsu R292 PMT with a quartz window and lower sensitivity limit of 190 nm; (2) 10.16-cm long quartz crystal coupled to a Hamamatsu R6095-03 PMT with a sensitivity limit of 300 nm; and (3) six 15.24-cm long quartz crystals coupled to Hamamatsu R374 PMTs with UV transmitting glass windows and a sensitivity limit of 185 nm. The windows of the R292 and R374 PMTs have a refractive index very similar to that of quartz, reducing the light loss on the boundary. Cherenkov radiation is more intense in the blue/UV region causing the R6095-03 PMT to cut off the signal below approximately 300 nm, reducing the detector light output compared to other designs. However, this design exhibits the shortest electron transit time of the three yielding narrower pulse widths which leads to less possibility of pileup and the potential to process more events per unit time. All Cherenkov detector crystals are cylindrical in shape, with a 25 mm diameter. Figure 2.6 shows the spectroscopic capabilities and energy calibration relationship from a ^{60}Co, PuBe, and ^{nat}B(d,nγ)^{12}C reaction using these detectors.

The SiPM based Cherenkov detector design uses the same GE-214 material but measures just 6 mm in diameter and 50 mm in length. This diameter was chosen to match the dimensions of the SensL J-series SiPM sensitive area, 6 x 6 mm. This design can be tightly tiled together for a high pixel density to increase spatial resolution. These crystals use the same PTFe tape reflector as the PMT based detectors. Initial designs used traditional optical grease for coupling but they suffered from light transmission degradation over time due to evaporation in the optical grease. This prompted evaluation of more optical coupling agents resulting in rebuilding of all the Cherenkov detectors to use Rexon 22P semi-curing

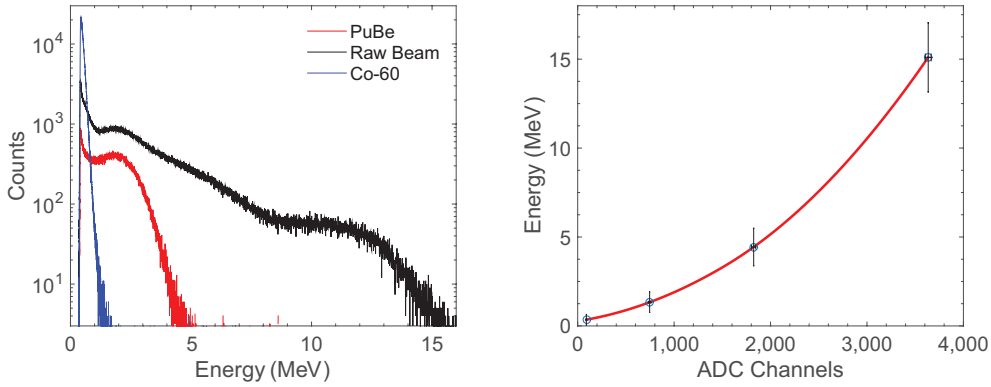

Figure 2.6: Spectra obtained (left) with quartz Cherenkov detectors used to produce an energy calibration relationship (right). Adopted from [26] where crude spectroscopy with these detectors was employed.

optical coupling agent.

2.4 Semiconductors

High purity germanium (HPGe) detectors are typically not used in high flux active interrogation applications because of the inherent rate limitations based on the physics of the detector. However, they are instrumental in this thesis in order to characterize custom detectors and the low energy nuclear reaction source so they are included here. Pulses from the semiconductor crystal are small and require preamplifiers to stabilize the signal, boost the pulse height, and impedance match to the processing electronics. Preamplifiers produce pulses with a long decay time leading to more pulse pileup and dead time than most other detectors. However, the unparalleled energy resolution of this detector technology renders it indispensable when it comes to characterizing an unknown source, such as the exact energy spectrum from the ^{11}B(d,nγ)^{12}C reaction. Care must be taken to reduce the neutron flux incident on the detectors as they are susceptible to neutron radiation damage.

Two HPGe detectors were used as part of this work, both standard electrode coaxial designs, manufactured by Canberra Industries. Both mobile designs are liquid nitrogen cooled via the flanged multi-altitude cryostat (Big-MAC) with external preamplifiers. There are

two main differences in the detectors, the size of the crystal and the preamplifier coupled to the system.

The first system investigated is a model GC4020, dubbed the 40% HPGe, using a standard 2002C RC preamplifier. The detector specification performance data provided by the manufacture for this unit specify an energy resolution of 2.0 keV FWHM at 1.33 MeV and a crystal size of 59.7 mm diameter and 60.0 mm in length. This detector is an "off-the-shelf" design from Canberra and is versatile enough for most applications. Detector control and data acquisition was performed with a CAEN DT5781 digital MCA and uses their MC^2 software package. The DT5781 is equipped with a FPGA featuring the real-time Digital Pulse Processing for Pulse Height Analysis (DPP-PHA firmware) making the module a spectroscopy acquisition system. This stand alone unit provides energy and timing information as well as waveforms and internal signals for quickly optimizing pulse processing parameters in real time for best results.

The second detector employed is a model GC8021, referred to as the 80% HPGe, using a specialized 2101P-10 preamplifier. The detector specification performance data provided by the manufacture for this unit specifies an energy resolution of 2.1 keV FWHM at 1.33 MeV and a crystal size of 73.7 mm diameter and 76.2 mm in length. This detector was custom designed with Canberra to operate in the presence of gamma rays slightly exceeding the 15.1-MeV gamma ray proposed in this project. This was accomplished in part by the larger crystal design to improve the intrinsic efficiency of the detector as well as the modified 2101P-10 preamp. This is a transistor reset preamplifier (TRP) with some electrical modifications by Canberra to operate in high flux situations in the energy range desired. This specialized preamp dictated the use of a Lynx digitial signal analyzer and Genie2k version 3.4 from Canberra for optimal performance. At the time of the experiments in this thesis, there was no alternative available from CAEN to properly handle the TRP.

The use of a TRP in the system requires an extra connection from the detector to the electronics that inhibits the data acquisition process while the preamplifier resets itself

through a self imposed discharge. The induced charge from radiation events in the detector are not discharged by the preamp until the full range of the voltage circuit is exceeded (typically 4V). At the maximum range the preamp is rapidly reset to collect charge again. Consequently the direct output of the preamp does not exhibit a series of triangular shaped pulses of a few millivolts in magnitude (as is typical for RC type preamps), but rather a saw tooth pattern of about 4 volts in magnitude and (when exposed to constant radiation) a generally regular frequency roughly proportional to the event rate as depicted in Figure 2.7.

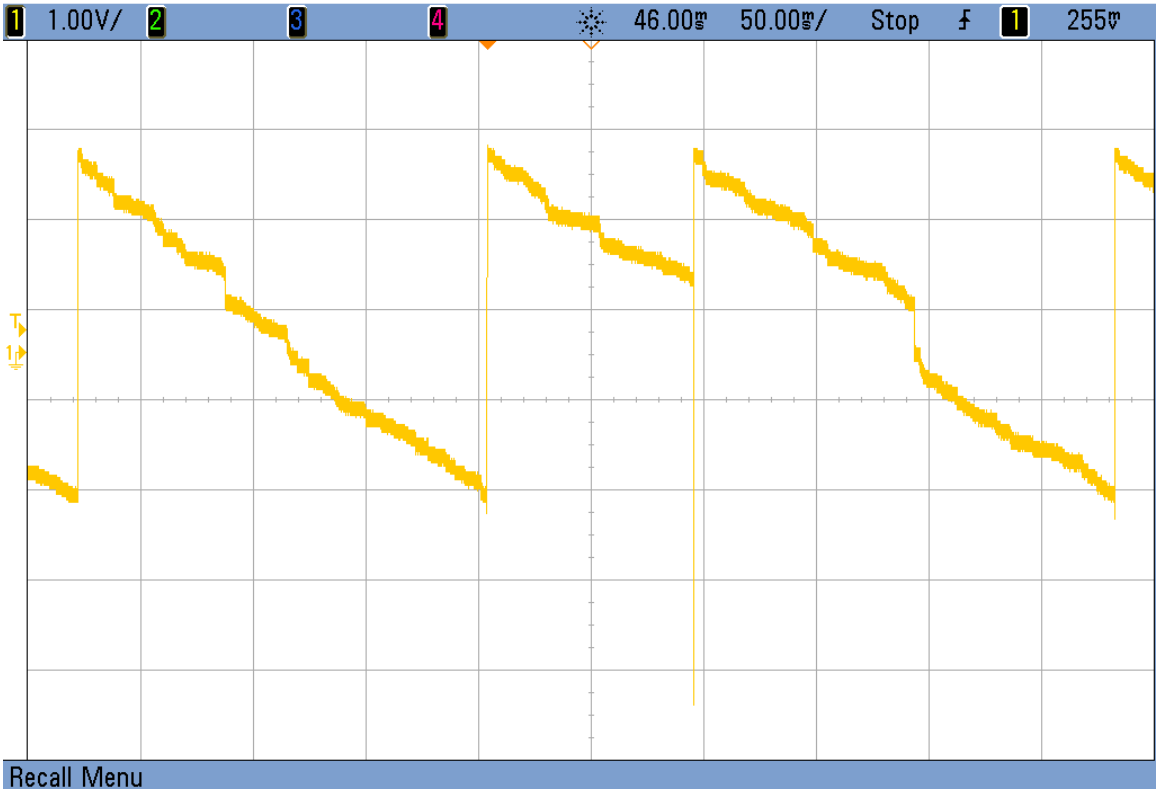

Figure 2.7: Macroscopic view of the sawtooth-like transistor reset preamplifier (TRP) operation including a single large event (cosmic) inducing a reset.

If one zooms in on the sloping part, one will observe steps that are not smooth, but rather a series of small steps (in this case, negative steps) that are in fact the result of individual events within the detector. In CANBERRA MCA's, there is a setting to define whether the input preamp is an RC type or a TRP type. This ensures that the signal is handled properly at the first input stage. After this stage the rest of the signal processing is identical, with the

exception that an anti-coincidence gate is applied during the TRP reset so that this dramatic event is not processed as a real pulse. This technique slightly increases the deadtime of the system in low count rate situations, however it prevents the detector from paralyzing in high count rate situations.

The resetting of the preamplifier is not strictly a function of count rate, but is actually dictated by the rate of energy deposition. The pulse height of a high energy gamma ray is considerably larger than that of a low energy gamma ray so the high energy gamma ray is more likely to be involved in the forced resetting event. The last event causing the forced resetting is discarded since the full height of the pulse cannot be determined. This results in a skewed collection of high energy events relative to low energy events which is problematic for correcting the resulting spectrum for efficiency, deadtime, and lost events in the attempt to quantify the source production of one energy versus another. However, this piece of equipment was specifically designed to operate in the high flux, high energy environment needed to characterize experimental active interrogation beams introduced in the next chapter.

2.5 Detector Performance and Evaluation

2.5.1 High Purity Germanium

Comparing the performance of the two HPGe detectors used can be broken down in two categories; general use and beam-line operation. General use consists of a variety of sources commonly available in laboratory settings. Both of the detectors will perform essentially the same under these conditions and does not present anything interesting as related to this research so it will not be discussed.

The relevant comparison of these two detectors is made when exposed to gamma rays ranging from 0.511 to 15.1 MeV as in the proposed active interrogation system. Application of the detectors in the complex, high flux environment is challenging. Great lengths were taken to ensure the detector crystals were equally collimated and shielded from room

return so the comparison focuses on the principle of operation, mainly the TRP versus RC preamplifier. Details of the accelerator driven ^{11}B(d,nγ)^{12}C reaction source will be presented in the next chapter, however the results of the initial tests of both detectors can be found in Figure 2.8 for a comparison here.

The detectors varied wildly in terms of dead time and total count in the beam line, however the main interest of these studies is to determine the exact energies of the peaks between the well understood 4.4 and 15.1-MeV gamma rays. The top spectrum is a product of the 40% detector with the standard RC preamplifier. The 4.4-MeV gamma ray response can be seen with the full energy deposition peak being around channel 600 on this scale yet no higher energy peaks are resolved due to pulse pile up and dead time. The bottom spectrum is a result of the 80% detector in the beam using the TRP instead of the RC preamplifier. This crystal is essentially double the size so one would expect the pile up and lack off energy resolution to be compounded. However, the operation of the TRP spectrum clearly shows a multitude of peak between the 4.4 and 15.1-MeV range.

These two spectra were obtained using the same accelerator current, 2.5 μA, but the resulting dead times were 98.7% and 2.7% for the 40% and 80% detectors respectively. The 40% spectrum was not energy calibrated here due to the lack of resolved high energy peaks. The 15.1 MeV response should be somewhere around channel 2000 but it is not resolved enough for a proper energy calibration. The clear choice of detector for the beam characterization work is the larger, more efficient crystal as it suffered less dead time and produced a well resolved spectrum of the source over the entire 0 – 15.1 MeV range.

2.5.2 Detectors for Imaging Array

The comparison of detector technologies for use in an active interrogation here will focus on a few key considerations: pixel density, environmental stability, and theoretical number of pulses per unit time which dictates the scanning time required. This is not an exhaustive list of all factors that could be investigated for active interrogation as that depends on the

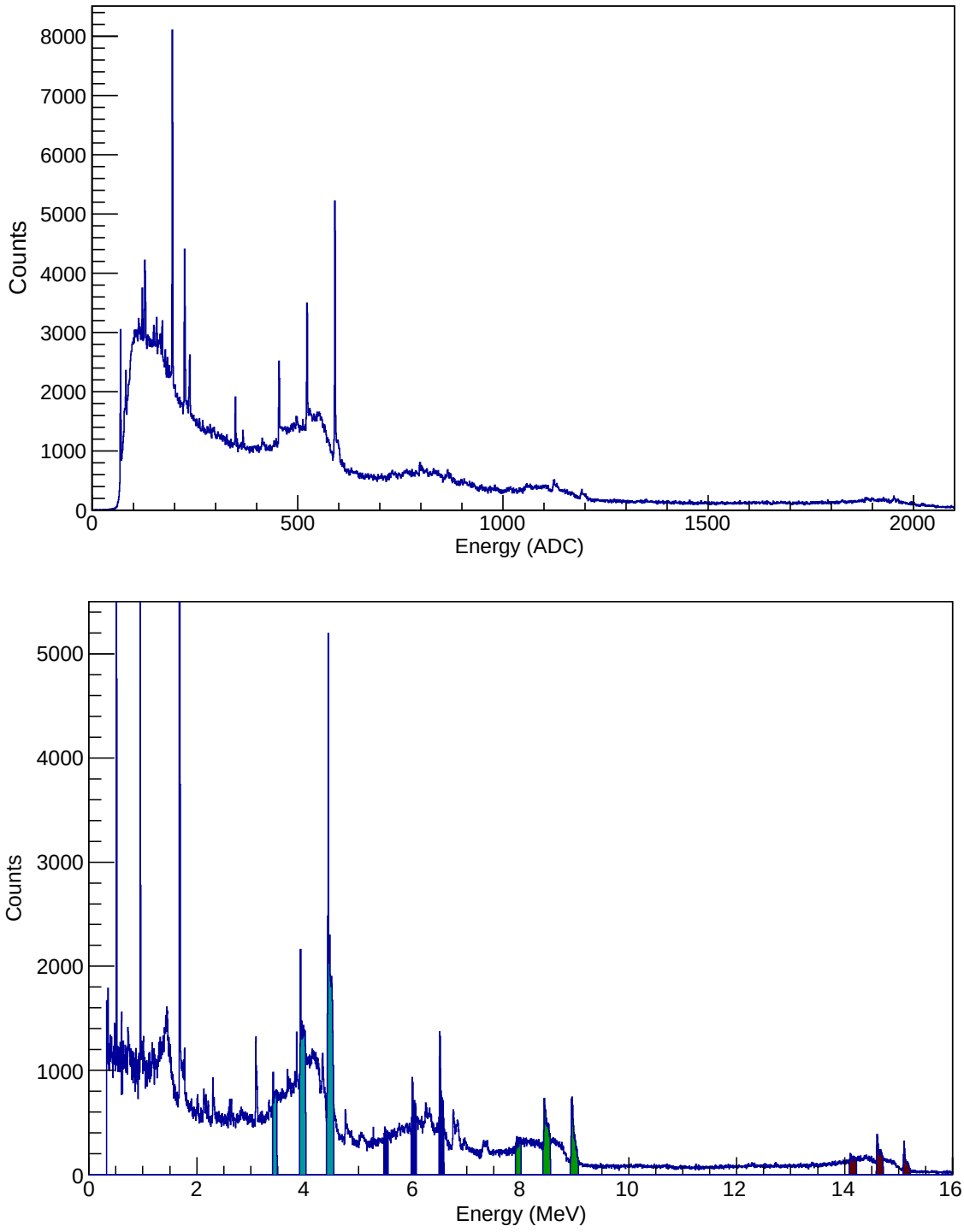

Figure 2.8: Spectra of the accelerator driven ^{nat}B(d,nγ)^{12}C reaction obtained with (top) GC4020 HPGe using RC preamplifier and (bottom) GC8021 HPGe using TRP.

goal of the application.

Pixel density, or number of detectors per square unit area, is the determining factor of the image spatial resolution. The pixel density can be tailored to a specific application to balance other parameters impacting the image quality such as the distance between the source, interrogated object, and detector array as well as the source size. This is typically a parameter specified as part of the goal of the project. No such parameter was dictated for this work, but the goal here is to create an array with a balance of spatial resolution and cost.

One major consideration for pixel density is the effects of an incident gamma ray interacting in one detector and causing an event in a neighboring detector by either Compton scattering or pair production resulting in 511–keV gamma rays from positron annihilation. This is a process known as radiation cross-talk and is influenced by many factors such as geometry and density of the detector volume as well as spacing of the detectors. Decreasing the distance between two detectors increases the probability for cross talk which artificially inflates the number of counts in the surrounding detectors when trying to measure transmission of discrete energy photons through some material. This leads to increased potential for pulse pile up and degrades energy resolution in the detector. Often times the energy of the Compton scattered photon is below 1 MeV depending on incident energy and scattering angle. Threshold detectors, such as the Cherenkov designs discussed in previous sections, can lead to significantly reduced cross talk in the presence of high energy gamma rays because they are not sensitive to the 511–keV gamma ray from pair production events in neighboring detectors. Additionally, a Compton scattered photon must deposit enough energy in the secondary detector to exceed the threshold.

Cross talk effects have been modeled in Geant4 using the large 5.08 x 10.16 x 40.64–cm NaI detectors and the 25–mm Cherenkov detectors. The simulated source is a simplified version of the low energy nuclear reaction based source presented in the next chapter. This is used in attempts to more accurately portray the effects of cross talk in the proposed active

interrogation system. The discrete energy beam is set as a surface source matching the size and geometry of the different detectors and is set to be incident on a single, central detector in an array. The analysis tracks events in the target detector and subsequent events in the neighboring detectors as they are moved farther apart resulting in a decreasing crosstalk versus increasing separation as seen in Figure 2.9.

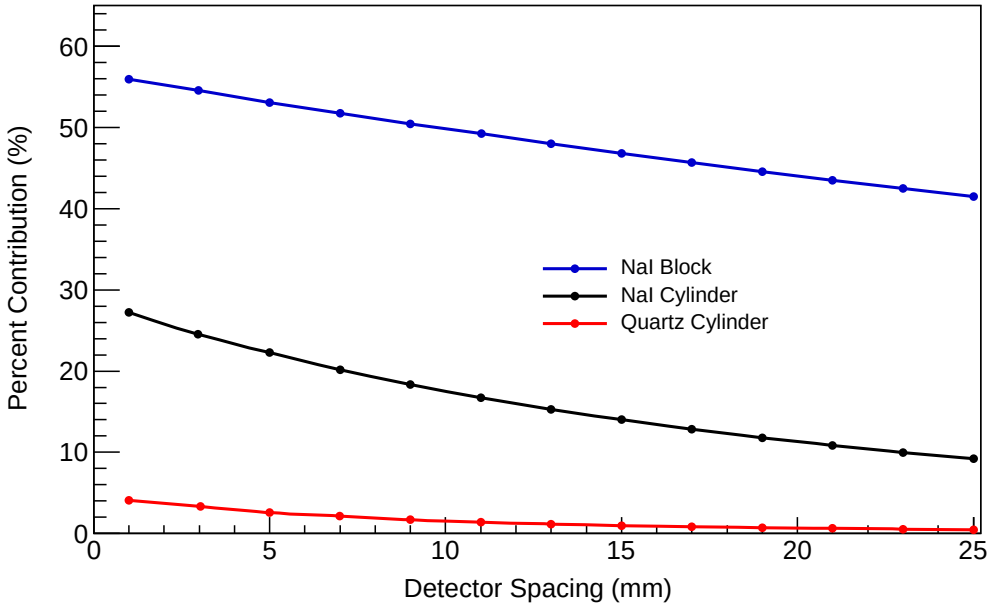

Figure 2.9: Simulated results of crosstalk contribution as a function of separation distance between detectors.

The percent contribution presented here is crosstalk events in the neighboring detector divided by the crosstalk events plus primary events in the target detector to represent the expected contribution of the detector in a beam situation. Comparing the actual detectors to each other is an inaccurate comparison due to the size difference. To resolve this, the quartz detector geometry was combined with the NaI material properties to produce the results denoted as “NaI Cylinder”. The Cherenkov detectors outperform the identical geometry NaI detectors by nearly an order of magnitude through most of the distances from 1 to 25 mm separation. This is largely due to the Cherenkov threshold properties and the lack

of photoelectric interaction of low energy gamma rays in the quartz material. Recall that an electron must have at least 336 keV to generate Cherenkov radiation in both detectors, target and secondary, and the 511–keV photons resulting from pair production will not cause Cherenkov radiation. The NaI detectors are sensitive to the photoelectric interactions, do not have a low energy threshold, and contain higher Z material which results in more pair production causing annihilation photons which then go on to interact in neighboring detectors. Detector cross talk results in prohibitively more events detected that add to detector overheads but do not contain useful transmission information for imaging. This can be partially mitigated in any type of detector by coincidence rejection; however, this imparts massive overheads and complexity to the data acquisition system and is not realistic for large arrays of tightly tiled detectors.

Organic scintillators are generally used for fast neutron detection through proton recoil events inside the detector. The low density of these materials, on the order of 1 g/cm^3, is far too low to efficiently detect gamma rays. Most high energy gamma rays will not interact in the low density material which results in significantly longer scanning times. This is contrary to the goal of the proposed imaging array in this research so they will not be considered as viable options as gamma ray detectors for the rest of this thesis.

Another disqualifying factor among the investigated scintillators is the characteristic decay time, given as $1/e$. Large events, such as a response to 15.1–MeV gamma rays will take more than a factor of 10 over the tabulated decay time to return to baseline. Long decay times dictate increased pulse integration times which limits the number of possible events per second a system can handle, again increasing scan times. Scintillators like CsI and $CdWO_4$ may have sufficient density to make then viable from an efficiency standpoint, however the increased pulse pile up and dead time from the longer decay constants render them unfavorable. To illustrate the effect of the decay time, consider the performance between two scintillators of essentially equal density but different characteristic decay times like LYSO and BGO seen in Figure 2.10.

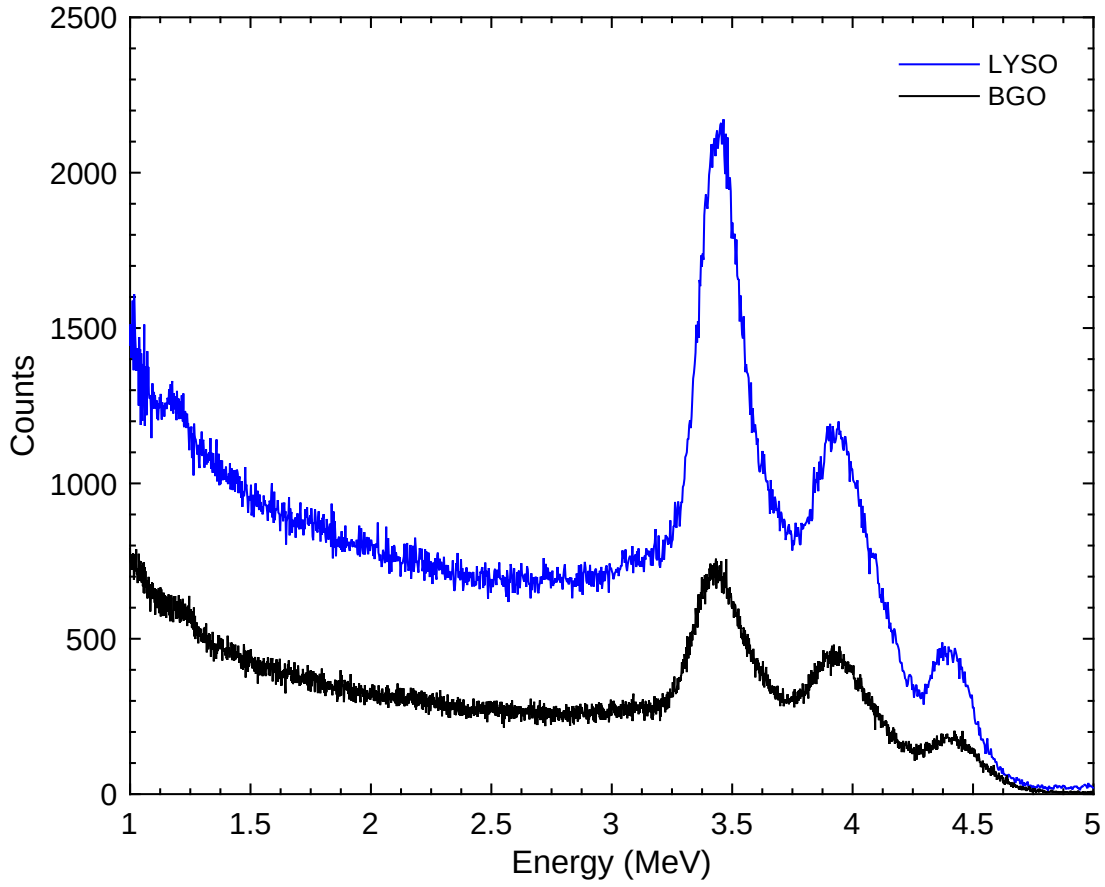

Figure 2.10: Comparison of PuBe spectra obtained from LYSO and BGO crystals on SensL J-Series SiPMs. Both experiments were conducted for the same amount of time, but the LYSO system was able to process moe events due to the shorter scintillation decay time.

This figure shows the spectra of two equally sized and spaced scintillators, LYSO and BGO, from a PuBe source with the same 600 second real time acquisition windows. The main difference in the tabulated properties, Table 2.3, of these two scintillators is the decay times, 42 ns for LYSO and 300 ns for BGO. A CsI crystal of the same size was initially evaluated as part of this experiment, however it was abandoned due to the combination of lower density and long decay time. The LYSO crystal was able to process almost an order of magnitude more events than BGO in the same period of time making it more desirable for use in the final system. LaBr exhibits a decay time of 30 ns, similar in magnitude

to LYSO, however it is less dense and will have a lower intrinsic efficiency. This is an interesting trade off but proper evaluation of these two materials against each other would require identical geometries. LaBr is hygroscopic, sensitive to moisture, so it can't be cut, assembled, and evaluated in the lab in the same manner as LYSO.

Performance of all the scintillators is effected by temperature swings as seen repeatedly in measurements conducted in a non-temperature controlled experimental facility. These effects do vary from scintillator to scintillator and are available from the manufacture in product specification documentation. Fluctuations in light output and decay time can not be completely neglected unless the detectors are temperature controlled. On the other hand, the quartz Cherenkov crystals are immune to temperature swings as the refractive index of the material does not change with temperature over environmental ranges. All PMT based detectors may be impacted by temperature induced gain fluctuations and increased noise.

2.6 Imaging Array Considerations and Design

Exploration of the novel active interrogation system concept will use a vertical detector array for imaging as previously shown in Figure 1.2. A prototype array is constructed for testing and evaluation of the proof of concept system. The two main detectors for evaluation purposes here are the 5.08 x 10.16 x 40.64–cm NaI detectors and the 25–mm diameter Cherenkov detectors. The cost of the two types of detectors is vastly different; the Cherenkov detectors can be built for approximately $400 each while the NaI detectors are on the order of $8000 each. Considering the cost of coverage, the Cherenkov detectors are about $160 per vertical centimeter while the NaI detectors are close to $1600 per vertical centimeter.

2.6.1 Spatial Resolution and Object Magnification

The term spatial resolution referred to in this work is the number of pixels used to reconstruct an image. A scanning system utilizing a vertical array of detectors has a fixed

resolution in that dimension based on the number of detectors employed and spacing between them. The array only needs to be a certain height to span the dimensions of the cargo container so the size of the detectors and spacing between them is the main concern. Resolution in the horizontal direction is set by the translation of the object to be imaged in between the source and detector array. Motion of the object can be discrete steps, the object is held in place during irradiation, or it can be continuous where the object position, thus image reconstruction, is a function of time.

If the imaging goal is to resolve an object of a particular size, the magnification of the object must be taken into account. In this type of system, object magnification is a simple matter of trigonometry as shown in Figure 2.11.

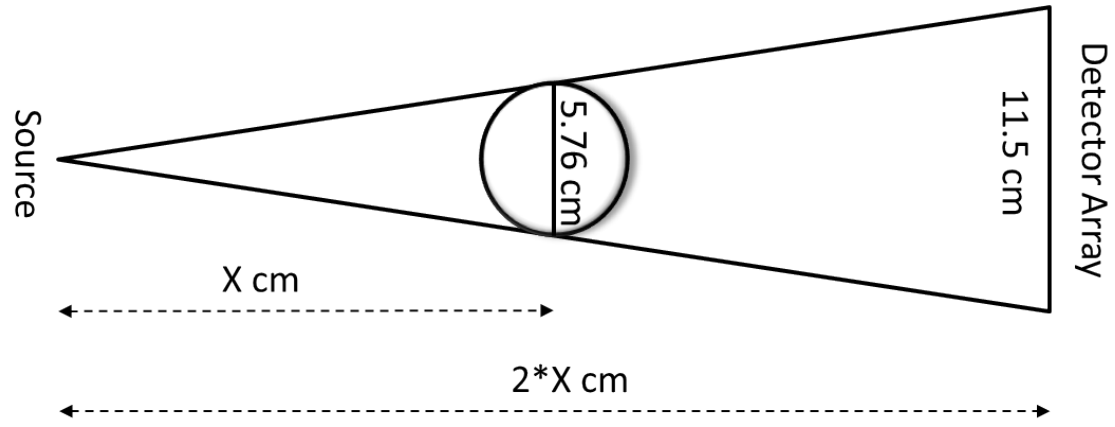

Figure 2.11: Basic concept of geometric magnification of a 100 cm^3 sphere of SNM in transmission imaging where the object is fixed half way between the source and detectors.

The imaging goal here is to be able to resolve a volume of 100 cm^3 of SNM inside the container. If the SNM is exactly in the middle of the source and the imaging array, a valid assumption in this type of system, the size of the shadow cast on the detectors is simply a factor of two of the actual size. Assuming the SNM to be a sphere of the specified volume, the diameter would be 5.76 cm which casts a 11.52 cm shadow on the detectors. The face of the NaI detectors suggested is 5.08 x 10.16 cm, assuming 1 cm separation in between the detectors in the array, the SNM shadow would only fully cover

two detectors at most. This coverage of two detectors, or pixels in the image, assumes the shadows is perfectly cast which is improbable yielding only a single detector fully covered. A 1 cm separation is assumed here for discussion purposes, however this configuration would results in considerable crosstalk, as shown in Figure 2.9, degrading the fidelity of the single pixel measurement. This single pixel many not be enough to definitively confirm the presence of SNM. If an array of the 25–mm Cherenkov detectors with 1 cm separation were used as the imager, the minimum number of detectors covered would be three. A single pixel would be statistically more susceptible to false positives and/or missed material than three pixels combined.

2.6.2 Cherenkov Array Design

A prototype mini-array was constructed for transmission and imaging studies using the proposed low energy nuclear reaction source. This array is based on the 25–mm diameter Cherenkov detector design described in section 2.2 and contains eight detectors vertically aligned with a 5.08 cm center to center pitch. The total height of the detector coverage is 38 cm as seen in Figure 2.12.

The detectors are held by a frame constructed from extruded t-slotted aluminum alloy, commonly referred to as 80/20, and low density insulation sheeting made by Owens Corning, model Foamular 250. The aluminum frame is 6105-T5 alloy (97.2–99% ^{27}Al) and the horizontal supports are wider than the proposed interrogation beam effectively leaving the detectors suspended in the low density insulating foam. The quartz crystals protrude from the foam in the direction of the incident beam yielding a support structure that will not cause scattering effects from the high energy gamma rays.

Figure 2.12: Photographs of prototype Cherenkov detector based imaging array with a 5.08 cm center-to-center detector pitch and constructed from lightweight aluminum framing and low density insulating foam.

CHAPTER 3

ACTIVE INTERROGATION SOURCES

Passive detection methods often fall short of consistently and effectively detecting special nuclear material, especially when shielded with high-Z material. Most passive interrogation methods rely on the inherent radioactivity of the material, generally low energy gamma ray emissions. These gamma rays do not easily penetrate surrounding material leaving them essentially invisible to radiation detectors outside of a cargo container. One "passive" method that is showing some promise is muon tomography [33]. This technique relies on tracking cosmic muon interactions with material inside the cargo container by arrays of detectors on the outside of the container. However, this method relies on events that are relatively rare meaning long interrogation times. Most images published to date take days to accumulate enough data for image reconstruction. At that rate, it would be faster to physically open and inspect each container manually which is just not an option in the fast pace of global cargo shipping which has a requirement for two-minute scans per 40-foot container [2, 3, 4].

To solve this problem, we need to use an external source of radiation in order to create or amplify the characteristic signatures from the material, a method referred to as active interrogation [5]. Active interrogation with neutron sources has been demonstrated [12], but can lead to significant doses to the cargo and potential stowaways. In addition to dose issues, there is a concerning probability of neutron induced activation in the interrogated material. For the purposes of this thesis, the discussion will be limited to sources consisting of photons or mixed fields of photons and neutrons for active interrogation. The most commonly used photon source for active interrogation is bremsstrahlung beams; however, recent advancements in alternative sources such as Inverse Compton (IC) and low energy nuclear reactions are showing promise.

The physics of bremsstrahlung-based sources is well understood and can be implemented in a fairly straight forward manor. Bremsstrahlung, or "braking", radiation is electromagnetic emission produced by acceleration, or deceleration, of a charged particle passing through the electric and magnetic fields of a nucleus. Most commonly this is done by accelerating electrons using a linear accelerator and impinging them on a metal target such as tungsten. The resulting emission is in the form of x-rays in a broad, continuous energy spectrum dictated by the energy of the incident electrons. A source can be pulsed with two different energy electrons to produce a time gated, "dual-energy" photon spectrum as seen in Figure 3.1.

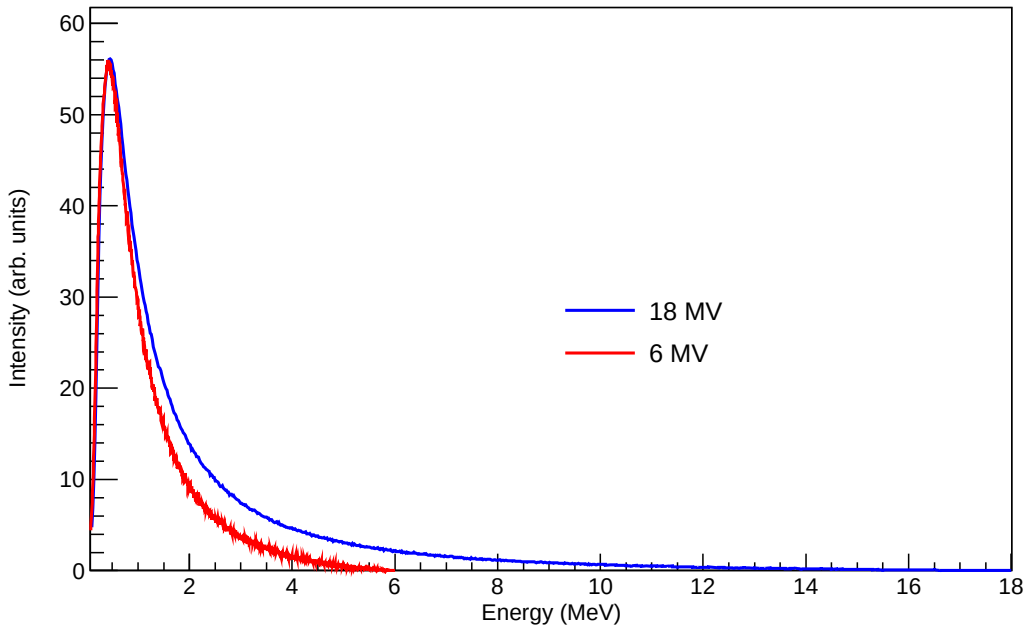

Figure 3.1: Simulated x-ray energy spectra of bremsstrahlung beams. Both beams show significant concentration in the lower energy range that is poorly penetrating and largely contributes to dose.

One major drawback to this type of source is the continuous nature of the energy emitted. A spectrum is identified by the end point energy even though that is where the minimum number of emissions occur. Most of the photons emitted are in the lower portion

of the energy spectrum which are not highly penetrating, therefore they have a significant contribution to the dose delivered to the interrogated object with respect to the portion that traverses the material and can be counted. Another concern arises when considering Compton scattering in the interrogated material, which can affect the signal to noise ratio of a detection system. It is difficult to determine whether a detected photon is the result of transmission through the object or in-scatter from an interaction elsewhere in the object. The process in which bremsstrahlung radiation is emitted generally involves only photons, but sources with enough energy can produce photoneutrons. Measurements of an 18 MV beam produced by a Varian Clinac have shown substantial neutron production recorded by using a 6-inch BF_3 thermal neutron counter. The neutron tube was placed 2 meters outside of the beam line and recorded just over 35,000 counts in 5 seconds of operation. Simple yet practical imaging implementations have been demonstrated [34] including detection methods based on nuclear resonance fluorescence [35, 36]. However, the dose associated with broad energy spectrum of bremsstrahlung and elemental identification issues remain to be addressed.

One alternative showing promise in lab settings is Inverse Compton scatter [37, 38, 36, 35], where a powerful beam of accelerated electrons is crossed with an intense laser beam causing the photons to scatter off the relativistic electrons, gaining energy. To form a somewhat viable source, both beams must be incredibly intense in order to account for the low interaction probability. The physics at play here is simply Compton Scattering in reverse of what we usually think of, but that means there is a distribution of up-scattered photon energies dependent upon the angle of scatter. Photons of somewhat discrete energy can be extracted by tuning the energy of the electrons and selecting an angle of scatter using shielding. This technique generally requires large footprints and power requirements for the necessary equipment: lasers, optics, high vacuum chambers, accelerators, etc. Currently this type of source is only capable of producing pencil beams of high energy photons in a lab setting and is not a viable option for a full scale scanning system until more ad-

vancements are made.

Another alternative source of particular interest is low energy nuclear reactions [39, 6, 40], where accelerated ions impinge upon a target nuclei to produce gamma rays. This type of source is capable of producing highly penetrating discrete energy photons, gamma rays, of varying energies as well as neutrons depending on the reaction. The modality of radiation produced can be selected with clever choices of ion type and energy as well as proper target nuclei. This technique is frequently used in subcompact systems with very low ion kinetic energies as a source of neutrons, D-D and D-T generators. For photon generation one could use ions — protons, deuterons, alpha particles, Li^{-}, or others — accelerated to MeV range kinetic energies by compact linear accelerators or cyclotrons [39] before interacting with a target. For the purposes of this thesis, the focus will be on low energy nuclear reactions including their challengers, characterization, and potential applications. In particular, a novel investigation will be presented into a low energy nuclear reaction of interest, the ^{11}B(d,nγ)^{12}C, based on observed nuclear transitions via gamma ray emission.

3.1 Deuteron Induced Reactions in Boron

Reactions such as ^{11}B(d,nγ)^{12}C are highly dependent upon the incident particle energy, determining which nuclear states are achieved and the abundances of those states. De-excitation of a ^{12}C nucleus is famous for emitting a 4.4–MeV gamma ray from PuBe and AmBe sources via ^{9}Be(α,nγ)^{12}C reactions. That state and others can be reached through interactions with deuterons as well. Figure 3.2 depicts the possible excited states of ^{12}C, however not all of the states are achievable through deuteron reactions.

Of particular interest for highly penetrating gamma rays is the 15.1–MeV state of ^{12}C, which emits a 15.1–MeV gamma ray in the return to ground state through a strong M1 emission. However, population of the 15.1–MeV state is a threshold reaction where the deuteron must have a kinetic energy of at least 1.633 MeV, otherwise the 12.7–MeV state is preferentially populated [6]. Increasing the energy of the deuteron leads to a higher

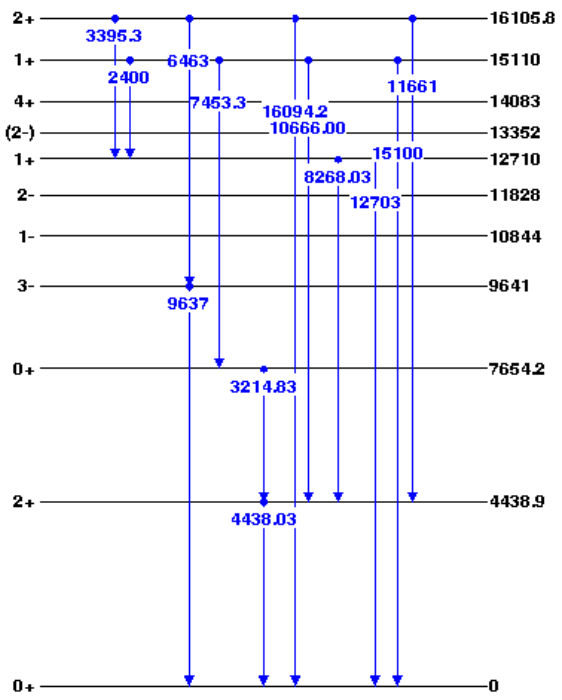

Figure 3.2: Energy level diagram of possible known nuclear states of ^{12}C (black) and gamma ray emission (blue) during de-excitation to the ground state. Nucleon decay modes are possible from many of these states but are omitted here.

yield of the 15.1–MeV state population relative to the 12.7– MeV state. Investigations in to the ^{11}B(d,nγ)^{12}C reaction date back to the 1950s where the main focus was on the cross section of populating the 15.1–MeV state as a function of incident deuteron energy. The cross section has varied wildly over the years with subsequent studies, however they all find a fairly broad resonance around 3.08–MeV [41, 42, 6]. Another important result of their work shows the angular distribution of the gamma rays is essentially isotropic in the LAB system with deuterons around 3.25 MeV; however, angular dependence is more pronounced at higher deuteron energies.

Recent efforts by Taddeucci et al. [6] have employed relatively modern equipment and techniques to measure the cross section of populating the 15.1–MeV state as well as the resulting neutron and gamma ray spectra. They used a range of deuteron energies from 3.00-7.44 MeV accelerated by a 4.5-MeV tandem Van de Graaff accelerator and beam-swinger facility [43] at the Ohio University John E. Edwards Accelerator Laboratory. A

highly efficient 10.16 x 10.16–cm BGO detector was employed to collect data from an enriched ^{11}B target subjected to 5-50 nA of beam current. The experiment was performed by collecting all gamma rays incident on the detector and again with a 32 ns time of flight (TOF) gating to look at only prompt gamma rays. Here, they were able to show the only prompt gamma ray emissions were the 4.4 and 15.1-MeV lines from ^{12}C, all the other gamma rays observed in the non-TOF gated experiments nearly vanished. However, it is important to note that they imposed an artificial (electronics based) low energy threshold, so the entire spectrum is not presented nor is it energy calibrated. Only the two major ^{12}C lines, 4.4 and 15.1 MeV, are discussed with any certainty in their work as they were mostly interested in the cross section, yields, and neutron spectrum. However, applications such as active interrogation can not afford to ignore any radiation that can be used to reduce scan time, effect dose to the interrogated object, or be used for techniques such as material identification. Gamma de-excitations from high energy levels have half-lives in the femto-second range, so some other processes must be responsible for the gamma rays in between 4.4 and 15.1 MeV.

3.2 Accelerator and Experimental Setup

There are a multitude of technologies that can be used to accelerate deuterons capable of reaching the 15.1 MeV state of ^{12}C. However, there is a tradeoff between accelerator size and beam current for most of them. There is a need for a system capable of sufficient beam current for scanning applications, but also small enough to be able to effectively shield and collimate the output into a fan beam. One option is to use a modified LANSAR Model DL-3 radiofrequency quadrupole accelerator (RFQ) manufactured by Accsys Technology Inc. and located at the Massachusetts Institute of Technology Bates Research and Engineering Center (Middleton, Massachusetts). The accelerator produces a 3.02-MeV deuteron beam with versatile pulse rates and widths, delivering an average current of up to 90 μA at up to 800 Hz repetition rate with a duty cycle of up to 1.6% according to the factory acceptance

test [44], a summary of this document can be found in Table 3.1.

Table 3.1: DL-3 Operating Specifications.

Parameter Description	Measured Value
Output d^+ beam energy	$3.02\,\text{MeV}$
Beam pulse width	$2 - 150\,\mu\text{s}$
Beam repetition rate	$80 - 800\,\text{Hz}$
Max RF duty factor	1.6%
Output beam current pulsed	$6 - 10\,\text{mA}$
Beam diameter at target entrance	$10\,\text{mm}$
Vacuum pressure	$3 \times 10^{-7}\,\text{torr}$
Average current	$1 - 90\,\mu\text{A}$
RF fill time	$5 - 6\,\mu\text{s}$

A continuous working (CW) accelerator would be beneficial for a production grade system to eliminate the "wasted" time in between pulses depending on the goal of the detection system. If detection systems for delayed neutrons and gamma rays are employed in addition to an imaging system, then a pulsed machine is preferable. For this investigation and proof of concept system, it makes no difference which mode of operation is employed as long as it can produce sufficient beam current.

Multiple target designs were tested as part of the project including thin (micron range) enriched ^{11}B as well as "thick" (2 mm) natural boron targets. Most research in this reaction has employed a high purity, enriched boron target, usually 99.9% ^{11}B, to focus on the cross sections to populate the most desired excited states. Originally, the plan for this work was to use such a target; however, two targets were quickly destroyed due to the heat build up from the impinging deuterons before the work in this thesis could be conducted. From now on, this investigation will focus on the 2–mm thick natural boron target with an approximate ^{10}B isotopic abundance of 19.9% and ^{11}B isotopic abundance of 80.1%. This target was purchased from Goodfellow USA, part number 433911/2, and measures 25 mm by 25 mm. The boron was fastened to a high vacuum aluminum end cap using a custom machined steel flange as shown in Figure 3.3.

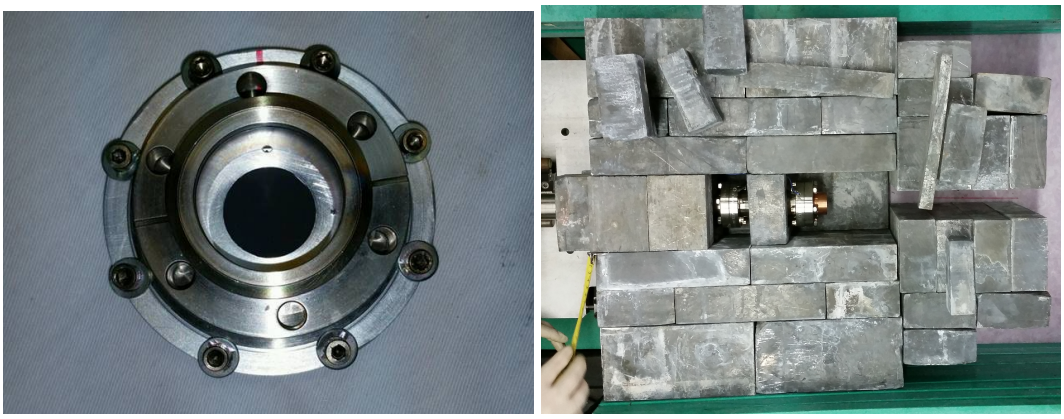

Figure 3.3: (Left) Assembled natural boron target affixed to an aluminum end cap before installation. (Right) Previous target holder assembled to RFQ depicted here to show the target is surrounded by lead for collimation. Deuterons enter from the left and the imaging space is far to the right.

The presence of ^{10}B in the natural material expands the possibilities of potential nuclear reactions that can take place and must be accounted for. It is crucial to understand the exact energies of the gamma rays resulting from the nuclear reaction in the target as well as other interactions in the experimental setup. Further complicating the potential reaction list is the aluminum end cap. Aluminum is frequently used in thin quantities for detector deconstruction because it is relatively opaque to gamma rays and mildly resistant to neutron interactions that go on to cause gamma rays in most general laboratory situations. However, this reaction is known to result in neutrons reaching as high as 16.5 MeV, so those reactions must be explored as well.

The target holder on the end of the accelerator is surrounded by multiple layers of lead and borated poly to collimate the resulting isotropic radiation into a fan beam. The accelerator itself is housed in a warehouse that does not have any shielding and is not temperature controlled. The lack of shielding of the building to the outside dictated that extra shielding be added all the way around the target to ensure all areas outside the building were below public dose limits. This also introduces a limit of the allowable beam current which will be discussed later. This lead cave around the target is surrounded with 5% borated poly in all directions, approximately 18 inches on top, 12 inches on the bottom,

and 48 inches on the sides as seen in Figure 3.4.

Figure 3.4: Photograph of shielding surrounding the boron target on the end of the accelerator. The RFQ section of the accelerator is on the far left, deuterons are accelerated into the boron target buried beneath the borated poly. The resulting radiation is collimated using large, high density concrete blocks shown on the far right.

Expanding out further from the target is mostly open space in the warehouse except the direction of the detectors where multiple rows of large concrete blocks are stacked as collimators and shields. The shielding in close proximity to the target coupled with empty space in the directions of non-interest drastically helps reduce room scatter and activation from materials in the environment. A scale drawing of the collimation and area of interest can be found in Figure 3.5.

This configuration produces a mock-up of a potential system that is more sophisticated than a typical laboratory experiment, yet not quite production scale. The two sets of large concrete collimator blocks together with the lead cave shown in Figure 3.3 produce a fan beam in the direction of the detector area that is calculated to be a divergence angle of 8.62 mrad (horizontal) and 276 mrad (vertical). The multiple layers of collimation are ideal for transmission measurements because anything interacting in the material will most likely

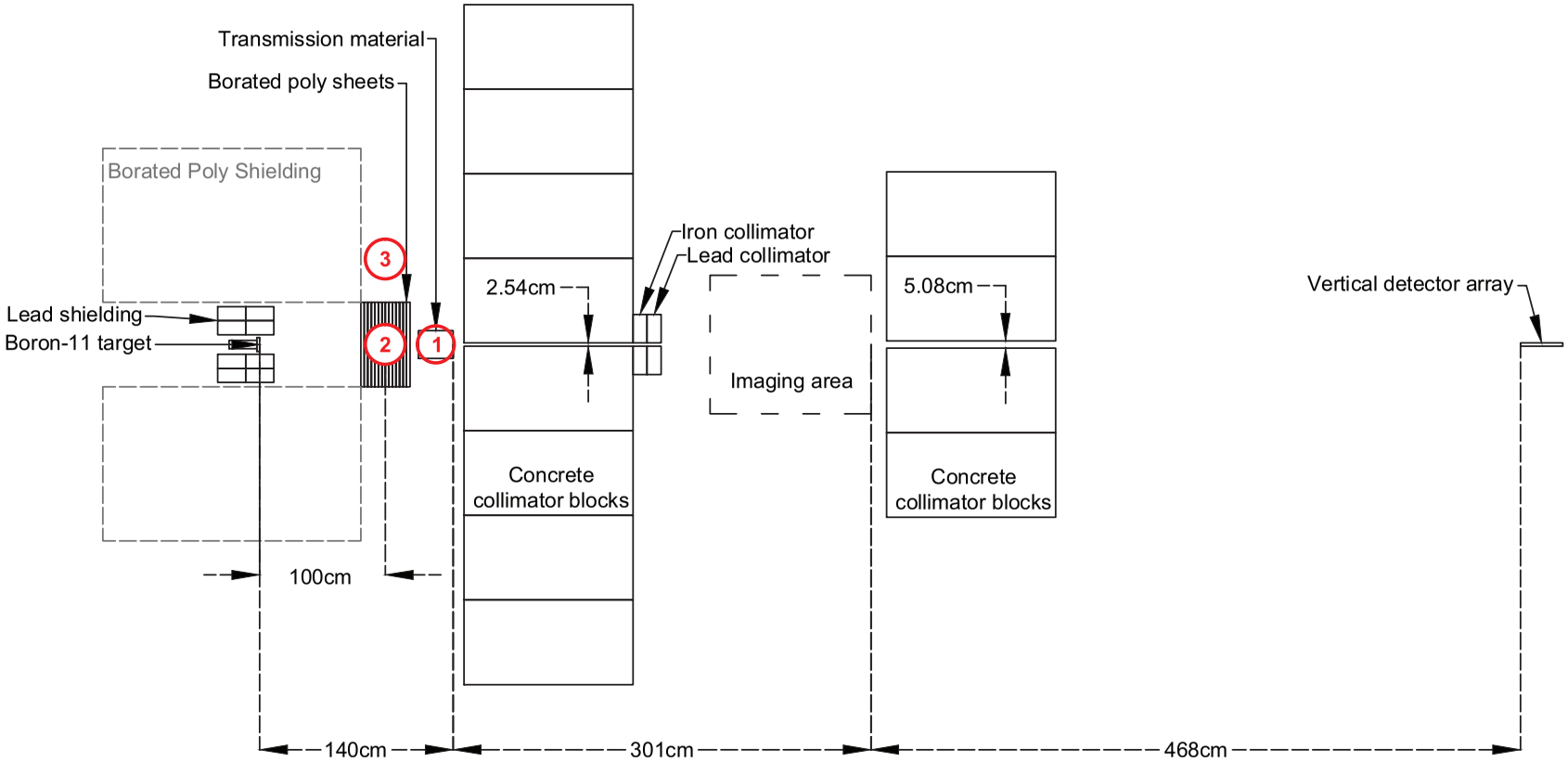

Figure 3.5: Schematic, drawn to scale, showing the main components and shielding of the experimental hall at Bates Research and Engineering Center in Middleton Massachusetts. (1) represents the location of the pure materials for transmission based experiments. (2) denoted the optional neutron filter made from 5% borated poly and variable from 1 – 21 inches. (3) location of observation for delayed gamma ray and neutron radiation from fissions in SNM. The location denoted as the vertical detector array is also the location of single detector work for consistency.

be scattered out of the small solid angle that will reach the detectors. This configuration includes a variable neutron filter, denoted as location 2, which consists of 2.54–cm thick sheets of 5% borated poly stacked such that the thickness of the sheets are oriented vertically. All sheets can be removed to have a purely unimpeded beam to the detectors, or up to 21 sheets can be added to reduce the neutron flux to the experiment. This low-Z filter does an excellent job of removing neutrons from the beam, yet has little effect on the flux of high energy gamma rays of interest.

All the detectors used as part of this thesis were located in approximately the same location as shown in Figure 3.5. Many measurements have been made at various locations, and this one was determined to the optimal for collimation, scatter, and other factors. It is important to keep the location of all competing detection systems the same for a fair comparison. The relationship between the detectors and the location of object transmission studies, location 1, is also important to ensure the small test objects cast a complete shadow on entire height of the imaging arrays.

The accelerator, target, and environmental set up are discussed in such detail here to aid the discussion about the origin of observed gamma rays not resulting from the known ^{12}C states. As mentioned earlier, all research thus far has focused more on the cross section of the ^{11}B(d,n$\gamma_{15.1}$)^{12}C reaction, which is generally assumed to be the predominant reaction. However, we must understand the entire product output if we are to use it effectively.

3.3 Simulated Reactions with Geant4

To begin the investigation in to the details of the source we need to start with simulations to gain a glimpse in to what *could* be taking place. The Monte Carlo based Geant4 toolkit [45, 46] provides a flexible framework for the simulation of particle transport and interaction with matter. It is a robust tool that can easily be tailored to use multiple physics models for particle interaction or tabulated cross sections.

A model was created to simulate deuteron interactions in a natural boron target. This

model specifically considers the nuclear reactions taking place inside the target materials to find out what is generated. The geometry includes a large natural boron target, 4 cm cube, in vacuum and an isotropic deuteron point source in the center of the boron. While this is not a realistic representation of the experimental setup, it is intended to investigate potential reactions happening inside the boron target itself.

The physics lists used in the simulation have been varied to look for variations in the predicted nuclear reactions. All simulations conducted used some combination of the following physics modules:

1. G4HadronElasticPhysicsHP
2. G4HadronPhysicsFTFP_BERT_HP
3. G4HadronPhysicsQGSP_BIC_HP
4. G4HadronInelasticQBBC
5. G4HadronPhysicsINCLXX
6. G4IonElasticPhysics
7. G4IonPhysics
8. G4IonINCLXXPhysics
9. G4DecayPhysics
10. G4RadioactiveDecayPhysics
11. G4EmStandardPhysics
12. GammaPhysics

Repeated simulations varying the combinations of these physics lists did not have a significant effect on the predicted nuclear reactions. The results reported in this thesis use items 1, 2, 6, 7, 11, 12. Geant4 gives access to the processes taking place at every level, so we are able to tally and track the entire cascade of nuclear reactions taking place in the target as well as the energy distribution of particles produced. Tracking of electrons and positrons was turned off for simulations as they do not add to the nuclear reactions, but they

do add significant overheads to computation time. The simulation employs 10^9 deuterons incident on the target which yielded a total of 687 possible nuclear reactions including cascades. A summary of these reactions can be found in Table 3.2 where reactions occurring less than 0.5% of the total rate of emission (occurrence) are omitted. A complete list can be found in Table A.3 in Appendix A.

Table 3.2: Nuclear reactions and abundance greater than 0.5% as calculated by Geant4. Q-value based on mass balance only. See Appendix A for the full list.

Reaction	Relative Yield (%)	Q-value
n + ^{11}B $\rightarrow$ n + ^{11}B	35.522	
d + ^{11}B $\rightarrow$ n + 3 α	34.764	6.459 MeV
d + ^{11}B $\rightarrow$ γ + n + ^{12}C	26.127	13.732 MeV
d + ^{11}B $\rightarrow$ α + ^{9}Be	9.113	8.032 MeV
n + ^{10}B $\rightarrow$ n + ^{10}B	7.918	
d + ^{10}B $\rightarrow$ γ + p + ^{11}B	7.302	9.230 MeV
d + ^{10}B $\rightarrow$ γ + n + ^{11}C	6.984	6.465 MeV
d + ^{11}B $\rightarrow$ d + ^{11}B	5.245	
p + ^{11}B $\rightarrow$ p + ^{11}B	4.516	
n + ^{11}B $\rightarrow$ γ + n + ^{11}B	3.715	
d + ^{11}B $\rightarrow$ γ + p + ^{12}B	3.567	1.146 MeV
α + ^{11}B $\rightarrow$ α + ^{11}B	2.753	0.0006 eV
d + ^{10}B $\rightarrow$ d + ^{10}B	2.316	
α + ^{11}B $\rightarrow$ n + ^{14}N	1.540	157.230 keV
d + ^{11}B $\rightarrow$ p + ^{12}B	1.417	1.146 MeV
p + ^{10}B $\rightarrow$ p + ^{10}B	1.224	
d + ^{11}B $\rightarrow$ n + ^{12}C	1.211	13.732 MeV
n + ^{11}B $\rightarrow$ γ + n + α + ^{7}Li	1.149	-6.485 MeV
d + ^{10}B $\rightarrow$ p + ^{11}B	1.009	9.230 MeV
d + ^{10}B $\rightarrow$ n + ^{11}C	0.942	6.465 MeV
n + ^{10}B $\rightarrow$ γ + α + ^{7}Li	0.862	2.790 MeV
n + ^{10}B $\rightarrow$ γ + n + ^{10}B	0.856	
d + ^{10}B $\rightarrow$ 3 α	0.823	17.913 MeV
α + ^{11}B $\rightarrow$ γ + n + ^{14}N	0.819	157.230 keV
d + ^{10}B $\rightarrow$ γ + d + ^{10}B	0.678	
n + ^{10}B $\rightarrow$ α + ^{7}Li	0.604	2.788 MeV
α + ^{11}B $\rightarrow$ p + ^{14}C	0.439	783.570 keV

The accuracy of the exact ratio of reactions occurring is not experimentally validated. It is well known that some tabulated cross sections and nuclear data are missing affecting

all simulation tools including MCNP. It is important to note that the Q-value presented here is based solely on rest mass and does not include kinetic energy from the incident particle itself as shown in Equation 3.1.

$$Q = (m_{initial} - m_{final}) * 931.502 \tag{3.1}$$

For example, the Q-value for the ^{11}B(d,nγ)^{12}C is calculated as 13.73 MeV which is not enough to populate the 15.1–MeV state of ^{12}C. However, when adding the possible energy from the deuteron the $Q_{excited}$ is calculated to be 16.28 MeV which can overcome the threshold and reach the 15.1–MeV excited state under the right conditions. The kinetic energy of the incident particle is included in the simulation; however, the $Q_{excited}$-value would change as the particle slows in the material. Another important note about this table and Q-value is that nearly all of the resulting nuclei are in an ionized state, so nucleons and electrons must be conserved such as the ^{11}B(d,nγ)^{12}C Q-value calculation shown in Equation 3.2.

$$Q = (2.01355321 + 11.009305 - 12.0 - 0.0005485803 - 1.00866501) * 931.502 = 13.732 MeV \tag{3.2}$$

The second, third, and fourth reactions listed are competing processes that determine the population of the 15.1–MeV state of ^{12}C. There is no claim here of these percentages being strictly correct, but they give an estimate to compare with observed experimental data. The processes in Geant4 chronologically handle nucleon decay before gamma decay, but the nuclear data for this reaction is not reliable. If there are no excited state population data and gamma emission probabilities available, then it will only de-excite through nucleon decay.

One important result of this simulation is the abundance of the ^{11}B(d,n)3α, occurring nearly 34% of the time from incident deuterons. This is significantly higher than expected

and turns out to be the most prominent nuclear reaction occurring per this simulation, which does not directly add to the desired high energy gamma ray output. However, this reaction could be the summed total of that reaction and the emission of a neutron and 15.1–MeV gamma ray. The next most probable reaction is the desired ^{11}B(d,nγ)^{12}C reaction followed by the ^{11}B(d,α)^{9}Be reaction resulting in a 1.68–MeV gamma ray. The resulting particles generated from these reactions can be found in Table 3.3.

Gamma ray production is omitted from this list due to the lack of tabulated emission intensities, branching ratios, and even available energy states in some cases. This is a known limitation of available nuclear data which may be explored experimentally in the future work of this project. In fact, conversations with the Geant4 development team have resulted in them independently recreating the results and verifying the nuclear data needed to specify population of the 15.1–MeV state and subsequent gamma emission of ^{12}C is missing. The kinetic energy of each particle generated is tabulated at the time of emission to build energy histograms as seen in Figure 3.6.

The non-continuous nature of the distributions is because of the tally at time of origin and includes stripping reactions. Here, we can see Geant4 is accounting for thresholds of emissions by the step-like functions. The energy of an emitted particle can be continuous between a minimum threshold and a threshold of a different reaction. Again, this is not necessarily 100% correct but is meant to give a visual representation of the problem. There are an enormous amount of particles generated inside the target itself that can spawn other reactions that go on to yield gamma rays. Generally, this will take longer than 32 ns from the time of the ^{12}C prompt gamma emissions suggesting a possible source of the intermediate energy gamma rays.

The charged particles will not likely make it out of the target material, but the neutron will. Once they escape the boron target, they will have the potential to interact with the aluminum endcap to which the boron target is fixed, essentially half of the neutrons will face the aluminum end cap as it covers a 2π solid angle in the direction of the detectors. A

Table 3.3: Summary of particles generated per 10^9 and kinetic energy range as calculated by Geant4 at the time of emission. % Resulting is the number of particles generated divided by the number of incident neutrons multiplied by 100. See Appendix A for the full list.

Particle	# generated	Avg. Energy	Energy Range
^{10}B	13.679	611.61 keV	0.009 eV $\rightarrow$ 20.545 MeV
^{11}B	60.435	635.07 keV	0.002 eV $\rightarrow$ 22.289 MeV
^{12}B	4.985	636.23 keV	159.43 eV $\rightarrow$ 10.236 MeV
^{9}B	0.001	1.15 MeV	2.775 keV $\rightarrow$ 3.513 MeV
^{10}Be	0.145	1.60 MeV	70.28 eV $\rightarrow$ 12.991 MeV
^{11}Be	0.017	1.32 MeV	256.54 keV $\rightarrow$ 3.809 MeV
^{7}Be	0.070	596.25 keV	67.268 eV $\rightarrow$ 11.295 MeV
^{8}Be	0.042	4.09 MeV	661.48 eV $\rightarrow$ 12.535 MeV
^{9}Be	9.253	3.55 MeV	121.81 eV $\rightarrow$ 19.993 MeV
^{10}C	0.004	946.02 keV	70.393 keV $\rightarrow$ 4.4406 MeV
^{11}C	7.945	749.43 keV	5.025 eV $\rightarrow$ 15.736 MeV
^{12}C	27.688	961.08 keV	75.23 eV $\rightarrow$ 22.132 MeV
^{13}C	0.596	1.78 MeV	129.86 eV $\rightarrow$ 14.691 MeV
^{14}C	0.463	1.58 MeV	7.542 keV $\rightarrow$ 15.097 MeV
^{3}He	0.006	3.98 MeV	36.39 keV $\rightarrow$ 14.749 MeV
^{6}He	0.001	2.60 MeV	28.845 keV $\rightarrow$ 15.411 MeV
^{6}Li	0.004	4.43 MeV	254.21 eV $\rightarrow$ 22.014 MeV
^{7}Li	2.732	1.69 MeV	65.774 eV $\rightarrow$ 17.2 MeV
^{8}Li	0.181	2.28 MeV	148.97 eV $\rightarrow$ 8.607 MeV
^{13}N	0.103	1.63 MeV	10.873 keV $\rightarrow$ 13.244 MeV
^{14}N	2.360	1.59 MeV	18.464 keV $\rightarrow$ 15.28 MeV
^{15}N	0.003	3.14 MeV	4.152 keV $\rightarrow$ 14.997 MeV
^{16}O	0.002	2.60 MeV	71.161 keV $\rightarrow$ 16.613 MeV
^{17}O	0.002	2.83 MeV	121.98 keV $\rightarrow$ 16.175 MeV
α	123.732	2.68 MeV	1.129 eV $\rightarrow$ 38.425 MeV
d	8.596	2.23 MeV	1.090 keV $\rightarrow$ 25.033 MeV
n	78.545	6.42 MeV	3.654 eV $\rightarrow$ 30.857 MeV
p	14.672	4.86 MeV	177.12 eV $\rightarrow$ 26.038 MeV
t	0.560	2.57 MeV	3.442 eV $\rightarrow$ 31.807 MeV

similar simulation used 2 cm of pure aluminum (natural) metal at the target of high energy neutrons to produce Tables 3.4 and 3.5.

Table 3.4 represents a portion of the total reactions predicted by the simulation. A complete list can be found in Appendix A. This simulation uses the ENDF/B-VII.1 cross section library. Additional libraries were evaluated including JENDL and TENDL, all hav-

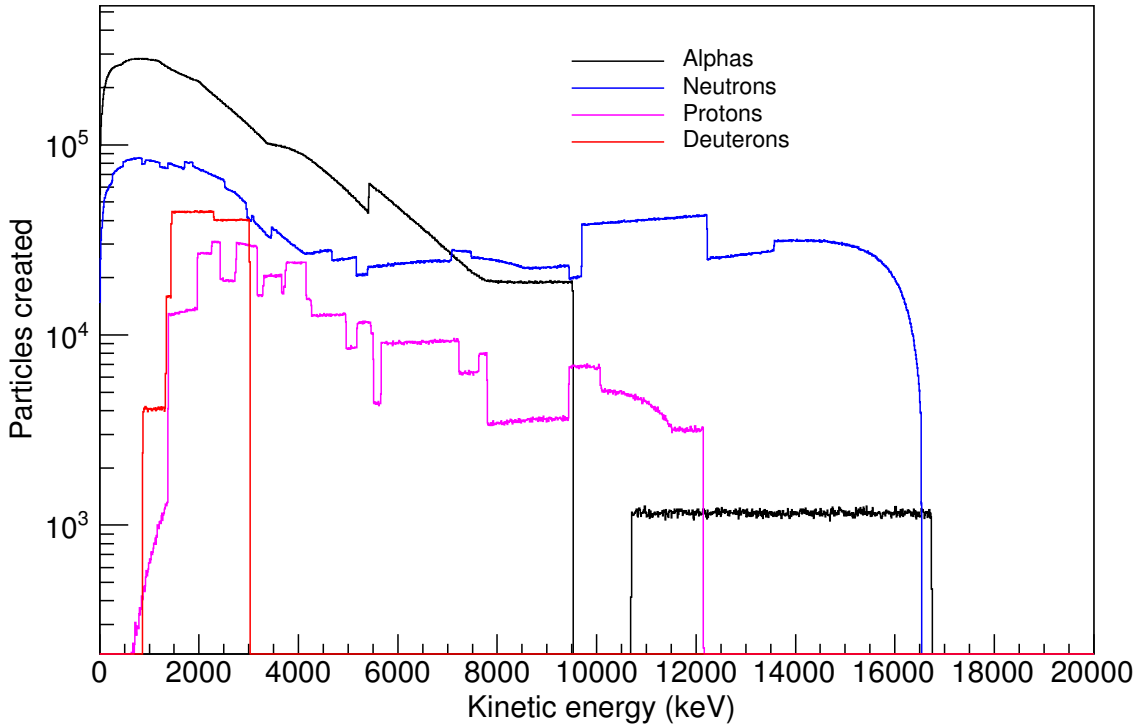

Figure 3.6: Kinetic energies of some of the reaction products at the instant of emission including stripping reactions. As the particles propagate through the target material they slow down and/or cause other reactions to occur.

ing approximately the same results. The gamma ray energies produced were again omitted from the tabulated results.

These simulations are meant to illustrate the complexity of the current accelerator and target system as most of the previous investigation in to this type of source has used enriched ^{11}B targets.

3.4 Experimental Beam Studies

Measurements of the ^{nat}B(d,nγ)^{12}C low energy nuclear reaction produced from 3.02–MeV deuterons have been completed at Bates Research and Engineering Center in Middleton, Massachusetts. A variety of detectors were used in multiple studies at the facility including HPGe, LaBr, custom Cherenkov, and Ej-309 as well as others that are neglected because

Table 3.4: Nuclear reactions and abundance greater than 0.01% as calculated by Geant4 from 16.1–MeV neutrons in ^{27}Al. Q-value based on mass balance only. See Appendix A for the full list.

Reaction	Relative Yield (%)	Q-value
n + ^{27}Al $\rightarrow$ n + ^{27}Al	47.479	
n + ^{27}Al $\rightarrow \gamma$ + n + ^{27}Al	14.799	
n + ^{27}Al $\rightarrow \gamma$ + p + n + ^{26}Mg	13.962	-6.681 MeV
n + ^{27}Al $\rightarrow \gamma + \alpha$ + ^{24}Na	3.835	-2.236 MeV
n + ^{27}Al $\rightarrow$ p + n + ^{26}Mg	2.494	-8.293 MeV
n + ^{27}Al $\rightarrow \gamma$ + p + ^{27}Mg	2.410	-1.082 MeV
p + ^{27}Al $\rightarrow$ p + ^{27}Al	1.663	
n + ^{27}Al $\rightarrow \gamma$ + 2 n + ^{26}Al	1.654	-11.996 MeV
n + ^{27}Al $\rightarrow \gamma$ + n + α + ^{23}Na	1.469	-8.854 MeV
n + ^{27}Al $\rightarrow \gamma$ + d + ^{26}Mg	1.398	-5.891 MeV
n + ^{27}Al $\rightarrow$ n + α + ^{23}Na	1.220	-9.377 MeV
n + ^{27}Al $\rightarrow$ 2 n + ^{26}Al	1.184	-12.745 MeV
α + ^{27}Al $\rightarrow \gamma$ + n + ^{30}P	0.301	-2.645 MeV
p + ^{27}Al $\rightarrow \gamma$ + p + ^{27}Al	0.217	-36.281 keV
n + ^{27}Al $\rightarrow \gamma$ + t + ^{25}Mg	0.185	-10.836 MeV
n + ^{27}Al $\rightarrow \alpha$ + ^{24}Na	0.148	-3.131 MeV
d + ^{27}Al $\rightarrow \gamma$ + n + ^{28}Si	0.144	9.360 MeV
n + ^{27}Al $\rightarrow$ d + ^{26}Mg	0.112	-6.046 MeV
n + ^{27}Al $\rightarrow$ t + ^{25}Mg	0.077	-10.882 MeV
α + ^{27}Al $\rightarrow \gamma$ + p + ^{30}Si	0.070	2.371 MeV
n + ^{27}Al $\rightarrow$ p + ^{27}Mg	0.050	-1.827 MeV
n + ^{27}Al $\rightarrow \gamma$ + ^{28}Al	0.032	13.487 MeV
d + ^{27}Al $\rightarrow \gamma$ + p + ^{28}Al	0.023	5.501 MeV
p + ^{27}Al $\rightarrow \gamma + \alpha$ + ^{24}Mg	0.017	1.566 MeV
α + ^{27}Al $\rightarrow \gamma + \alpha$ + ^{27}Al	0.012	
t + ^{27}Al $\rightarrow \gamma$ + n + ^{29}Si	0.011	11.576 MeV

they do not add any value to this discussion.

One of the major challenges of these measurements is the energy calibrations of the detectors due to the lack of radioisotopes naturally emitting gamma rays above the 2.6–MeV emission of ^{208}Tl, a product of the ^{232}Th decay chain. Techniques involving nuclear reactions need to be used to reach higher energies such as sources like plutonium beryllium (PuBe) or americium beryllium (AmBe) which produce the same 4.4–MeV state of ^{12}C as the our accelerator based source. This is a useful surrogate for many applications; however,

Table 3.5: Summary of particles generated and kinetic energy range as calculated by Geant4 at the time of emission. % Resulting is the number of particles generated divided by the number of incident neutrons multiplied by 100. See Appendix A for the full list.

Particle	% Resulting	Avg. Energy	Energy Range
^{26}Al	2.838	657.76 keV	(62.019 eV $\rightarrow$ 2.353 MeV)
^{27}Al	64.180	404.68 keV	(0.001 eV $\rightarrow$ 5.278 MeV)
^{28}Al	0.056	541.51 keV	(0.574 eV $\rightarrow$ 2.294 MeV)
^{29}Al	0.001	532.68 keV	(3.067 keV $\rightarrow$ 1.835 MeV)
^{3}He	2.24e-5	4.750 MeV	(2.762 MeV $\rightarrow$ 7.419 MeV)
^{24}Mg	0.017	1.369 MeV	(58.512 keV $\rightarrow$ 4.533 MeV)
^{25}Mg	0.266	934.73 keV	(20.029 eV $\rightarrow$ 4.497 MeV)
^{26}Mg	17.966	778.24 keV	(10.856 eV $\rightarrow$ 3.530 MeV)
^{27}Mg	2.460	885.02 keV	(2.109 keV $\rightarrow$ 2.174 MeV)
^{23}Na	2.689	1.263 MeV	(9.210 eV $\rightarrow$ 4.812 MeV)
^{24}Na	3.983	1.785 MeV	(974.89 eV $\rightarrow$ 4.444 MeV)
^{23}Ne	1.13e-5	868.03 keV	(5.398 keV $\rightarrow$ 2.537 MeV)
^{30}P	0.301	1.085 MeV	(305.43 keV $\rightarrow$ 3.106 MeV)
^{31}P	0.001	871.46 keV	(542.72 keV $\rightarrow$ 1.841 MeV)
^{27}Si	0.007	396.14 keV	(39.447 keV $\rightarrow$ 1.473 MeV)
^{28}Si	0.151	454.90 keV	(53.272 eV $\rightarrow$ 2.876 MeV)
^{29}Si	0.011	528.17 keV	(232.33 eV $\rightarrow$ 2.886 MeV)
^{30}Si	0.070	1.175 MeV	(172.42 keV $\rightarrow$ 3.479 MeV)
α	6.705	6.561 MeV	(359.24 keV $\rightarrow$ 14.453 MeV)
d	1.511	5.519 MeV	(17.785 keV $\rightarrow$ 10.445 MeV)
n	40.101	4.825 MeV	(0.392 eV $\rightarrow$ 19.742 MeV)
p	19.237	4.121 MeV	(2.743 eV $\rightarrow$ 15.805 MeV)
t	0.262	3.361 MeV	(181.68 keV $\rightarrow$ 5.619 MeV)

the 4.4 MeV–gamma ray emission is significantly Doppler broadened resulting from the kinematics of the nuclear reaction.

Energy calibrations for the HPGe and LaBr detectors were performed using a variety of sources including ^{60}Co, PuBe, as well as the 0.511, 4.439, and 15.11–MeV lines from the primary nuclear reaction, ^{11}B(d,nγ)^{12}C. This alone is not sufficient to get a good understanding of the calibration between the well separated 4.4 and 15.1–MeV lines. To fill in the gap with additional calibration points, prompt activation gamma rays were used stemming from neutron capture in ^{56}Fe, spawning 7.631 and 7.645–MeV, and ^{14}N, yielding 10.829–

MeV gamma rays. These gamma rays are discrete, not Doppler broadened, because of the kinematics as they result from thermal neutron capture in the parent nucleus. Further, the physics of pair production can be employed to expand the number of points available by including the single escape peaks of the 4.439, 7.631, 7.645, 10.829, and 15.11–MeV events in the energy bin versus energy relationship.

The prompt gamma activation lines were chosen due to the energy range and ease of generating them in the lab. A 4.4 mCi ^{252}Cf source was placed inside a high density polyethylene cylinder as a source of thermal neutrons. This was placed next to a steel dewar of liquid nitrogen and shielding, lead and borated poly, was added between the source and detectors as shown in Figure 3.7.

Figure 3.7: Photograph of prompt gamma activation experiment to gather energy calibration points. The neutron source is placed inside the while poly cylinder for thermalization and some lead is employed in the direction of the detectors to reduce the flux of 2.2–MeV gamma rays from hydrogen capture.

After an overnight count, the liquid nitrogen was evacuated from the steel dewar, and the experiment was repeated. Subtracting the spectrum of the full dewar from the spectrum of the empty dewar, we are left with only the events originating from the nitrogen. The

same process is used for an iron block to gather the iron lines. The full energy and single escape from the iron and nitrogen capture can been seen in Figure 3.8.

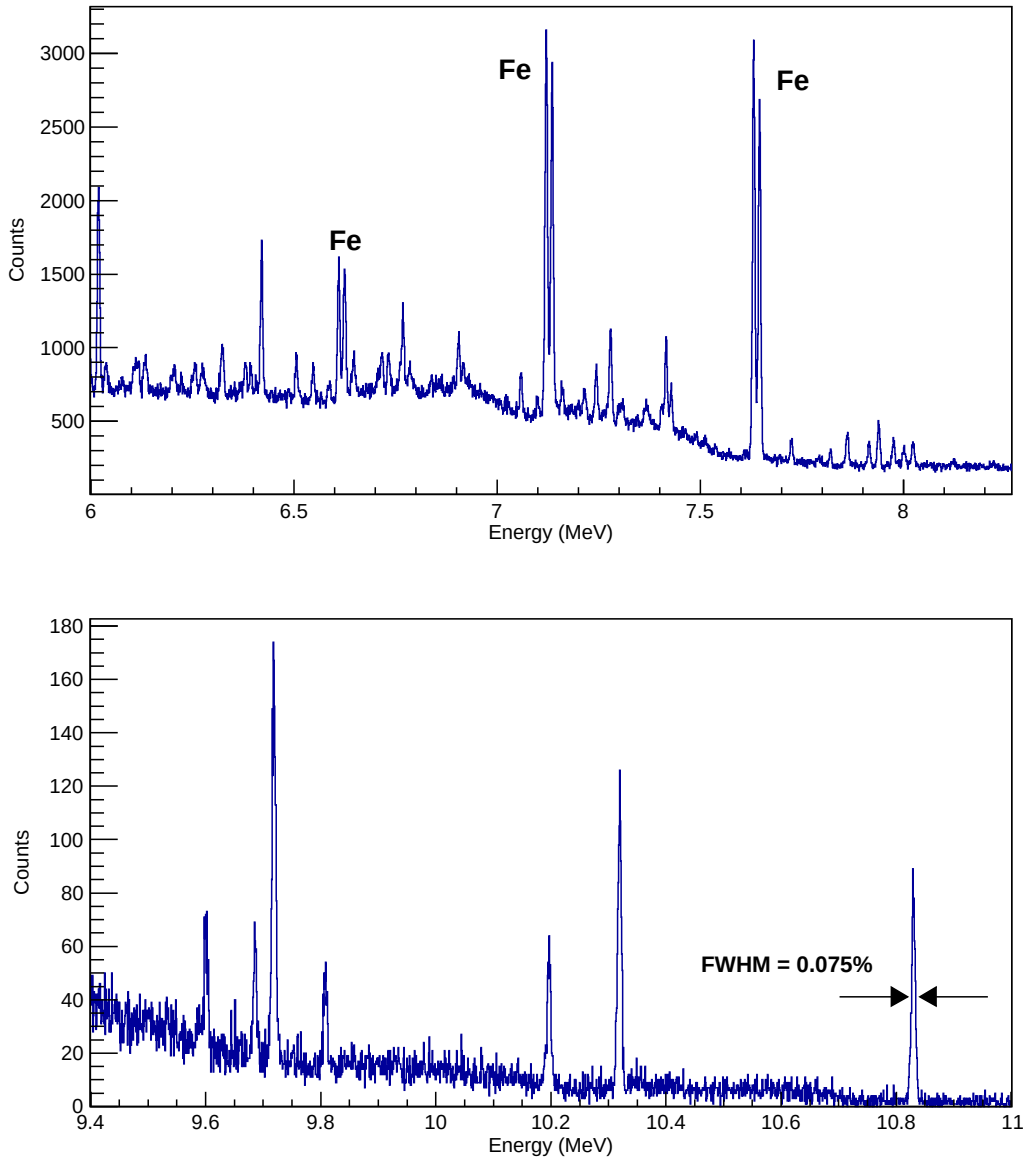

Figure 3.8: Gamma ray events collected by the 80% HPGe detector from prompt gamma neutron activation where: (top) depicts the intense 7.631 and 7.645–MeV gamma rays from iron as well as the single and double escape peaks. The events are well resolved given the 14 keV separation. (bottom) shows the prompt 10.829–MeV gamma ray lines from thermal neutron capture in nitrogen. The energy resolution of the highest energy gamma ray is calculated to be 0.075% depicting the discrete, non Doppler broadened, nature of these peaks.

This process is discussed in detail here because these mid-energy gamma ray energies are crucial for accurate calibration of the spectra collected from the beam down to keV level accuracy. Without such confidence in the energy calibration, it would be impossible to determine the unknown energies in the beam spectrum to determine if they are the result of reactions in the target or surroundings.

A Gaussian fit was applied to each well resolved, non-broadened, peak using ROOT to obtain the peak centroid and associated error which was then compiled in to a channel versus energy relationship as seen in Figure 3.9. To check the fidelity of the calibration, multiple fitting functions were tested by calculating a predicted energy and comparing it to the known energies.

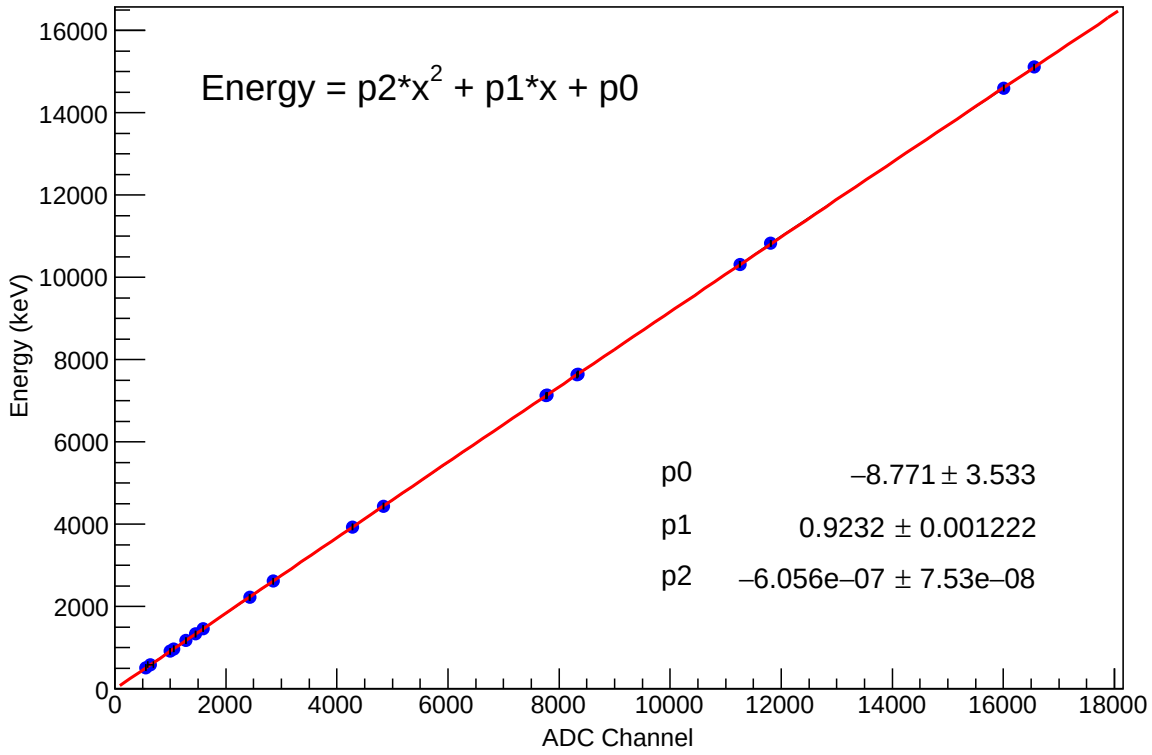

Figure 3.9: HPGe energy versus ADCCH calibration with polonomial fitting function and errors as calculated by ROOT. The blue points on the plot mark the measured peak centroid and tabulated gamma ray energy. The error on the measured centroids is included, but is smaller than the markers used to portray the points.

Semiconductor detectors such as HPGes generally display strong linearity for lower

energy ranges, but here a polynomial relationship more accurately reproduces known energies throughout the entire range of this application. The error on the determination of the channel is smaller than the marker used to depict the point, it is assumed there is no error in the associated known energies. This same method was applied to the scintillator–based detectors; however, peak drifts due to temperature changes over multiple days destroyed the fidelity of the data. After the peak energies of the beam spectrum were well known using the precision from the HPGe measurements, the same peaks were identified and mapped in the LaBr spectrum to the HPGe calibration.

The mobile 80% HPGe was placed at the detector location denoted in Figure 3.5 and lifted to the beam center line height and vertically aligned with a rotating laser that covers the entire room, including the side of the accelerator. The horizontal alignment was done using a plumb bob from the center of the detector down to professionally surveyed markings on the floor of the facility. This was then checked by installing a flood light at position 1 in Figure 3.5 and turning the overhead lights off. The flood light shines through multiple layers of collimation to ensure proper alignment before the light was removed. The neutron filter was stacked to include 50.8 mm of 5% borated poly to eliminate as many neutrons as possible into the environment. A lead cave was built around the crystal of the HPGe and collimator bricks containing a 36.3–mm diameter hole were stacked in front of the detector. Figure 3.10 shows the setup as it was being constructed.

This photo is used to show the alignment and concept of the shielding and collimation around the HPGe crystal. The detector/crystal itself was not visible in the final configuration. The 36.3–mm diameter collimators were stacked to 40.6–cm thick and aligned the beam directly into the center of the 73.7–mm diameter crystal. The combination of the cave and collimator cut down on any room return and decreased the probability of single and double escape peaks resulting from pair production in the detector.

The accelerator was operated at a lower than normal current, 2.5 μA, in order to reduce pulse pile up and dead time in the detector. The total collection time was 15685 seconds

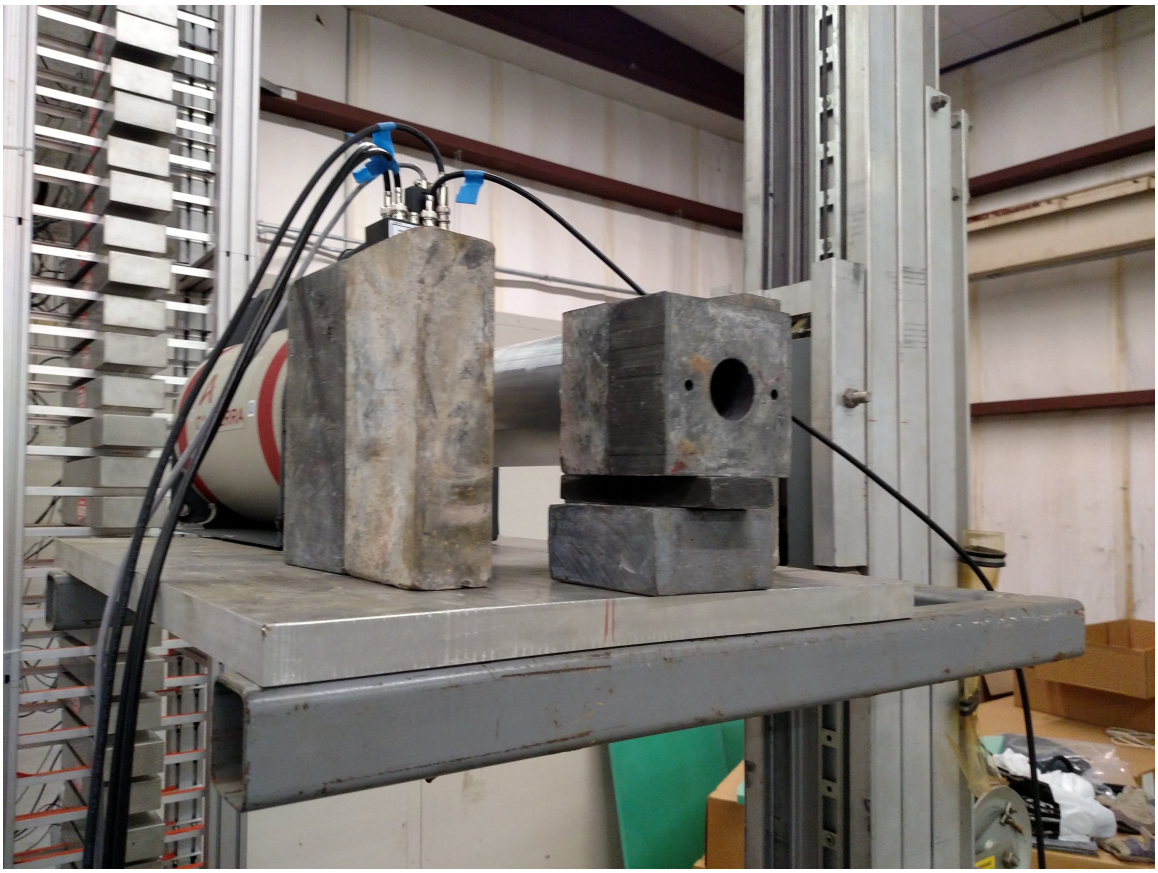

Figure 3.10: Photograph of HPGe lead collimation and shielding cave during construction. The lead collimator bricks contain a 36.3–mm diameter hole aligning the incident radiation beam into the center of the 73.7–mm diameter HPGe crystal. A total of eight of these collimator bricks were aligned in the final configuration.

and the average deadtime was 2.97%. Background was collected for the same amount of time, 15685 seconds, the night after the experiment when the accelerator was off, yielding a deadtime of 1.63%. The overnight background was nearly negligible due to the lead cave so it was directly subtracted off the beam spectrum which was then energy calibrated to produce the spectrum shown in Figure 3.11.

This spectrum is broken down in to multiple segments to present a more detailed view of the higher energies. There are three large gamma rays below 2 MeV that appear to be orders of magnitude more prominent than the higher energies. This spectrum may be slightly misleading because it has not been corrected for the energy dependent intrinsic efficiency

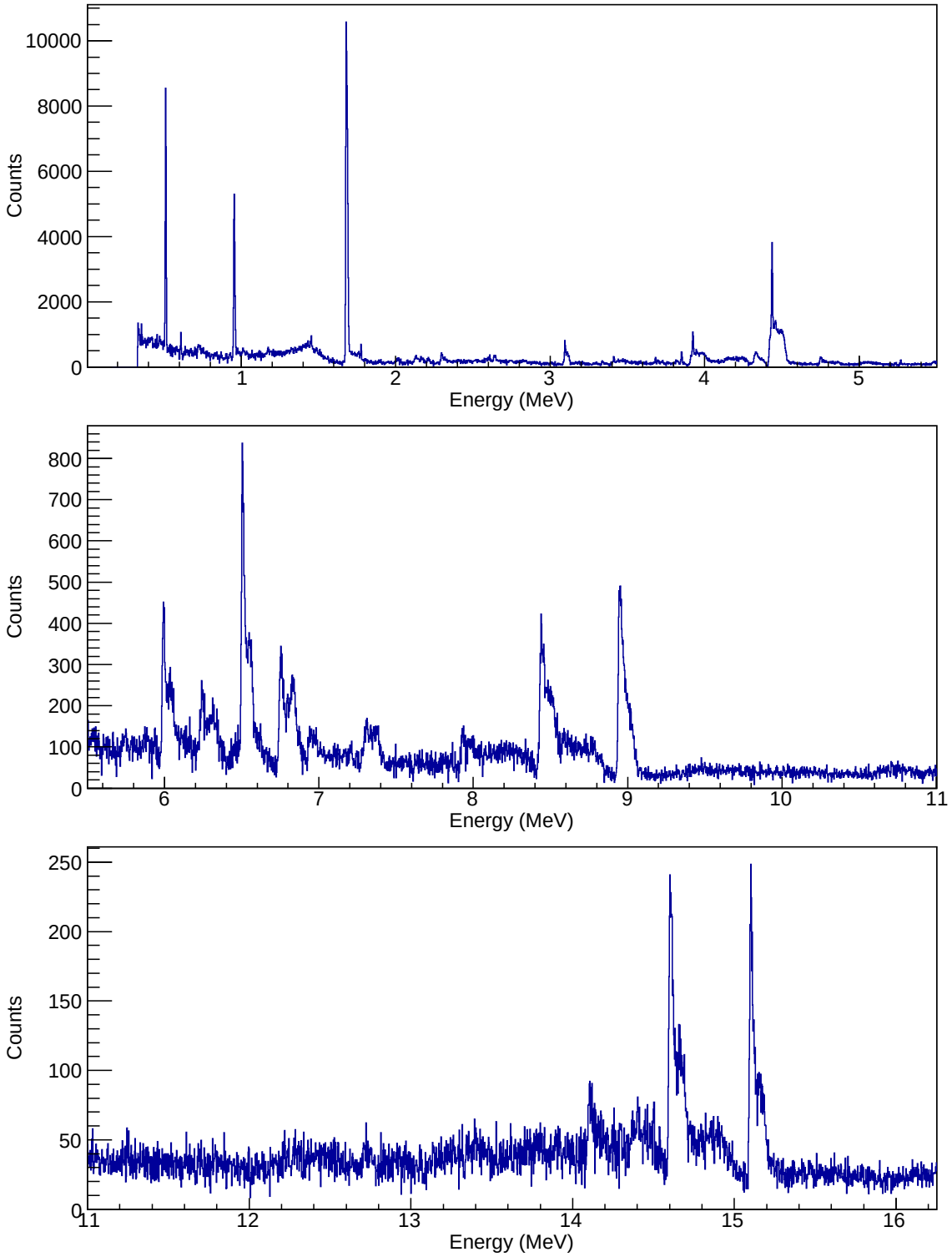

Figure 3.11: High resolution, energy calibrated spectrum of the ^{nat}B(d,nγ)^{12}C source using a HPGe detector shown for the first time.

nor the event losses due to the transistor reset preamplifier. Instead, this is presented to identify peak energies and compare to known nuclear states to determine the origin. A LaBr spectrum, found in Figure 3.12, will be more useful to visually compare the relative intensities of the peaks as the crystal has a higher density than HPGe and it does not have the preamplifier issue.

This plot has been restricted to 2 MeV and higher to show the resolved peaks between 4.4 and 15.1 MeV and relative magnitudes. In the LaBr detector, more single and double escape peaks are visible because the size of the crystal is considerably smaller than the HPGe and the collimator bricks were not employed. The full energy deposition of the 15.1–MeV gamma ray is visible, yet very small. The double escape peak is the most prominent for the incident 15.1–MeV photons. A large portion of the counts collected between 10 and 14 MeV in the LaBr spectrum are due to bremsstrahlung radiation emission from the high energy electrons propagating through the crystal which escapes.

3.5 Identifying Intense Peaks and Their Origins

Identifying the origin of the observed peaks has not been done before because it is an arduous task. There are many reactions taking place here that emit gamma rays, but the focus will be on the largest ones in order to determine if this source is a viable option for active interrogation. Many techniques were used to identify the possible and most likely origins, but some peaks may be the result of a combination. More detail will be given about the determination as each peak as it is discussed.

The main observable reaction is the desired ^{11}B(d,nγ)^{12}C resulting in the most prominent gamma ray yields of 4.438 MeV ($2^+ \rightarrow 0^+$) and 15.1 MeV ($1^+ \rightarrow 0^+$). Some of the observed gamma rays stem from secondary and tertiary reactions taking place from reactions such as ^{11}B(d,n)3α where the alpha particles go on to create other nuclear reactions. A summary of the most likely origin of other observed energies identified can be seen in Table 3.6.

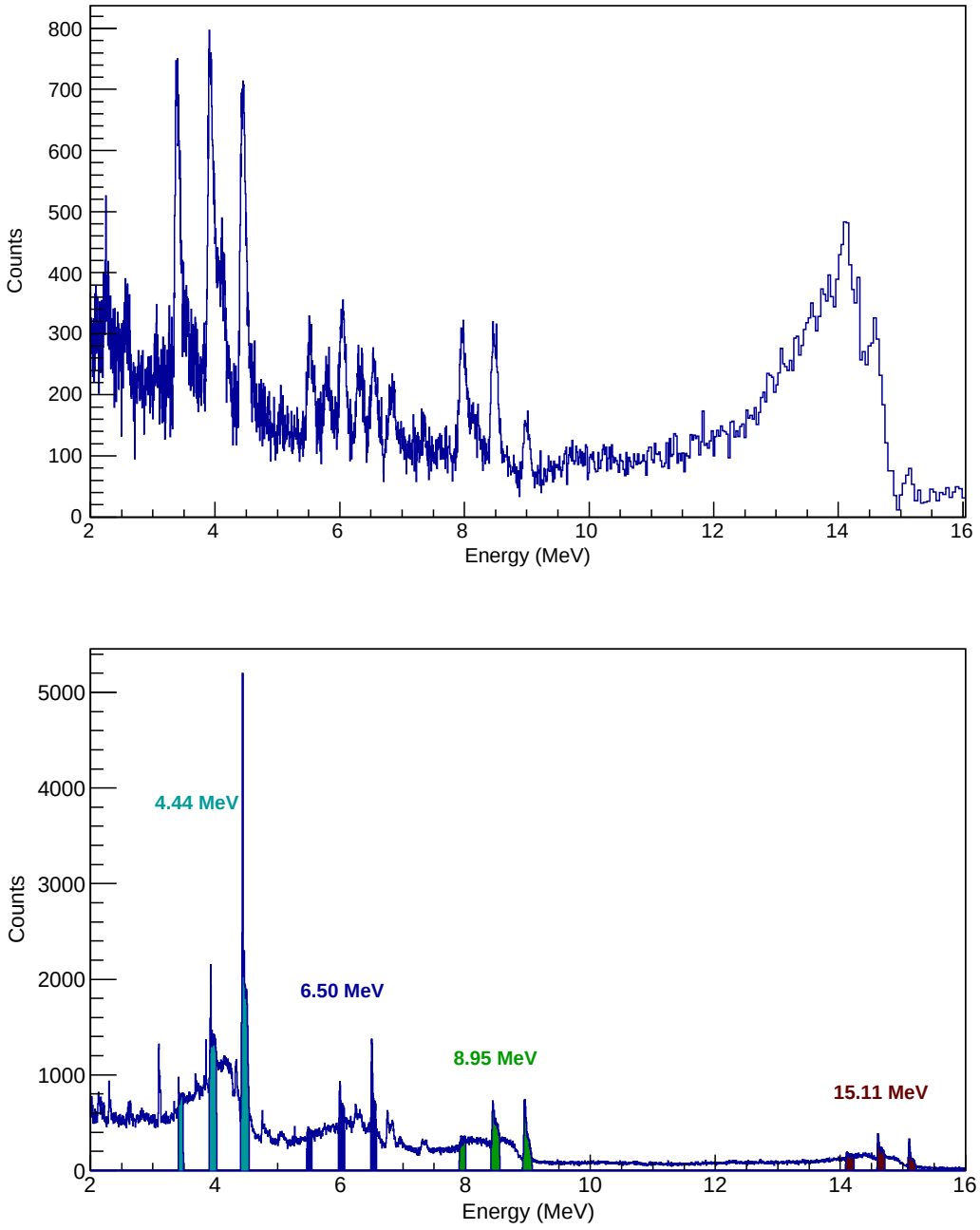

Figure 3.12: Energy calibrated spectra of the ^{nat}B(d,nγ)^{12}C source using a LaBr detector (top) compared to the 80% HPGe detector (bottom) showing only the regions corresponding to gamma rays greater than 2 MeV.

This is not an exhaustive list of all gamma lines detected, but is a list of the most prominent observed gamma de-excitations taking place. Some of the features in the spectrum are

Table 3.6: A summary of the most intense peaks observed. Identified by the energy calibrated peak centroid and propagated uncertainty. The reactions and transitions are only some of the possible reactions emitting gamma rays within the uncertainty range. A full list can be found in Appendix B.

gamma energy	energy error	reaction	transition
511.4 keV	$\pm$ 1.29 keV	β^+ annihilation	
954.3 keV	$\pm$ 2.43 keV	^{11}B(n,γ)^{12}B	$2^+ \rightarrow 1^+$
		^{11}B(d,p)^{12}B*	$2^+ \rightarrow 1^+$
1684.14 keV	$\pm$ 1.21 keV	^{11}B(d,α)^{9}Be*	$\frac{1}{2}^+ \rightarrow \frac{3}{2}^-$
4437.87 keV	$\pm$ 2.27 keV	^{11}B(d,n)^{12}C*	$2^+ \rightarrow 0^+$
		^{27}Al(p,p')^{27}Al*	$\frac{9}{2}^+ \rightarrow \frac{3}{2}^+$
4458.08 keV	$\pm$ 3.02 keV	^{27}Al(n,γ)^{28}Al	$4^+ \rightarrow 3^+$
6505.46 kev	$\pm$ 3.48 keV	^{27}Al(α,p)^{30}Si*	$5^+ \rightarrow 4^+$
		^{27}Al(α,n)^{30}P*	$1^- \rightarrow 0^+$
		^{208}Pb(n,n')^{208}Pb*	$1^+ \rightarrow 0^+$
		^{12}C(α,n)^{15}O*	$\frac{5}{2}^+ \rightarrow \frac{5}{2}^+$
6756.70 keV	$\pm$ 3.91 keV	^{11}B(d,α)^{9}Be*	$\frac{9}{2}^+ \rightarrow \frac{3}{2}^-$
8951.76 kev	$\pm$ 2.18 keV	^{27}Al(p,p')^{27}Al*	$\frac{3}{2}^+ \rightarrow \frac{3}{2}^+$
		^{27}Al(n,n'α)^{23}Na*	$\frac{7}{2}^- \rightarrow \frac{5}{2}^+$
		^{27}Al(α,p)^{30}Si*	$2^+ \rightarrow 0^+$
15101.90 keV	$\pm$ 6.80 keV	^{11}B(d,n)^{12}C*	$1^+ \rightarrow 0^+$
		^{10}B(d,α)^{8}Be*	$1^+ \rightarrow 2^+$

omitted because they are poorly resolved. Upon analysis, they appear to be a combination of double and single escape peaks in addition to a Doppler broadened full energy peak within a few keV of each other yielding one large feature. The uncertainty of this finding was too large to be considered definitive and other experiments should be conducted attempting to resolve this.

The presented reactions were chosen by using the HPGe data and energy calibration to determine the energy of the peaks, then comparing to known states tabulated by the National Nuclear Data Center (NNDC) managed by Brookhaven National Lab [47]. The energy available in the system and kinematics of these reactions were checked to make sure they are possible, which eliminated some from the initial list. These peaks may be from a combination of some or all of the possibilities listed; however, it is important to consider

the possibility that these could result from a currently unknown state.

One issue to consider when using HPGe detectors in an environment that may contain neutrons is n,γ reactions with the germanium of the detector leading to excess signal [48]. This was mitigated by the use of the 50.8–cm thick neutron filter placed in front of the source. However, the borated poly of the filter may be partially responsible for one of the observed peaks, 954.3 keV, through a ^{11}B(n,γ)^{12}B and ^{11}B(d,pγ)^{12}B reaction. This is deemed partially responsible because the same reaction is occurring in a much greater abundance inside the boron target as well. Other potential gamma rays originating in the filter were ruled out by using the LaBr detector and varying the thickness of the borated poly from 0 to 53.34 cm in 17.78 cm increments, a graphical comparison can be seen in Figure 3.13.

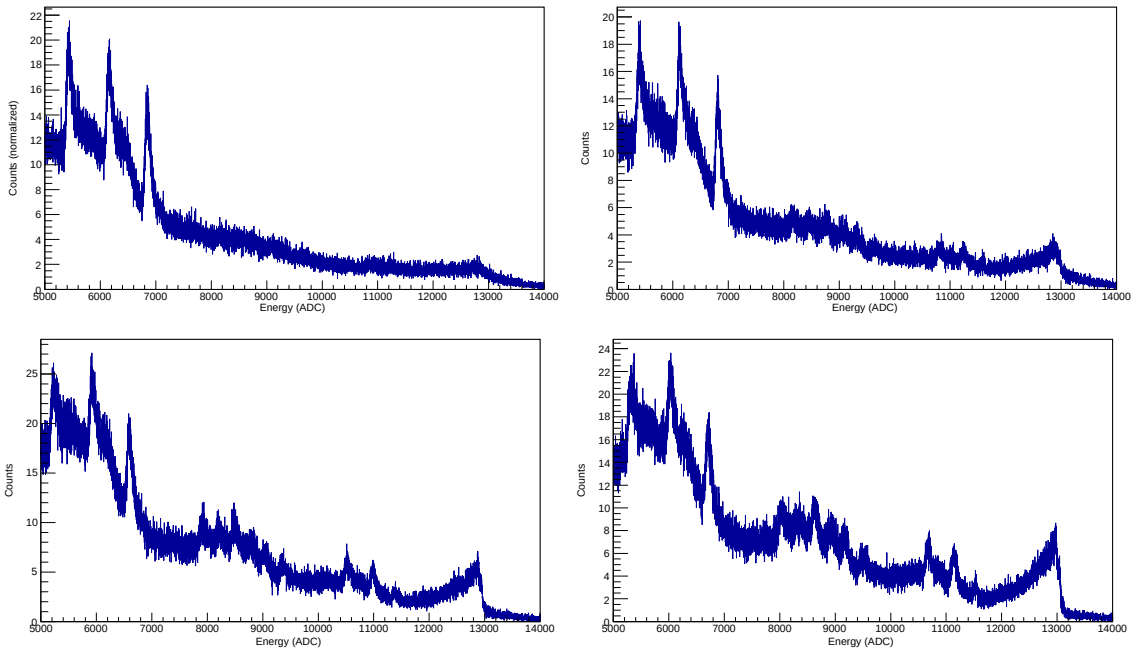

Figure 3.13: Spectra of the ^{nat}B(d,nγ)^{12}C source using a LaBr detector with varying thicknesses of borated poly used as a neutron filter starting from zero in the top left plot ranging up to 21 sheets in the bottom right plot. The region of interest, channels 7000 through 12000, change in resolution but not in magnitude with increasing thickness of neutron filter.

The main area of interest is between 4.4 and 15.1 MeV, channels 7000 through 12000.

As more borated poly is added the peaks become visible, however the contribution of these gamma rays to the spectrum can still be seen even with no borated poly suggesting the origin of the peaks is not in the filter. The peaks become more resolved with added sheets of borated poly because the reduction of pulse pile up from the lower energy, less than 2 MeV, gamma rays. The current of the accelerator and location of the detector was held constant so the only variation was the thickness of the filter. When no borated poly is used the signal is dominated by ever present 511 keV from activation and subsequent β^+ decay inside the target area. The borated poly is not only a neutron filter, but also acts as a low energy gamma ray filter.

Most of the intense gamma rays observed stem from the deuteron-boron reaction and are the result of excited states of beryllium, boron, or carbon. One such peak is found to be 1684 keV resulting from the ^{11}B(d,α)^{9}Be reaction which was predicted to occur in 8.94% of the deuteron interactions by the Geant4 simulations. The intensity of this peak is overstated on the graphical representation, Figure 3.11, due to the lack of correction for detector efficiency in this plot in order to preserve integrity of the data.

Continuing in increasing energy in the spectrum, the next major gamma ray observed is the coveted 4.4389–MeV emission from the ^{11}B(d,nγ)^{12}C reaction. It is important to note that there may be other contributions to this peak such as the 4.438–MeV from ^{27}Al(p,p')^{27}Al* or the 4.444–MeV from ^{9}Be(d,γ)^{11}B as well as others. These reactions are not immediately intuitive and part of the reason this level of detail has never been presented before so they will be discussed in more detail before continuing with other peak identifications.

An abundance of high-energy particles available in the deutron – boron target system alone has already been established in Figure 3.6. It is assumed none of the charged particles will escape the boron target itself since the size of the target is far greater than the range of these particles. Here we need to consider two main issues, high energy neutron interactions occurring anywhere in the system and the transmutation of isotopes inside the target itself.

The experimental setup and shielding configuration is sufficient to stop neutrons from entering the room environment in significant quantities; however, the boron target is mounted directly to an ^{27}Al holder. The neutron production from the ^{11}B(d,nγ)^{12}C reaction has been estimated, on the order of 10^9 μA^{-1}s^{-1}, to be two orders of magnitude larger than that of the gamma rays and extends up to 16.5 MeV [6, 7]. Examining the published ENDF/B-VII.1 cross sections [49] of neutron interactions in ^{27}Al and the boron isotopes found in Figure 3.14, it is obvious there will be a high probability of interactions considering the neutron flux and energy along with the relatively large amount of material. This is backed up by the Geant4 simulation results presented in Table 3.4.

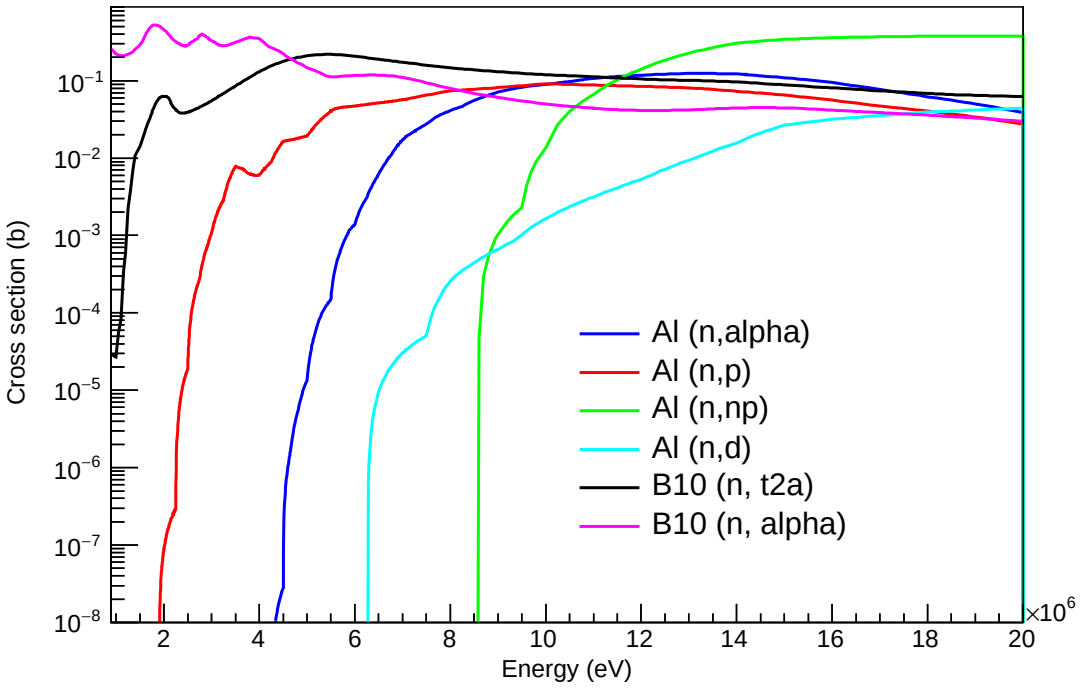

Figure 3.14: Select neutron cross sections in aluminum and boron materials plotted using ENDF/B-VII.1 cross sections downloaded from KAERI [49]. The source is known to produce copious amounts of neutrons extending up to 16.5 MeV which can result in many reactions producing charged particles that cascade into other reactions.

Of particular interest at this point of the discussion are reactions in aluminum resulting in either protons or α particles. The cross sections for these reactions are about 0.1 b

once the neutron energy reaches more than a couple MeV, the resulting charged particles quickly interact in the surrounding aluminum causing more reactions. This does not seem like a large probability until it is considered in perspective to the estimated neutron flux, 10^9 per μA of beam current, into the 1.5 cm thick aluminum target that covers essentially 2π of the solid angle of emitted neutrons. The same argument can be made for interaction inside the boron target itself yielding some credibility to the Geant4 predicted interactions in Figure 3.6. There is a strong possibility these reactions make a significant contribution to the observed gamma ray spectrum downstream of the target holder.

The second main issue that must be considered at this stage is the in-growth of other isotopes into the natural boron target. The measured deuteron beam current, I, can be converted to estimate the number of deuterons per second incident on the boron target via Eq. 3.3 by simply dividing the frequently used beam current, 24 μA, by the elementary charge.

$$I/e = \frac{24 * 10^{-6} Coulomb/second}{1.602189 * 10^{-19} Coulomb} = 1.498 * 10^{14} \frac{deuterons}{second} \tag{3.3}$$

The spot size of the deuteron beam impinging on the boron target is stated to be 10 mm in diameter by the manufacture [44]. The deuteron range is on the order of microns in the target yielding a relatively small number of target atoms given the target has been used consistently for approximately 2 years at beam currents up to 24 μA. This could lead to a staggering number of reaction products considering the simulation in Table 3.3 was for only 10^9 incident deuterons, five orders of magnitude lower than the actual beam currents, representing only 10's of microseonds of actual beam current. Most notable will be the build up of ^{9}Be and ^{12}C from the predominant deuteron interactions. This build up further complicates the list of possible reactions considering deuterons may be impinging upon the built up isotopes and these reactions are known to emit large amounts of alpha particles, all in this relatively small area.

One such interaction of concern is the build up of ^{9}Be interacting with the impinging

deuterons producing a ^{9}Be(d,γ)^{11}B reaction with a mass only Q of 14.79 MeV. This one potential addition mentioned earlier to the 4.4 MeV observed peak. This is a somewhat cyclical reaction as some of the ^{11}B will eventually interact with a deuteron and may go back to ^{9}Be via reactions specified earlier, referred to here as the BeB cycle for now. Many of the reactions mentioned in this analysis are part of a larger reaction cycle of great interest to the Astrophysics community — the CNO cycle — involving carbon, nitrogen, and oxygen in the early universe.

Having established these other processes are taking place in the experimental system, lets return to the main goal of this study, identifying the observed gamma ray peaks. The next major gamma rays observed in Figure 3.11 from the accelerator are calculated to be 4.458, 6.505, and 8.951–MeV along with their associated single and double escape peaks. These are difficult to track down as there are a plethora of isotopes that can emit gamma rays in this region depending on the excitation energy and method, see Appendix B for a complete list. One similarity between all three of these gamma rays is that they are all possible from ^{27}Al reactions as denoted in Table 3.6. The feasibility of the listed reactions involving aluminum has been presented in the previous discussion.

The 6.505 MeV peak may be a compilation of contributions from other reactions such as ^{208}Pb(n,n')^{208}Pb*. The established neutron flux in conjunction with the amount of lead surrounding the target, see Figure 3.3, mean a contribution to this peak cannot be ruled out. The ENDF cross section for just the n,γ reaction in ^{208}Pb is approximately 2 mb for a 10–MeV neutron.

Another possible contribution to the 6.505–MeV peak could stem from the CNO cycle via ^{11}B(d,nγ)^{12}C building up ^{12}C which then interacts with any of the α particles generated to produce a ^{12}C(α,n)^{15}O* reaction. This is not expected to be a major contributor to the observed peak because it is a threshold reaction where the kinetic energy of the α, E_α, must be larger than 11.345 MeV [50]. However, it cannot be ruled out because a non-negligible quantity of α particles in the 10.5-16.5 MeV range are predicted in the target area as shown

in Figure 3.6.

In between the 6.505 and 8.951–MeV lines there is a jumble of detected signal. Part of this stems from a 6.758–MeV gamma ray emitted from the ^{11}B(d,α)^{9}Be reaction that was also responsible for the 1.684–MeV gamma ray. However, this one is not as significant because the observed peak is actually a combination of the full energy deposition in conjunction with what appears to be single escape peaks resulting from an unresolved reaction. The yield of these reactions is low and not useful for active interrogation so it is not discussed in detail.

There is a prominent peak determined to be 8.951 MeV that could be the result of multiple reactions. One of which is a p,p' with ^{27}Al as Table 3.5 predicts that roughly 20% of the incident neutrons go on to create a reaction that spawns a proton. Other possible candidates are reactions listed in Table 3.6 that are also predicted by the simulation.

The last major gamma ray to speak of is the 15.11–MeV resulting from ^{11}B(d,nγ)^{12}C. This is one of the most important emissions for the active interrogation work in subsequent sections of this thesis because it is abundant and highly penetrating through materials expected in cargo containers. It is hard to rule out reactions resulting in excited states of ^{13}C, one of which being a 15.098 MeV gamma ray through a strong M1+E2 transition. From a usability standpoint, it doesn't matter if there is a contribution since the two relatively high energy gamma rays are only a few keV different. There is an outside possibility the incident deuteron could induce a reaction in the ^{10}B that produces the Hoyle state of carbon, then decays to ^{8}Be and produces a 15.1 MeV gamma ray. This is beyond the scope of this thesis and will be further investigated as future work.

The deuteron – ^{11}B reaction results in preferentially populating the 15.1–MeV state instead of the 12.7–MeV state of ^{12}C. Theoretically the incident deuteron will occasionally slow down to below the 15.1–MeV state threshold in which case there should be a strong 12.703–MeV gamma ray. There is no observed 12.703–MeV gamma ray in the LaBr spectrum, but it could be buried in the bremsstrahlung portion of the 15.1–MeV sig-

nal. Inspecting the HPGe spectrum, there does appear to be an artifact in approximately the right location to suggest a 12.703–MeV gamma ray; however, it is not enough to confirm the presence of one suggesting the deuteron interacts through a nuclear reaction before slowing down to the threshold energy.

Throughout the studies conducted as part of this thesis there has always been an intense 511 keV emission from the target. Routine safety surveys upon entry to the accelerator area require the use of an ion chamber to ensure the accelerator is off. These surveys lead to another important observation, the target was still radiating fairly intense radiation for a period of time after shutting down the beam. Studies of this radiation lead to findings of activation products such as the 1.79–MeV from aluminum and a highly intense 511 keV emission.

The 0.511–MeV gamma ray comes from annihilation meaning the parent decay product must be a positron (β^+) emitter thus the parent isotope has an excess of protons. This is usually a very unstable configuration leading to short half-lives, on the order of a few seconds or less; however, this emission lasts for more than an hour. This was investigated by employing a LaBr detector in the beam line using the list mode capabilities of the DT5730 digitizer where each event is saved with a time stamp. The beam was run at 20 μA for 30 minutes to build up the decay products. Data acquisition started a few seconds before the beam was shut off and continued for a total of 1800 seconds. The 0.511–MeV events were isolated and plotted as events per second producing an activation die-away plot shown in Figure 3.15.

The first 200 seconds of the decay radiation are ignored since there will likely be an abundance of short lived positron emitters. The main interest here is the most intense decay products, which are also long lived. The slope of this decay curve was analyzed and fitted with a single exponential decay function, Equation 3.4, using ROOT in efforts to determine

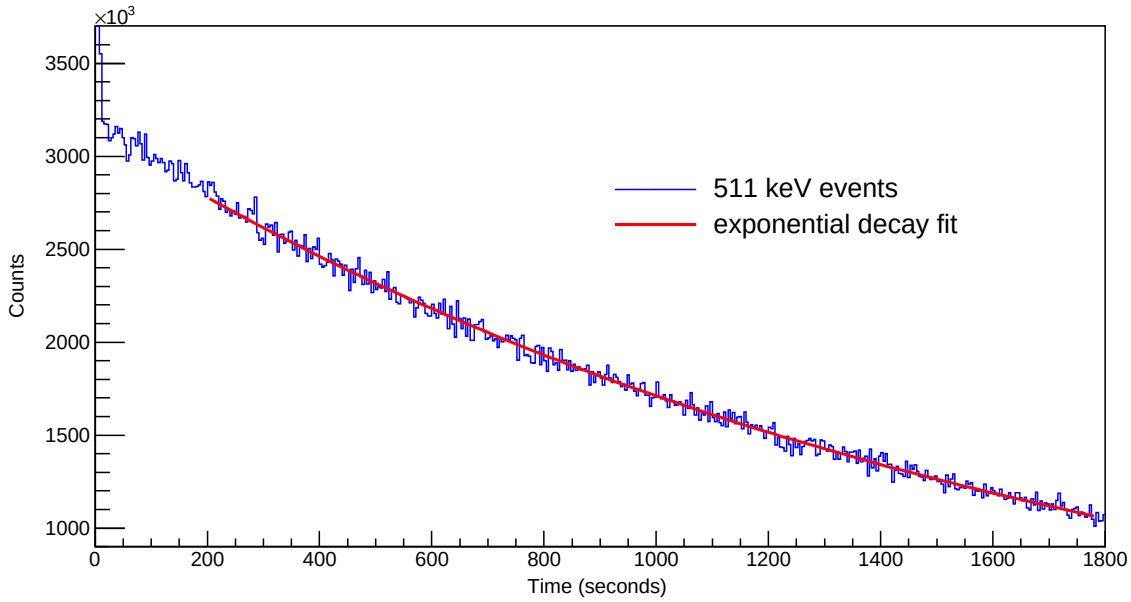

Figure 3.15: Isolated 511 keV activation product decay from the target immediately after shutting off the beam. The red line denotes a fitted relationship of Equation 3.5.

the decay constant, λ, which contains the half-life, $t_{1/2}$.

$$N = N_0 e^{-\lambda * t} \tag{3.4}$$

The single exponential decay function fitted from 200 – 1800 seconds yielded a calculated half-life of 1154.2 seconds. This does not match the half-life of any single known decay tabulated from NNDC so this must be a combination of decay products. When the same equation was fitted from 1400 – 1800 seconds the calculated half life rose to 1182.9 seconds, which still does not match any known decays but suggest a combination of one intense, long lived decay combined with others that are much shorter. Inspecting the predicted nuclei resulting from the nuclear reaction simulations in the target there is only one proton heavy isotope produced in large quantities with a half life on this order of magnitude, ^{11}C. This is a known β^+ emitter with a tabulated half-life of 1221.8 seconds [47]. This can be used in a multiple exponential function to describe i isotopes decaying as found

in Equation 3.5.

$$\Sigma_i N_i = \Sigma_i N_{0_i} e^{-\lambda_i * t} \tag{3.5}$$

Fitting this equation to two isotopes, using the ^{11}C half-life as an initial condition, the unknown half-life is calculated to be 148.93 seconds. This closely matches the half life of ^{30}P which is a predicted product of the aluminum – neutron simulation reported in Table 3.5. This simulation also predicts a build up of ^{30}S, another β^+ emitter, which has a short half-life of 1.178 seconds and decays into the longer lived ^{30}P. This is an important finding lending validity to the simplified simulation but also because both ^{30}P and ^{30}S have multiple gamma emission possible in the 6.5 MeV range as shown in Appendix B that could also be adding to the observed spectrum.

The ^{11}C build up and decay presents another interesting relationship as it is generated from deuteron on ^{10}B reactions. It decays to form ^{11}B which then undergoes any of the listed reactions that may produce the desired gamma rays previously described. This is akin to a breed-and-burn cycle used in nuclear reactors with uranium and plutonium isotopes.

Applications for the 0.511–MeV gamma ray are yet to be decided. They may be of some use in imaging assuming enough make it though the interrogated material for analysis, but they may also contribute too much to the dose delivered to the cargo. Dose studies are beyond the scope of this thesis but are under investigation by other researchers. If the studies conclude this gamma ray imparts too much dose to make it viable in a production system, the target could simply be changed back to an enriched ^{11}B target and include active cooling to avoid destroying the target. The activation study shows nearly all of the 0.511–MeV gamma rays from long term decay originate from ^{11}C, which simulations suggest is only a product from ^{10}B based deuteron reactions. Some level of 0.511–MeV will still be present from the short lived β^+ emitters and pair production events, but it would be less. The massive amount of 0.511–MeV gamma rays observed during beam operation will still be present from all the other reactions taking place. Essentially all of the intense peaks

observed originate from either ^{11}B or ^{27}Al based reactions as tabulated in Table 3.6.

3.6 Other Potential Reaction for Use

The focus thus far has been on a single reaction as a possible candidate for a low energy nuclear reaction based active interrogation source. There are many other reactions that need to be explored for potential use as well. Such reactions could be studied with a compact cyclotron accelerating protons to varying energies before impinging on a variety of targets. This would provide a way to experimentally measure the yield of gamma rays as a function of energy to optimize for active interrogation purposes.

One reaction of interest is ^{12}C(p,p')^{12}C which can reach the same 4.4 and 15.1 MeV states as discussed in the previous section. Protons in the 16-20 MeV range could populate the desired states but would result in relatively small neutron production. This could be a desired alternative to reduce dose to the cargo containers if only the gamma rays are used for interrogation.

3.7 Conclusion and Future Work

There is a wide variety off sources available for use in active interrogation. Proper selection of the source depends on the goal of the system; imaging, material identification, fission, etc. All systems designed for practical use must keep certain key parameters in mind that effect the source selection such as penetrability of the radiation, dose to cargo as stowaways, speed of scan, and footprint of operation.

The investigation presented here has explored the use of low energy nuclear reaction sources, particularly the ^{nat}B(d,nγ)^{12}C using a 3.02 MeV deutron using a compact linear accelerator. This system was found to be useful as an active interrogation source given the highly penetrating discrete energy gamma rays and their separation. Understanding the output of the reaction is crucial in order to apply the source properly. Here we have seen a copious amount of nuclear reactions taking place with respect to the one desired

reaction. Knowing the energies and reactions generating them can lead to better target development and experimental setups. For example, a moving boron target would not suffer from significant build up of reaction products which could eliminate some of the undesired signal. Another improvement could be to avoid using aluminum as a target holder or end cap if the 6.50 and 8.95–MeV gamma rays are not desired. Ideally the boron target would be attached directly to the end of the accelerator itself without a holder which would eliminate all the aluminum reaction discussed. This would require some advancements in the target construction as pure boron is usually very brittle and would not stand up to the pressure differential of the vacuum system and environment.

Fully understanding the production of these gamma rays could also lead to more efficient use of this source in active interrogation by utilizing each major peak in transmission analysis. This will be presented further in the next chapter which addresses the imaging system and principles of operation in the proof-of-concept Cherenkov array.

Further experiments with this reaction could be useful to validate the Geant4 model and fill in the nuclear data currently missing in order to simulate the population of the 15.1 MeV state of ^{12}C. In addition to this reaction, other reactions discussed should be experimentally explored for potential use in active interrogation applications.

CHAPTER 4

IMAGING TECHNIQUES FOR ACTIVE INTERROGATION

The application of radiography to an object is a standard practice today in many fields ranging from the food packing industry to nuclear security. The beverage industry often applies x-ray radiation to cans at the end of the filling process to ensure they are filled to the proper level before packing. The welds of steel pipelines used by the oil and gas industry can also be exposed to radiation in the search for imperfections in the weld that would potentially lead to failure of the pipeline under pressure. The most prominent application of radiation based imaging is in the medical field where many techniques are routinely used and is the focus of much the research devoted to radiation based imaging today. This research often finds its way into applications in other industries, but sometimes the advancements go both ways.

Radiation based imaging systems in nuclear security are not a new concept and have adopted much of the technology developed for medical applications. However, imaging an object such as the contents of a cargo container is vastly different than imaging a tumor or broken bone. Active interrogation systems searching for shielded special nuclear material need special attention when it comes to technological advancements because they essentially operate in a different physics realm. Medical applications require extremely precise spatial resolution to focus on minute details in low density materials, the human body, which generally involves the use of low energy radiation. Cargo containers often contain large amounts of higher density material that require penetrating radiation, high energy neutron or photons, for interrogation.

4.1 Overview of Select Current Methods

Many systems for active interrogation have been proposed using varying technologies and operating principles. The composition of such a system depends on the end goal such as imaging, induced fission, elemental identification, and others. Imaging alone is comprised of many types of systems as the term imaging is broadly defined. Some systems use x-ray back scatter to build an image of the cargo contents closest to the wall facing the radiation beam [51]. This is done by applying radiation on one side of the container and using detector arrays above, below, or on the same side to monitor for scattered photons at certain angles [52]. The ability of these systems to image the entire depth of container and potential use for elemental identification has yet to be shown with acceptable doses and scanning times.

Another imaging technique recently growing in popularity is muon tomography which relies on cosmic muons passing through a set of detectors, then scattering inside the cargo container, then passing through another set of detectors upon exiting to gather information about the track on the muon [33]. This does not really count as active interrogation because it utilizes cosmic background radiation as the interrogation source leading to some significant challenges, system complexity and scan times. These systems must be large and complex to track the limited number of muons incident upon the system leading to limited spatial resolution, elemental discrimination, and poor statistics without counting times on the order of weeks [53]. Neutron interrogation systems can be relatively simplistic by simply bombarding an object with fast neutrons and using large detectors to monitor for beta delayed radiation resulting from fission, thus confirming the presence of SNM [54]. However, this does not produce images of the contents and the beta delayed radiation is low energy making it easily shielded and thus missed by the system.

Transmission imaging currently provides the most promising ability to interrogate all the way through the cargo container while producing an image [4]. This method relies

on bombarding one side of the cargo container with high energy photons and measure the resulting photons exiting the container on the other side producing a high contrast, two-dimensional, side view image of the container. Application of this technique thus far has focused mainly on bremsstrahlung sources as the means of interrogation. However, the dose delivered to the cargo with the broad energy beam and elemental identification has yet to be addressed. The work in this thesis seeks to mitigate some of these drawbacks by using a transmission imaging technique with a low energy nuclear reaction source and a set of custom designed detectors.

4.2 Energy Independent Transmission Imaging

Transmission imaging operates on the principle of attenuation in the interrogated material and was previously illustrated in Figure1.2. This is typically done by comparing the detector response of the source directly incident on the detectors with nothing in between to the detector response after the interrogation beam traverses some material. The detector response for each is integrated to produce a transmission fraction, T, found in Equation 4.1:

$$T = \frac{I_{impeded}}{I_{unimpeded}} \tag{4.1}$$

where the total number of counts for each scenario are calculated as the integral of the interrogated material, $I_{impeded}$ and the integral of the unimpeded beam, $I_{unimpeded}$, to produce a transmission ratio. The ratio represents the fraction of the beam that was attenuated by the interrogated material and should span a range of 0.0 – 1.0 where 1.0 indicates an unimpeded beam and 0.0 represents a beam that is fully blocked from the detectors. Ratios exceeding 1.0 are falsely possible if there is significant in-scatter incident on an unimpeded detector so proper design of collimation and detectors arrays is important.

The transmission ratio process is applied to each detector in an array as material is translated between the source and detectors, then assembled into a two dimensional map

of the transmitted fraction producing an image where each detector represents one pixel at some location. This is a fairly simplistic methodology that does not require any energy resolution in the detectors. Often times these types of systems use the broad energy bremsstrahlung beams and high efficiency detectors such as $CdWO_4$ in Geiger mode [23]. The output of this technique is essentially independent of energy and produces an image of the areal density of the object, similar to that of a medical x-ray but uses an entirely different energy domain and individual detectors instead of film. The use of detectors fixes the spatial resolution of the image so small faced, tightly packed detectors will produce images the best spatial resolution available.

The work in this thesis focuses on the use of custom designed Cherenkov detectors and a discrete energy photon beam from the ^{nat}B(d,nγ)^{12}C reaction previously discussed in chapters 2 and 3 respectively. The current process of interest uses a collimation configuration found in Figure 3.5 effectively creating a fan beam of discrete energy photons. Objects are placed in the area denoted as "Imaging area" and are translated in 3 mm steps across the beam. The object location is fixed for 300 seconds of irradiation before it is moved. The first ever experimental image using a low energy nuclear reaction interrogation source if found in Figure 4.1.

This fairly simple lead collimator, Figure 4.1a, was chosen to illustrate a few key results of interest; spatial resolution and in-scatter effects. The object is 5.08 cm thick and contains three holes aligned horizontally, two that are 6.6 mm in diameter and one that is 36.3 mm in diameter as shown in Figure 4.1b. The spectra of each detector was integrated to calculate the transmission ratio of each pixel according to Eqn. 4.1 to reconstruct a high contrast planar image of the object, Figure 4.1c. The eight-detector array used here was fixed in place as the object was imaged, after the first scan the image horizontal location was reset and the scissor lift holding the lead colimator was adjusted to slightly lower the colimator and the scan was repeated. The two separate images were then interwoven during post processing based on the horizontal position and detector number. The location of the image

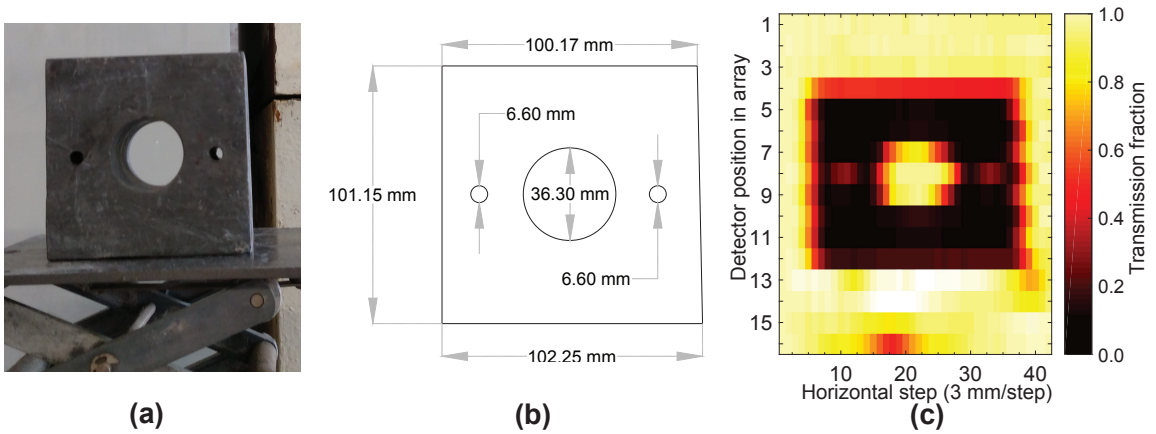

Figure 4.1: Imaging of lead collimator using a low energy nuclear reaction driven source. (a) Photograph of the lead objects chosen for spatial resolution evaluation of the array by using the three horizontally aligned holes. (b) Scale drawing of the collimator showing object dimensions, in particular the two 6.6 mm diameter holes. (c) High contract transmission image of the collimator. The x-axis represents the horizontal translation step of the imaging process (3 mm per step), while the y-axis corresponds to detector position in the array. The eight-detector array was vertically shifted and the scan was repeated to produce finer resolution resulting in a total of vertical 16 pixels. Reproduced with permission from Rose and Erickson [55]

produces a magnification of about 2 on the detectors so the vertical adjustment of the image, 1.27 cm, moved the object shadow down by half the pitch of the detectors to compensate for the dead space of the array.

The spatial resolution of this source, object, detector array combination is sufficient to detect a small change in the imaged material. The small variation is the two 6.6 mm holes in the collimator and are indicated on the transmission image in vertical position 8 on the y-axis and positions 11 and 32 on the x-axis. This is substantial spatial resolution given the realistic standoff distance between the source and the detector array. Further illustrations of the image sensitivity and resolution can be found when analyzing the image in areas related to the scissor lift such as vertical location 16, horizontal range of 14 to 22. The mildly darkened area indicates the presence of some material of less areal density than the lead which can be explained by the intersection of the four lift supports and the aluminum hinge pin connecting them visible in photograph, Figure 4.1a.

The effects of in-scatter into the detectors resulting from strong forward scattering, high energy gamma rays interacting in the lead, scissor lift, and translation rail can be seen in the image in the area between the lead collimator and the hinge pin. This area is brighter because it exhibits a ratio slightly larger than 1.0 due to the fact the detectors are exposed to the unimpeded beam that is surrounded by material as it traverses the imaged object. Though in-scatter is present, it is reduced by the dual collimation configuration and distance between the object and imaging array leaving a small solid angle the scattered photon must satisfy. This effect can be further reduced by incorporating spectroscopic analysis instead of integral analysis in attempts to filter out events that don't correspond to a specific energy.

Integral transmission techniques such as this can produce sharp images with high contrast however they still lack elemental identification capabilities. Thus far the image produced with the low energy nuclear reaction source is essentially equivalent to what can be produced via traditional bremsstrahlung sources. The discrete energy source should be able to produce an equivalent image while delivering less dose to the object given the reduction of low energy, poorly penetrating photons that are so prevalent in bremsstrallung sources. The exact calculation of image quality and dose associated with these two sources is currently under investigation and is considered beyond the scope of this thesis.

4.3 Energy Dependent Transmission Imaging

Transmission of photons through a material depends on the energy of the photon and the average atomic number of the material. The total linear photon attenuation is a sum of all contributing attenuation coefficients — photoelectric effect (σ_{pe}), coherent and non-coherent scattering(σ_c), pair and triplet production(σ_{pp}), and photonuclear(σ_{pn}) — for a given material and energy photon. One simple way to calculate the transmission probability of a photon given atomic number related properties is the Beer-Lambert Law, Eqn. 4.2, utilizing the energy-dependent mass attenuation coefficient μ/ρ and ξ, the areal density of

the object.

$$T(E,Z) = \frac{I(E,Z)}{I_0(E)} = e^{\frac{-\mu(E,Z)}{\rho}\xi} \tag{4.2}$$

Bremsstrahlung-based sources can be used for high penetrability and elemental specificity through energy-dependent transmission imaging when metal filters are used to shield the low energy photon flux and allow only certain portions of the broad energy spectrum through [56]. Dual- and multi-energy radiography using bremsstrahlung takes advantage of the dependence of the photoelectric and Compton cross section on the atomic number Z; $\sigma_{pe}/\sigma_c \sim \mathrm{Z}^{3-4}$. The implementation of photoelectric absorption mechanism is motivated by the abundant presence of low-energy photons in the bremsstrahlung spectrum. However, low-energy photons have poor penetration capability needed to probe through shielding and significantly contributes to the radiation dose.

If multiple discreet energy photons are implemented by low-energy nuclear reactions producing gamma rays, Figure 3.11, dual-energy elemental discrimination becomes possible. Utilization of selected parts of the transmission spectrum can be used to derive the effective atomic number of the material from the total linear attenuation coefficient. This method utilizes the difference in atomic-number scaling of Compton Scattering ($\sigma_c \propto Z$) and pair production ($\sigma_{pp} \propto Z^2$) as the 4.4–MeV photon interactions are dominated by Compton scattering and the 15.1–MeV photon interactions are dominated by pair production for most materials as depicted in Figure 4.2.

This general dominance illustrates only the main interaction modes and does not tell the full interaction story. The most important property is the total interaction probability. There is still a probability of other photon interaction process taking place as shown in Figure 4.3.

Distinguishing between low-, medium-, and high-Z materials expected in cargo containers is important for the success of this active interrogation system. In this figure one can see the 4.4–MeV gamma rays are less likely to interact in low Z materials such as alu-

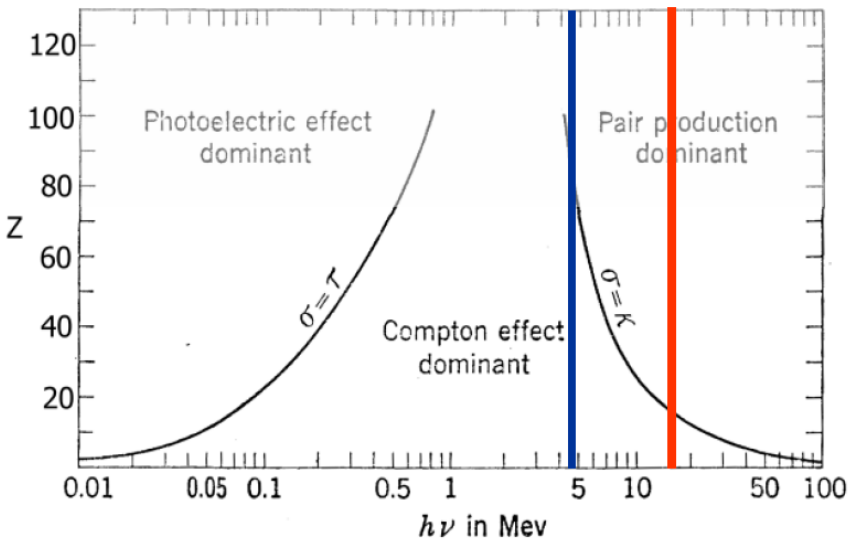

Figure 4.2: Relationship of photon interaction probability as a function of energy and atomic number adopted and modified from Knoll [57].

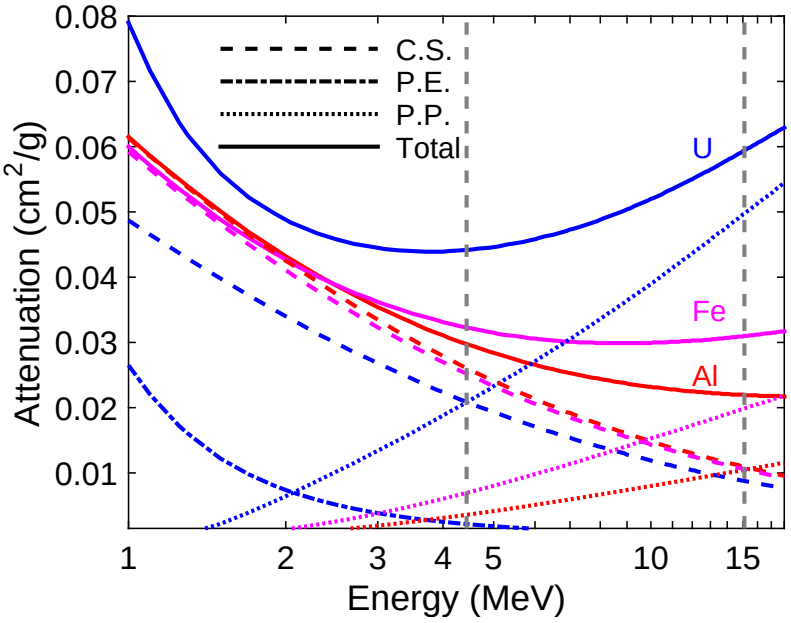

Figure 4.3: Relationship of tabulated photon interaction probabilities as a function of atomic number available from NIST XCOM [30] reproduced with permission from [7].

minum than the 15.1–MeV gamma rays. However, the opposite is true for high Z materials such as uranium.

The calculated transmission of these two gamma rays alone is not enough for material

identification as the atomic number and geometry dependent properties, μ/ρ and ξ, are not known. The areal density can be decoupled from Equation 4.2 by solving for the attenuation coefficients of each energy independently then taking a ratio of one to the other to produce a figure of merit as shown in Equation 4.3.

$$R(E_1, E_2, Z) = \frac{\ln T(E_1, Z)}{\ln T(E_2, Z)} = \frac{\mu(E_1, Z)}{\mu(E_2, Z)} \tag{4.3}$$

Gamma rays of different energies traversed the same material, being exposed to the same energy independent areal density. When the ratio is applied the ξ / ξ term equals 1 leaving only the measured energy dependent transmission ratio equal to the atomic number and energy dependent attenuation coefficients. The differential attenuation of these two prominent gamma rays provides a unique solution representing a ratio of linear attenuation coefficients.

The interrogated material will almost always be some sort of composite, not pure elemental material. The effective atomic number, Z_{eff}, of a bulk material can be defined as a hypothetical single material that exhibits an equivalent attenuation coefficient ratio to that of the bulk. Rewriting Equation 4.2 to account for a composite containing i independent materials yields Equation 4.4.

$$T = \Pi_i e^{-\frac{\mu}{\rho}\xi_i} = e^{-\Sigma_i \frac{\mu_i}{\rho_i}\xi_i} = e^{-(\frac{\mu}{\rho})_{\text{eff}}\xi} \tag{4.4}$$

The calculated transmission ratio of the composite material can be applied to the figure of merit, Equation 4.3, resulting in the effective mass attenuation coefficient. The calculated ratio can then be compared to tabulated values from NIST XCOM to assign a Z_{eff} from the closest matching material. In the grand scheme of things, it doesn't really matter how a photon interacts inside the interrogated material as it is assumed that any interaction removes it from the beam incident on the detectors. This assumption is not strictly valid as there is a small probability of Compton Scatter into a small solid angle, but given the large

distance is a good approximation.

This attenuation coefficient ratio relationship was evaluated by measuring the relative photon transmission of various materials with atomic numbers from 13 to 92 including Al, Fe, Cu, Mo, Sn, W, Pb, and U. The transmission objects were machined to obtain an approximate areal density of about 20 g/cm^2 to eliminate its dependency from Equation 4.2. The materials were placed approximately 1 meter from the boron target as shown in Figure 3.5 to cast a complete shadow on the entire detector array approximately 8 meters away. The separation distance and collimation are more than sufficient to render build-up effects negligible. The energy dependent opacity of each object was measured for a time period of 2700 seconds using an average deuteron beam current of 21 μA producing the transmission spectra in Figure 4.4.

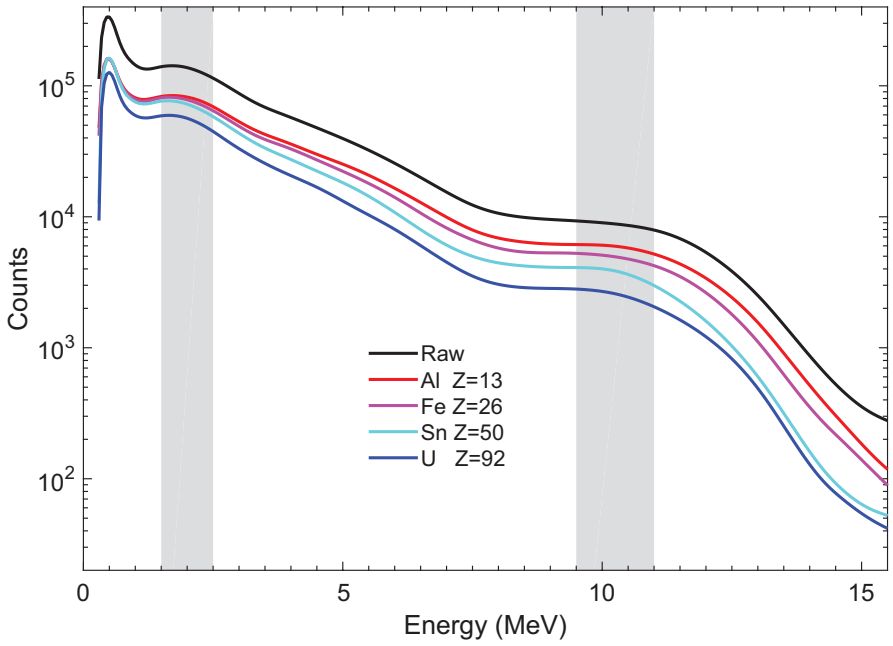

Figure 4.4: Selected transmission spectra through various materials to illustrate the differential attenuation as a function of energy and the integration regions used for analysis.

The integration regions for transmission analysis are denoted as the gray boxes in the background. These were determined based on the kinematics of the reactions inside the quartz material and the corresponding prominent features. These regions are simplified as

they do not include all the events in the detectors for the energy they are integrating. The 4.4–MeV region does include some contribution for the Compton continua of the 6.5 and 8.95–MeV gamma rays which causes a slight deviation in experimentally calculated ratios from theory in the mid–Z range seen in Figure 4.5.

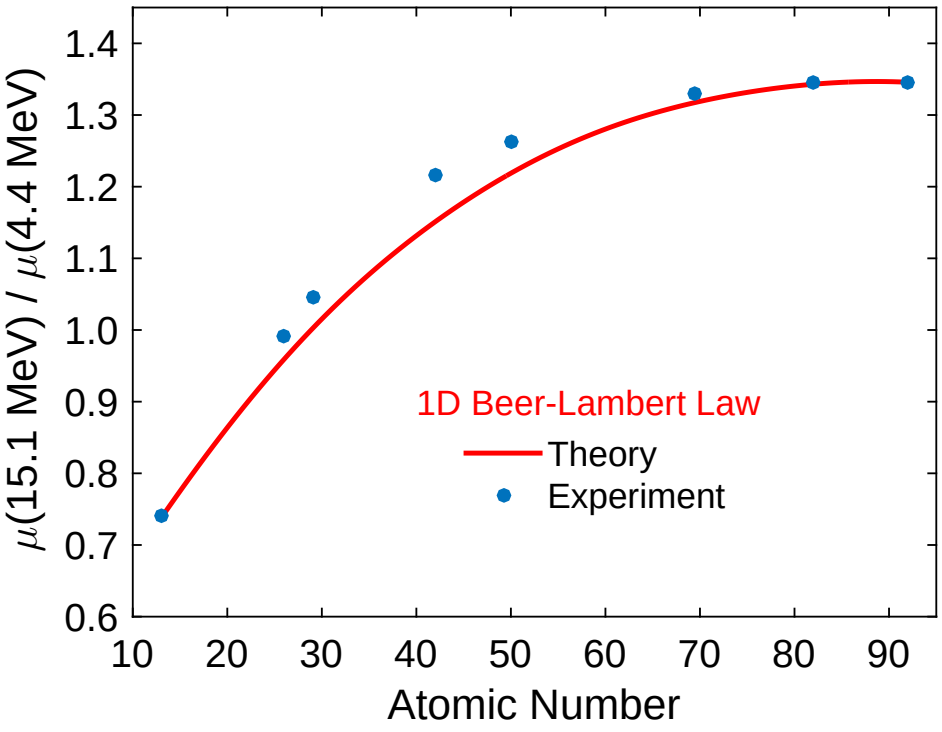

Figure 4.5: Comparison of experimentally obtained linear attenuation coefficient ratios (dots) and the theoretical Beer-Lamber Law (red line). Error bars on the experimentally obtained ratios are smaller than the markers used to portray them so they are omitted.

The error bars on the experimentally calculated ratios are smaller than the markers use to display them so they are omitted from the plot. The large separation in photon energies used for interrogation of the objects results in an improved ability to discriminate between low-, medium-, and high-Z materials. However, as the atomic number approaches about 70, the slope of the curve in Figure 4.5 levels off, and exact material discrimination becomes difficult using the 15.1/4.4–MeV relationship. The difficulty in exact discrimination in the high–Z range stems from the errors associated with these measurements slightly over lapping even though they are small as well as the slope of the theoretical curve approaching

zero with increasing Z.

The simplified integration regions recreate a curve close to the theoretical predicted Beer-Lambert Law. This curve can be fitted and stored for comparison of unknown materials in lieu of using tabulated data to reduce processing time associated with fully unfolding the transmission spectrum to isolate events from the energies of interest. Numerical details of the resulting transmission spectra can be found in Table 4.1.

Table 4.1: Objects used for transmission studies with constant areal density. The atomic number of W corresponds to the Z_{eff} of the copper tungstate alloy.

Material	Z	Thickness (mm)	4.4 MeV Transmission	15.1 MeV Transmission
Al	13	71.05	59.7%	66.9%
Fe	26	24.62	57.2%	56.3%
Cu	29	21.40	54.5%	52.0%
Mo	42	19.54	52.8%	45.0%
Sn	50	26.56	53.3%	44.2%
W	69.5	8.81	58.7%	48.2%
Pb	82	19.29	41.5%	30.1%
U	92	10.16	41.3%	29.9%

Transmission measurements of these materials illuminated a problem with the theoretical to experimental ratios of the tungsten sample. Initially it was assumed the material was pure tungsten metal, Z=74, however it was an outlier in all repeated measurements. Upon further investigation, it was found to be a copper – tungsten alloy, CuW90, with a Z_{eff} of 69.5. The experimental ratio of the tungsten material in Figure 4.5 accounts for the actual Z_{eff} of this material.

The integral transmission and Beer-Lambert Law approaches can be combined to produce two different images from the same set of data. The first type is the high contrast, two dimensional representation of the areal density previously shown in Figure 4.1, while the second is a graphical representation of the Z_{eff} traversed material. Figure 4.6 shows the results of energy independent and energy dependent imaging using the same data.

Figure 4.6 illustrates the energy independent transmission imaging method (Figure 4.6b)

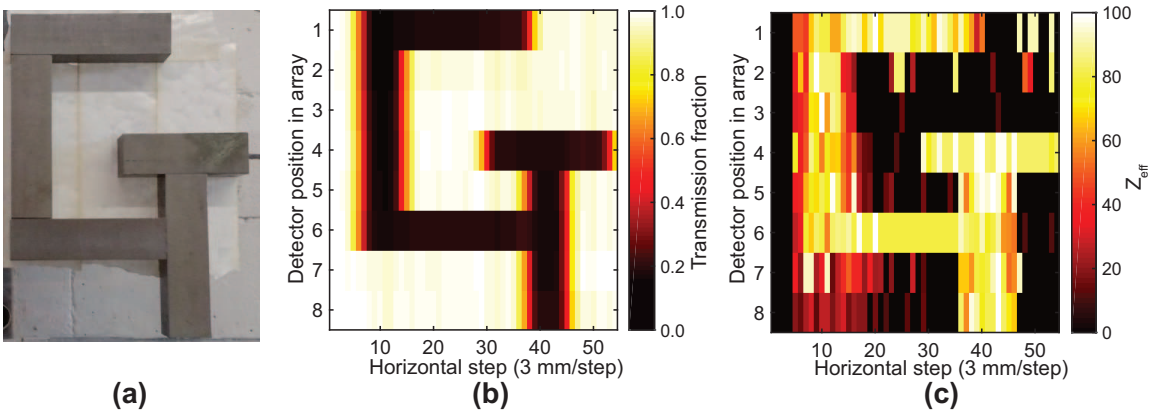

Figure 4.6: Transmission imaging and experimental reconstruction of atomic number Z of combined tungsten and acrylic object. (a) Photograph of the assembled object, with tungsten alloy bricks fixed to a sheet of acrylic to represent GT lettering. (b) Transmission image using the energy-independent integral approach. (c) Reconstruction of Z_{eff} of the object using 4.4-MeV and 15.1-MeV photons. Noise in the figure is due to forward scattering of high energy photons combined with accelerator fluctuations. Horizontal pixels are 3 mm translational steps while vertical pixels correspond to detector position in the vertical imaging array. Reproduced with permission from Rose [55]

and energy dependent method of material characterization via Z_{eff} calculation (Figure 4.6c). The approach to energy independent imaging is the same as Figure 4.1c. The Z_{eff} image is produced by integrating the regions corresponding to 4.4 and 15.1 MeV as described then employing the Beer-Lambert law to solve for the attenuation coefficient ratio, Equation 4.3. This produces a matrix with each element representing the average Z_{eff} for that pixel on a scale of 0 to 100. The Z_{eff} image has some noise due to the forward peaked scattering of high energy photons and fluctuations in the output of the accelerator. The integral image also suffers from scattering noise and accelerator fluctuations, however integration of the entire energy spectrum provides better statistics than the reconstruction of Z_{eff} due to the larger number of events considered.

A more challenging situation to evaluate this dual imaging methodology arises when considering composites and non-uniform thicknesses. In particular, one of the original goals of this imaging system is to search for SNM shielded by some other materials. An assembled object containing uranium used to demonstrate the imaging system in a more

complex scenario is shown in Figure 4.7.

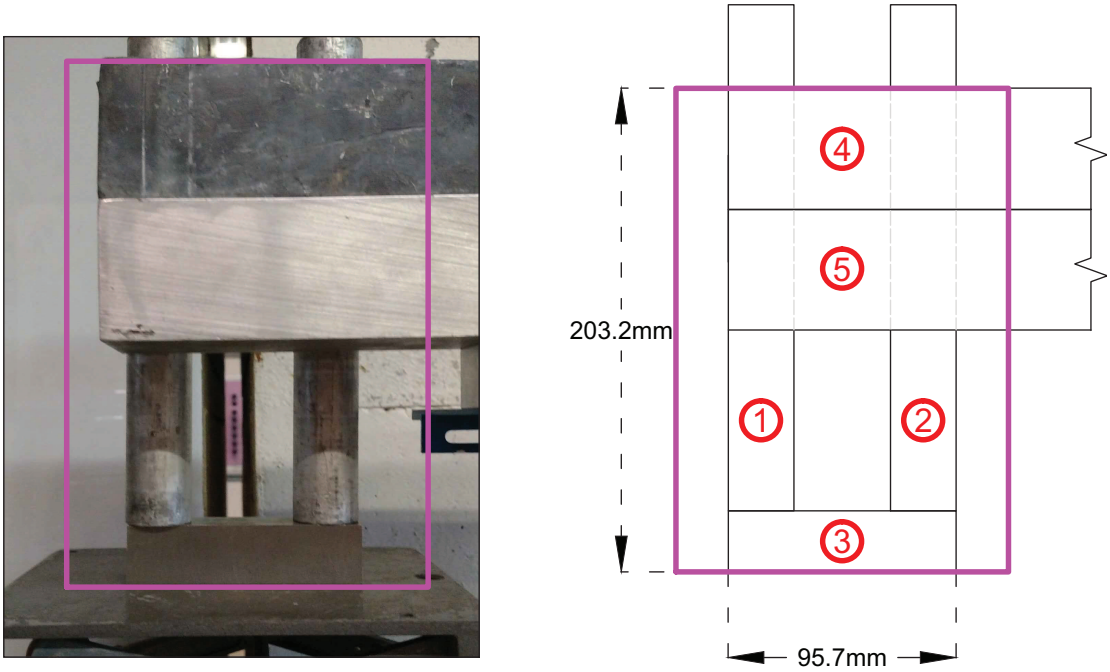

Figure 4.7: (A) Photograph of the object used for demonstration of transmission imaging containing partially covered uranium. (B) Scale drawing of the object. Items 1 and 2 natural uranium rods with aluminum clad and hollow cores, 3 tungsten block, 4 and 5 lead and aluminum plates suspended partialls shielding uranium rods. Reproduce in part with permission from Rose et al [7].

Figure 4.7a is the photograph of the composite object with a box superimposed on top indicating the portion of the photo casting a shadow on the detector array visible though the collimators. A schematic of the assembly is shown in Figure 4.7b where items 1 and 2 correspond to natural uranium rods with aluminum cladding and hollow cores sitting atop 3, a 25.60 mm-thick tungsten block, forming the letter "U" with approximate matching areal density. The bottom half of the uranium rods are bare with no shielding while the top half are covered by a 15.95 mm-thick lead region and a 52.22 mm-thick aluminum alloy region, items 4 and 5 respectively. The uranium rods weigh in at 2 kg each including the aluminum cladding. With a density of 19.1 g/cm^3 for uranium, each whole rod represents approximately 100 cm^3 of uranium matching the lower detection limit goal of the project.

The dual images associated with this assembly can be found in Figure 4.8

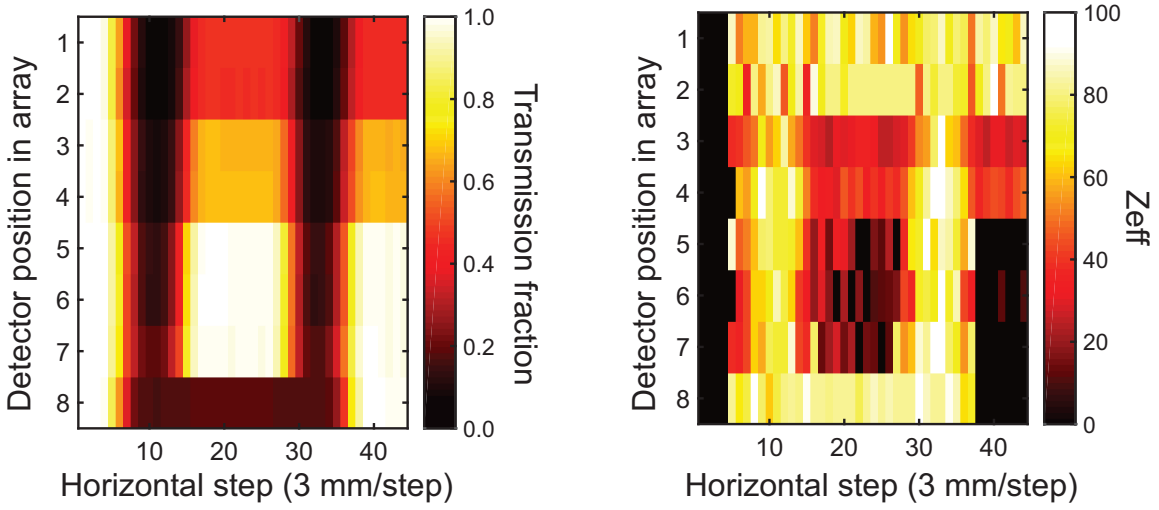

Figure 4.8: (a) Transmission image using the energy-independent integral approach. (c) Reconstruction of the energy dependent imaging approach producing an illustration of the Z_{eff} of the object using 4.4-MeV and 15.1-MeV photons. Noise in the figure is due to forward scattering of high energy photons combined with accelerator fluctuations. Horizontal pixels are 3 mm translational steps while vertical pixels correspond to detector position in the vertical imaging array.

These images were obtained and produced by exactly the same process and analysis as the previous images in Figure 4.6. The areal density map, Figure 4.8a, indicates approximately the equal areal density between the tungsten block and the uranium protruding from the shielding material while the areal density increases in the region where the uranium is covered by aluminum, and even more when the uranium is covered by the lead. This alone does not indicate the presence of high-Z material, only varying areal density.

The reconstructed Z_{eff} map, Figure 4.8b, indicates an abundance of high–Z material corresponding to the uranium, tungsten, and lead regions. The region associated with the aluminum is substantially darker, lower Z_{eff}, except in the region covering the uranium rods where high–Z material is still indicated. This shows sufficient spatial resolution combined with high–Z determination to resolve the portion of the uranium rod included in the image.

4.4 Image Reconstruction from Detector Array

The images presented here are reconstructed using a method that is simple and efficient to instantly produce images upon completion of irradiation. The detectors themselves stay in a fixed position while the object is translated in front of the beam in between the large concrete collimators. The translation of the objects is not continuous, it is fixed in place for a 300 second period of irradiation producing a matrix where the number of rows corresponds to the number of detectors in the vertical array and the number of columns corresponds to the number of translation steps in the image such as that seen in Figure 4.9.

1.1	1.2	1.3	1.4	1.5	1.6	1.7	1.8	1.9	1.....
2.1	2.2	2.3	2.4	2.5	2.6	2.7	2.8	2.9	2.....
3.1	3.2	3.3	3.4	3.5	3.6	3.7	3.8	3.9	3.....
4.1	4.2	4.3	4.4	4.5	4.6	4.7	4.8	4.9	4.....
5.1	5.2	5.3	5.4	5.5	5.6	5.7	5.8	5.9	5.....
6.1	6.2	6.3	6.4	6.5	6.6	6.7	6.8	6.9	6.....
7.1	7.2	7.3	7.4	7.5	7.6	7.7	7.8	7.9	7.....
8.1	8.2	8.3	8.4	8.5	8.6	8.7	8.8	8.9	8.....

Figure 4.9: Photograph (left) of the front face of the imaging detectors array aligned with (right) the numbered row - column matrix used to illustrate the image reconstruction and normalization concept.

The numbers in the grid correspond to the row.column or the (detector number).(translation step). Each row of the matrix corresponds to a single detector and is handled independently in the analysis code since the response of one detector does not depend on the neighboring detectors yielding the ability to parallelize the reconstruction process. The transmission integral of each translation step is normalized to the unimpeded integral of that detector, ie

$I_{8.7}/I_{0_{8.1}}$ is the transmission fraction in detector 8 at translation position 7 forming pixel 8.7. All images start with 4–5 steps of unimpeded beam so any of the first few steps can be used as I_0 in the calculations. In the interests of error reduction, the integral obtained from the first four steps of each detector are averaged to produce a more consistent unimpeded integral, $I_{0_{avg}}$, for the ratio calculations. This technique is applied to not only the full integral, energy independent transmission, but also to the energy dependent transmission.

Any two "identical" detectors will have slightly different responses to the same incident radiations due to many uncontrollable factors; imperfections in the crystal material, reflector, PMT, etc. Normalizing the detector response to itself at a known condition is an important feature of this reconstruction method because it erases the need for identical detectors with identical performance. Each detector uses a unique energy calibration so gain matching, PMT noise and performance, source anisotropy, and other fluctuations can be ignored.

Natural background has been measured with these detectors overnight to build up a spectrum. The inherent low energy discriminating physics of Cherenkov radiation makes these detectors immune to most of the low energy natural background leaving mostly just PMT noise detected. The average count rate in these detectors without a source is around 200 counts per minute which the count rate in the beam is on the order of 10^7 counts per minute. The orders of magnitude difference and the nature of the ratio methodology applied to the transmission spectra render background effects negligible and therefore they are not considered in the analysis code further simplifying and increasing the speed of image processing.

4.5 Enhancing Elemental Discrimination

This elemental discrimination method can be extended to more precise Z_{eff} calculations, especially in the high–Z range, by incorporating other energies. Chapter 3 showed multiple gamma rays produced from the ^{nat}B(d,nγ)^{12}C source that could be employed in addition

to the 4.4 and 15.1–MeV lines. The same transmission and ratio processes can be applied with these energies as the attenuation scales differently as a function of Z. A brief synopsis of the total attenuation as a function of material using some of the available energies can be found in Figure 4.10.

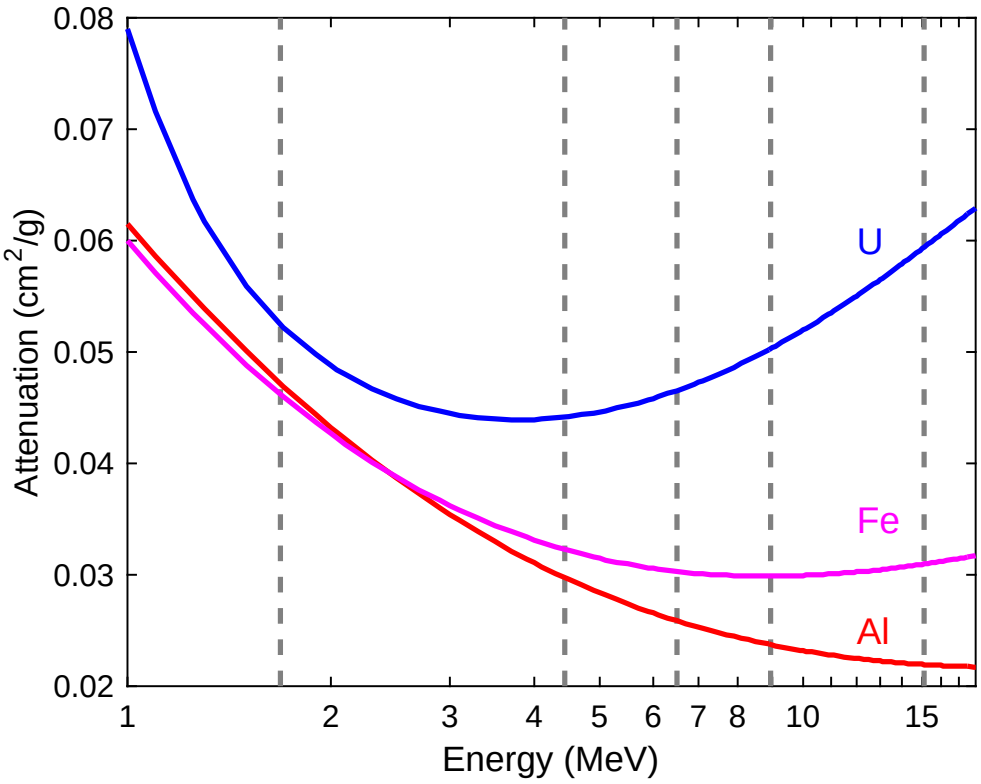

Figure 4.10: Total attenuation coefficient as a function of photon energy for select materials to illustrate the differential cross section scaling as a function of atomic number. The vertical gray lines represent intense gamma ray energies available for analysis from the low energy nuclear reaction driven source.

This plot is restricted to the energies available above 1 MeV due to the proximity of the lower energy gamma rays to the Cherenkov threshold energy which distorts the already sub-optimal energy resolution. In fact, the Cherenkov response to the 1.684–MeV gamma ray is nonlinear enough to be unreliable so it won't be included here. The addition of the 6.505 and 8.950–MeV gamma rays will not result in any additional discriminatory capabilities when applying the same ratio with $\mu_{4.4MeV}$. It is obvious the largest separation

in attenuation coefficient ratio will occur at the largest separation of of attenuation coefficients. These ratios were added to the same transmission data presented in Figure 4.5 resulting in the multi-ratio Cherenkov analysis found in Figure 4.11.

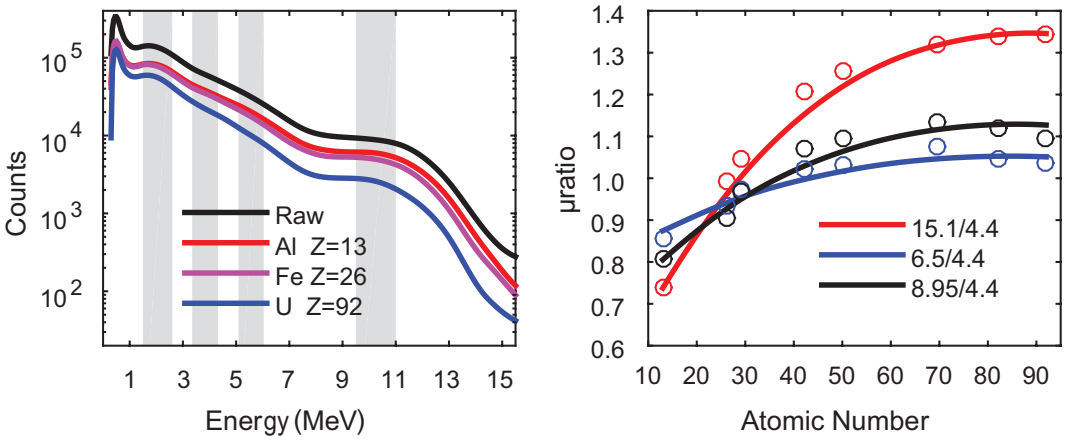

Figure 4.11: Example of multi-region integration (left) of Cherenkov transmission spectra to evaluate attenuation coefficients in multiple ratio (right) relationships. The Cherenkov detector array does not contain enough energy resolution to effectively take advantage of the potential multi-ratio analysis. Reproduced in part from Rose and Erickson [55].

The ratios calculated deviate from the theory, Beer-Lambert Law, due to the limited spectroscopic capability inherent to Cherenkov detectors. Applying detectors with superior energy resolution, such as LaBr or LYSO, may yield results that match the expected ratios based on theory. However, this still won't improve the elemental differentiation at high-Z because the slope of the theoretical curves approach zero even faster for these new ratios.

If the imaging system were a hybrid of detector technologies, such as Cherenkov intermixed with LaBr or LYSO, additional gamma analysis would be possible. Intense gamma rays are available at 0.511, 0.954, and 1.684–MeV. The full spectrum from this particular source is shown in Figure 4.12.

The 0.511–MeV line in particular could be interesting since the dominant interaction with matter switches from Compton Scatter at low-Z to photoelectric effect at high-Z, visible in Figure 4.2. Low energy gamma rays such as this would not make it through a cargo container in great abundance, however there is a massive amount produced in the boron tar-

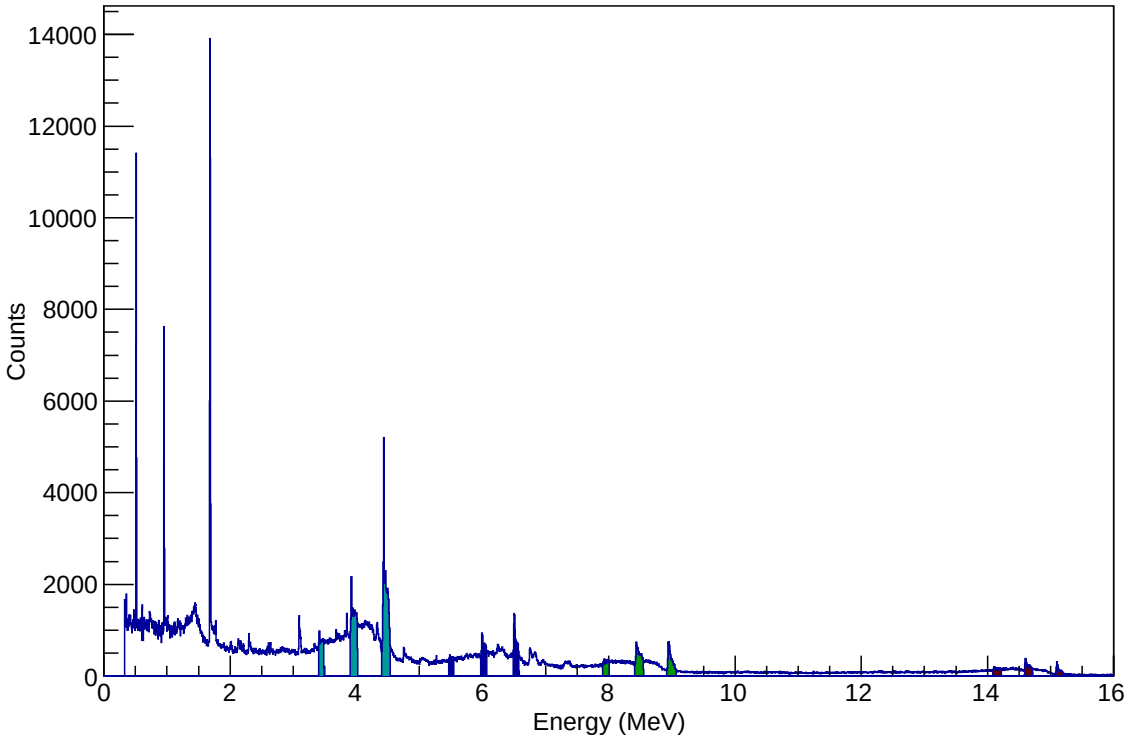

Figure 4.12: High resolution spectrum of the ^{nat}B(d,nγ)^{12}C source to illustrate the available gamma ray energies for transmission analysis including the highly intense gamma rays below 2 MeV.

get region. Incorporation of the 0.954 or 1.684 MeV lines would be more beneficial since they are abundant and more penetrating than the 0.511–MeV. These modifications to the detection system and analysis could result in many ratios that exhibit better discrimination at high-Z as shown in Figure 4.13.

This figure is just a snapshot of the ratios available, keeping the attenuation coefficient in the denominator constant for each plot except one where the numerator is kept fixed at 15.1–MeV. The analysis algorithms can be expanded to use one ratio, such as the established 15.1 to 4.4–MeV, to identify a material as Z greater than 60, then another ratio can be applied for better discrimination in that region. The proposed modification to the imaging system constructed and used in this chapter is beyond the scope of the original project. The analysis methods and tools are ready for the extension, however it will be left to future

work.

4.6 Improvements and Future Work

Transmission imaging techniques are a powerful tool with many applications, the focus here being nuclear security. The method laid out in this chapter is not unique to just one source, any source with well separated gamma rays can benefit from this work. One source of particular interest is Inverse Compton where photons of a single energy can be applied erasing the need for spectroscopy. The source can be adjusted to select a second energy resulting in the same areal density decoupled ratio analysis presented here.

The images obtained as part of this thesis were produced by translating the object in discrete increments to form each pixel. A constant motion method would be used in a deployed system where the horizontal pixels would be a function of some time integrated portion of the counts received relative to the position. This would require an additional layer of processing to the analysis algorithms but it should decrease the over all scan time required.

Other improvements to the elemental discrimination of this imaging system could include integrating multiple detector technologies as mentioned in the previous section. The spatial resolution of the system could also be increased by the use of smaller detectors arranged close together. The beginning stages of these two potential improvements will be addressed in the next chapter.

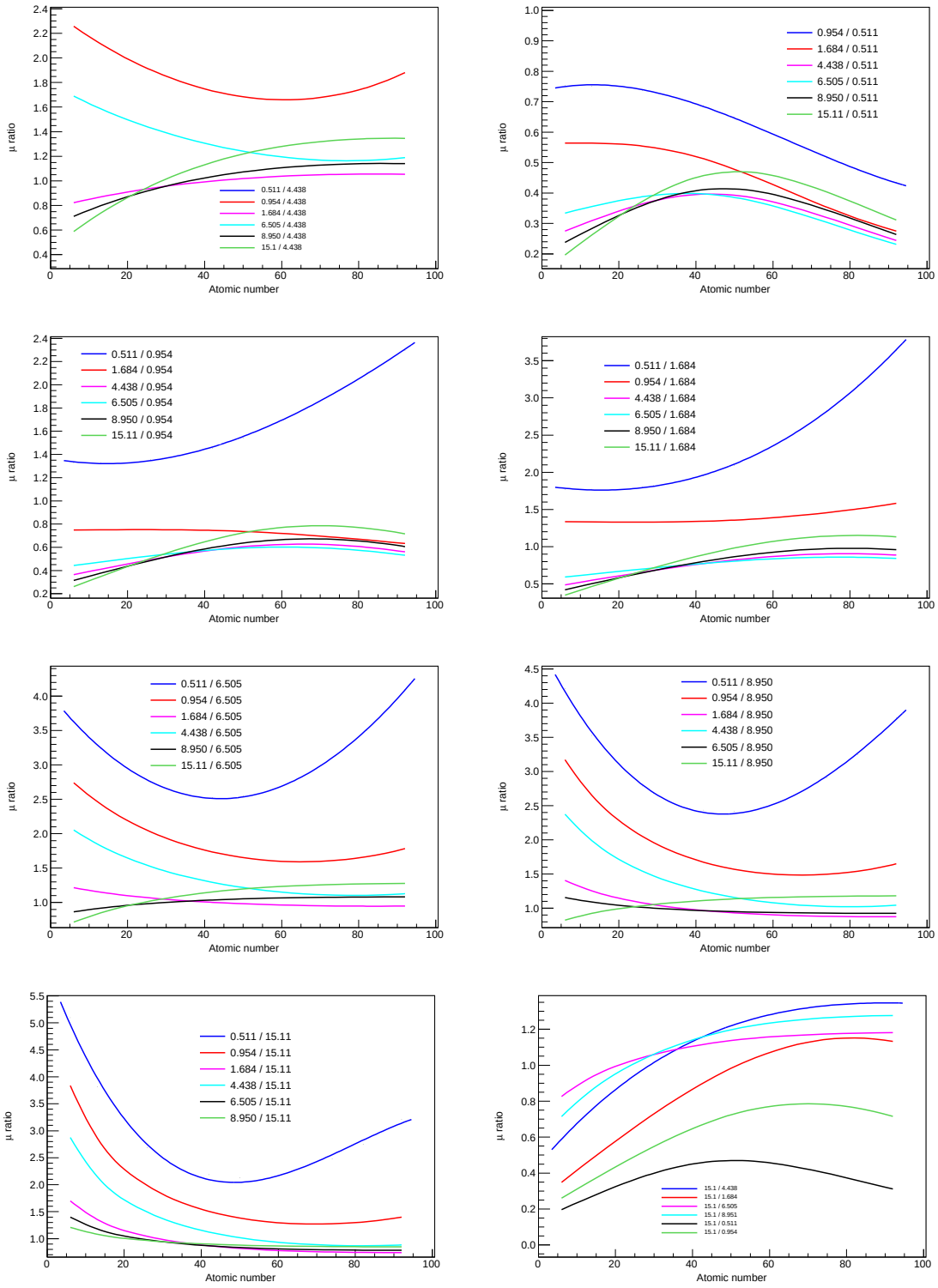

Figure 4.13: Overview of some of the possible ratios and material identification capabilities using the prominent gamma ray energies of the ^{nat}B(d,nγ)^{12}C source if detectors with moderately high energy resolution are employed for Z_{eff} discrimination.

CHAPTER 5

THE NEXT GENERATION IMAGING ARRAY

The never ending march of scientific advancements constantly produces new and exciting technologies available to improve upon the current state of the art. Progress in photonic read out devices has enabled new types of advanced detection systems with capabilities beyond the standard photomultiplier tube (PMT), especially when it comes to hostile detection environments. The PMT relies on electrostatic fields to induce electron avalanches from accelerated photoelectrons resulting from a photocathode. These fields can be heavily influenced by external factors such as magnetic fields and even neighboring PMTs if they are placed too close together causing a loss of gain or complete inoperability in extreme cases. Recent developments in semiconductor based optical photon detectors, such as silicon photomultipliers (SiPM), has led to a whole new arena for detectors [58].

SiPMs operate with a supply voltage far less than PMTs, 30 V versus 1000 V, eliminating the need for costly high voltage power supplies. These photon sensors are mechanically robust, radiation hard, operable at high count rates, geometrically compact, and insensitive to magnetic fields. They can be tightly tiled, sub-micron separation of sensitive areas, to fabricate detectors in a wide variety of complex geometries, materials, and light readout configurations.

One of the most exploited properties of SiPMs is the superior timing capability over PMTs for high energy physics experiments when using Cherenkov radiators [59]. Some studies have shown a coincidence timing resolution as low as 30 ps [60]. These studies applied the sensors in Geiger mode to fully utilize the timing properties ignoring any spectroscopic capabilities that may be present.

A version of this technology has been around for years, however technological advances and reductions in cost make SiPMs attractive alternatives to traditional PMTs in low light

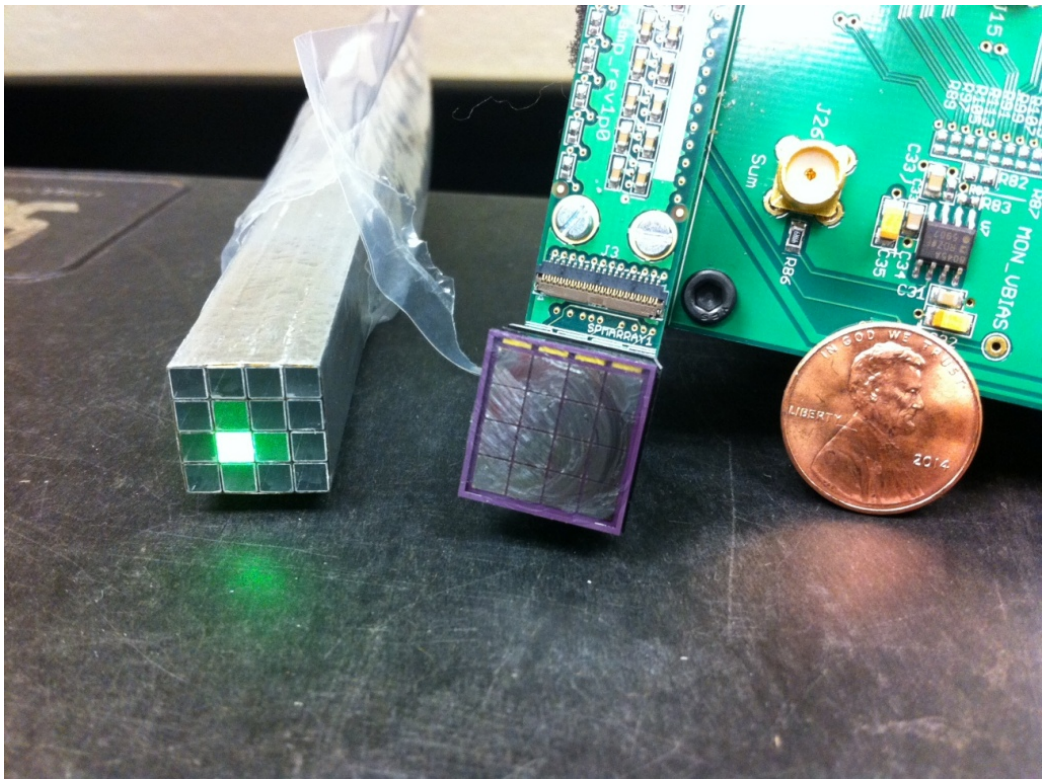

Figure 5.1: Photograph of 4x4 tiled array of 3x3 mm SiPMs and a custom designed segmented, individually reflected and light proofed, borosilicate glass Cherenkov array with one pixel illuminated with a laser to illustrate optical isolation including a penny for size reference.

situations such as Cherenkov. The imaging array presented in the previous chapter has satisfied the original goal of the specified project based on the cost effective performance of PMTs at the beginning of the project. However, since this work began the tides have turned and now SiPMs can be effectively and economically deployed so an outline of the next generation prototype will be presented here.

Finer spatial resolution of the images can be realized by switching to SiPM based detectors, commercially available down to 1x1 mm. The sensitive area of these sensors is available in a square format leading to compact tiling to maximize pixel density. The over all length of the detectors can be reduces aw well without any loss in crystal length because the thickness of the SiPMs are on the order of 1 mm including the circuit board relative to the $\approx$10 cm length of PMTs.

5.1 Advances in Silicon Photomultipliers

Multiple SiPM technologies from SensL and Hamamatsu have been evaluated since the beginning of this project in search of an appropriate sensor for Cherenkov based detectors. The initial testing of each product always revolved around scintillator crystals to ensure proper configuration and operability in the event low light detection was not possible. All of this evaluation was completed with a CAEN DT5730 digitizer connected directly to the output if the SiPM without any additional amplification with the exception of one as noted below.

The main concern with SiPMs and Cherenkov revolved around electrical noise and dark current in the sensor itself. It is often difficult to separate legitimate signal from a few photons on the sensor from the dark current. One way to resolve noise issues is to cool the semiconductor and maintain a constant temperature, but this adds complexity and failure points to a system and is not feasible for a large scale imaging system.

One of the early tests utilized a 4x4 tiled array of SensL B-series 3x3 mm SiPMs. Measurements with CsI and Stilbene crystals showed promise at first, however the temperature of the integrated electronics increased until the only signal available was noise. One of these tests included active cooling using a standard computer fan constantly blowing air across the board and successfully achieved PSD capabilities with the Stilbene as shown in Figure 5.2.

Though PSD was achieved, the overall results were disappointing due to the dynamic range of the sensor. Stilbene is a low light output organic scintillator, refer to Chapter 2, yet still saturated in the presence of a PuBe evident by the neutron and gamma lobes curling upwards at high energies. The plot would normally extend beyond what is displayed at channel 16000, but saturation destroyed the energy capabilities above his range. The issue with heating and over amplification stems from the built in active electronics on the board, mainly a preamplifier, which are not user adjustable. The noise from the electronics

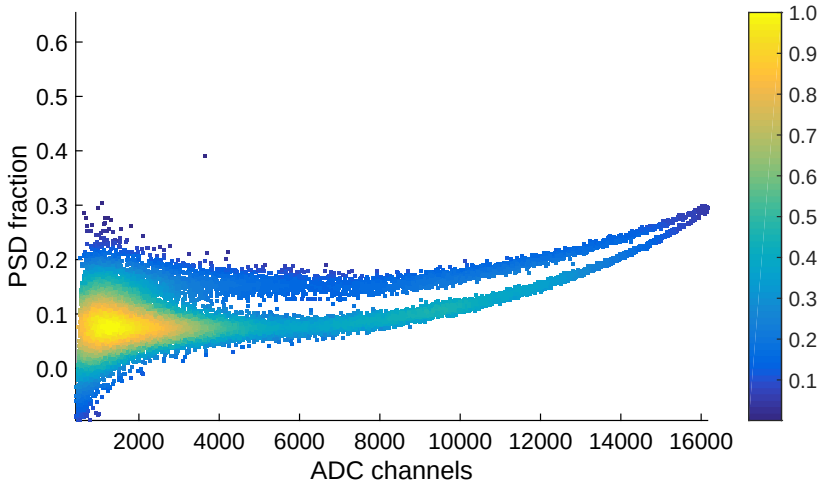

Figure 5.2: Illustration of limited pulse shape discrimination capability using a PuBe source of the SensL B-Series SiPM array coupled with a Stilbene crystal. This configuration suffered from saturation due to dynamic range limitation above channel 16000.

induced heating prevented and discernible Cherenkov measurements. Conversations with SensL resulted in a work around, but the main recommendation was a newly available piece of equipment with superior performance, the C-series.

Evaluation of the C-series consisted of a MicroFB-SMA-60035 which is a 6x6 mm sensitive area mounted on a low noise test board with SMA outputs. Unlike the B-series array, this equipment relies on an external, benchtop DC power supply that is variable. The voltage can be adjusted to tune the amplification of the signal. The CsI crystal in combination with a ^{137}Cs source was employed to produce Figure 5.3.

The experiment resulted in a clean spectrum of the source. The C-series is stable and did not suffer from large amounts of noise when used with a scintillator. However, tests with the Cherenkov radiator failed at incident energies up to 1.33 MeV.

The most recent product from SensL, the J-series SiPMs, is touted as UV sensitive and exhibits an order of magnitude less noise than its predecessor. The same form factor was used, MicroFB-SMA-60035, this time containing a 6x6 mm J-series sensor and was tested with LYSO and BGO crystals and a ^{232}Th source as shown in Figure 5.4.

These tests evaluated the use of the J-series with scintillators as well as the two high

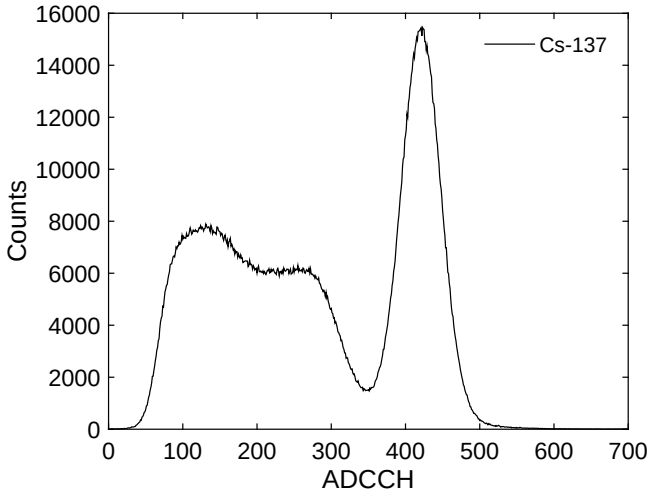

Figure 5.3: Spectrum of ^{137}Cs source obtained by a CsI(Tl) crystal coupled to a C-Series SiPM showing good spectroscopic capabilities.

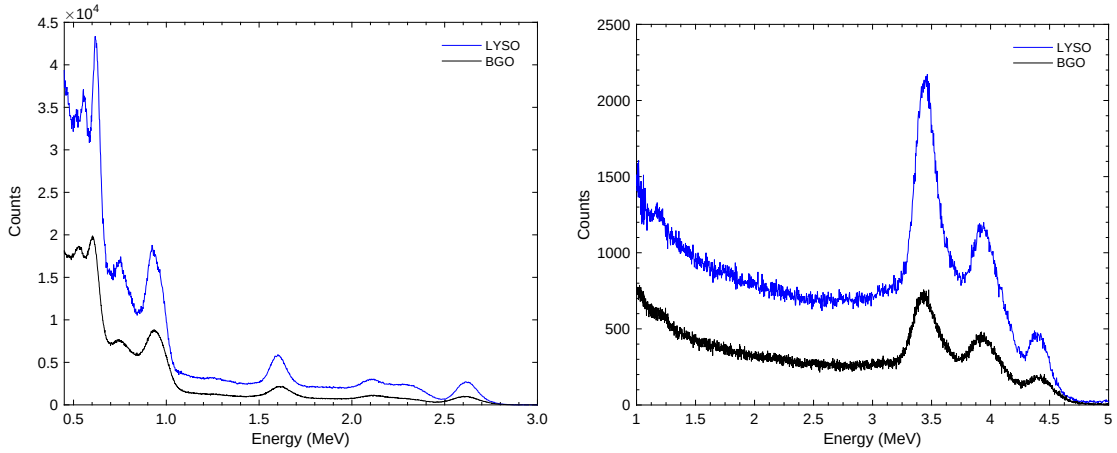

Figure 5.4: Examples of the SensL J-Series SiPMs coupled to BGO and LYSO detectors. The LYSO crystal consistently out performs the BGO crystal in both energy resolution and total number of counts due to the faster characteristic scintillation decay times.

density scintillators against each other. The sensor performed with no issues using either crystal and the background spectrum that includes noise was considerably smaller than previous generations. Cherenkov measurements were attempted with the same GE-124 quartz material as the previously presented PMT based detectors. The experiment started with waveform analysis in attempts to isolate a pulse and evaluate the noise as shown in Figure 5.5.

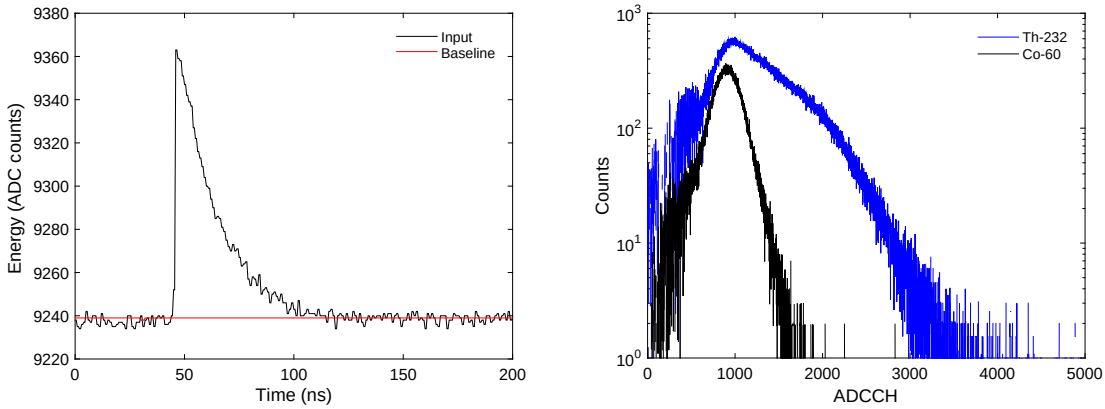

Figure 5.5: Isolated pulse (left) of Cherenkov radiation resulting from a 2.6 MeV gamma ray interacting in GE-214 quartz and crude spectroscopy (right) available from this Cherenkov crystal and SiPM combination.

The noise level of this sensor is low enough to be useful for Cherenkov radiators. Spectroscopy experiments were conducted using ^{232}Th and ^{60}Co sources to produce the plot shown in Figure 5.5. The spectra are not perfect as there appears to be an absence of signal below 1 MeV resulting from partial scatter in the detectors, most likely due to the extremely low light production. However, that may actually be beneficial in the final system to further reduce low energy signal processing to focus more on the high energy photons of interest.

The capability of Cherenkov spectroscopy in the J-series is due in large part to the increased photon detection efficiency, PDE, over a wider range of photon wavelengths. Most other SiPMs experience a drop off in PDE around 320 nm but the J-series extends into the UV region with a PDE close to 20% at 300 nm. Figure 5.6 shows the PDE versus wavelength of the J-series SiPMS reproduced with permission from SensL[61].

One important feature of this efficiency curve is the presence of PDE, approximately 6%, at 250 nm. Data below this wavelength is currently unavailable from the manufacturer, but it appears the PDE does continue in lower wavelengths in a reduced capacity. This sensor is ideal for use with scintillators as well due to the PDE 50% at 420 nm, a popular wavelength for many commercially available scintillators on the market. This is nearly double the efficiency of the Hamamatsu R6095 PMT, ≈27%, which is used in the previous

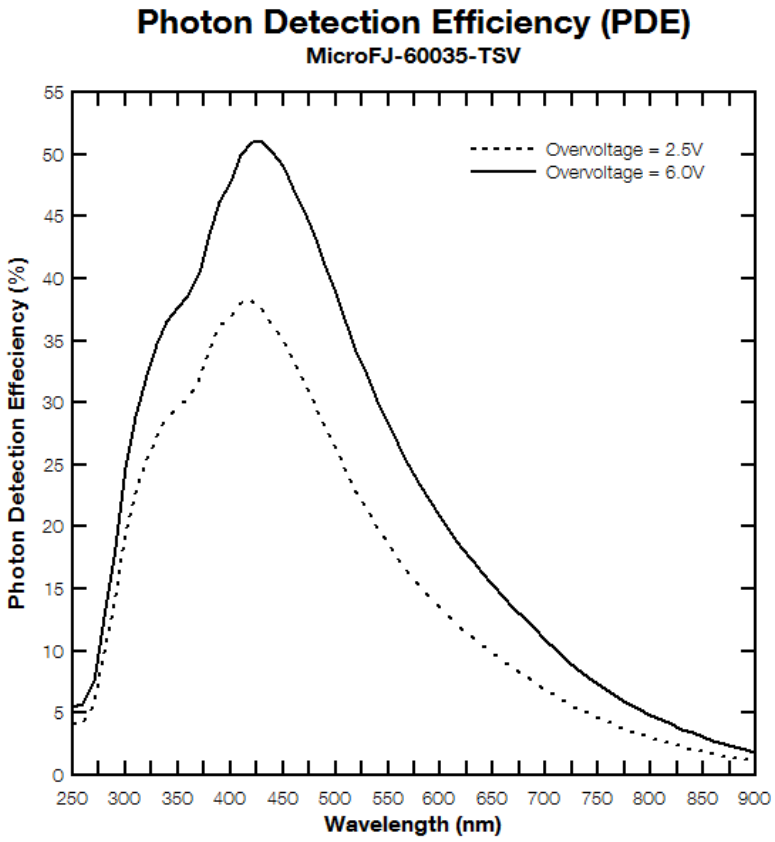

Figure 5.6: SensL J-Series SiPM photon detection efficiency as a function of photon wavelength showing >50% efficiency at 420 nm and increased sensitivity in the blue-UV region when compared to competing SiPMs. Reproduced with permission from SensL [61].

prototype array. This increase PDE leads to improved energy resolution with scintillators emitting in this region such as LYSO, 428 nm.

The current product offerings from SensL contain two different output modes, fast and standard, depending on the operation method. This is built in to each sensor so no extra equipment is necessary, some models can even operate both outputs at the same time. The main difference is the width of the output pulse as shown in Figure 5.7.

The fast output Figure 5.7(left) looks attractive for use in active interrogation systems with a pulse width of about 1 ns. However, this produces an issue with processing electronics needed to handle such pulses. The digitizer of choice in this thesis has been the x730 series from CAEN with a 500 MS/s sampling frequency. This equipment samples the

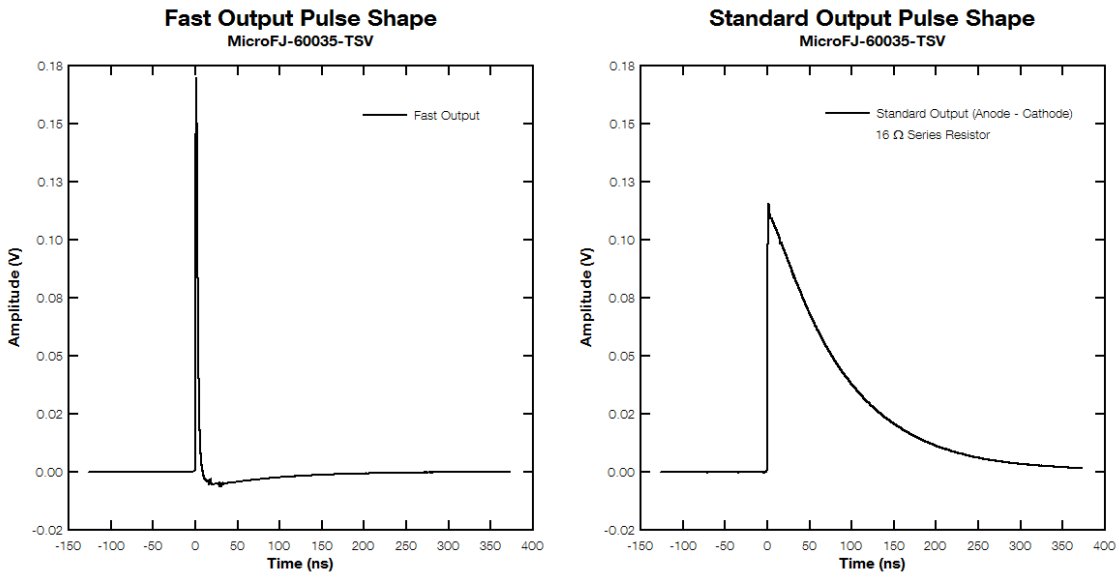

Figure 5.7: Example of pulses from dual output mode J-Series SiPMs available for use depending on application demands. Reproduced with permission from SensL [61].

signal every 2 ns, leaving a gap where a pulse from the fast output could come in and never be in the sampling window. Equipment with higher sampling frequencies are available, such as the 2 GS/s x751 series from CAEN, but are currently cost prohibitive. Even with this faster equipment, spectroscopic capabilities would not be available.

The experimental results employing the J-series presented thus far have have operated with the standard output. Figure 5.7(right) shows a pulse width of about 350 ns with the base sensor which is not fully optimized for timing. The SMA configuration evaluated here does include some optimization indicated by Figure 5.5(left) where a complete pulse, resulting from Cherenkov emission of a 2.6 MeV gamma ray, lasts only 55 ns before returning to the baseline.

The use of scintillators in active interrogation applications has already been explored in Chapter 2 of this thesis. One of the most promising materials identified through evaluation was LYSO based crystals due to the high density, fast decay time, and hydrophobicity. This material has recently been the focus of research for medical technologies such as PET where efforts have been applied to examine the relationship of energy resolution, timing,

and depth of interaction to the geometry and surface finish of the crystal [62]. Studies have been completed using identical crystals with varied surface finishes; mechanically polished, chemically polished, saw cut, and matte finishes [63, 64]. The optimal surface finish from these studies has varied due to the different geometries from one experiment to the other.

A similar study was conducted with 6x6x50 mm LYSO crystals where one crystal was mechanically polished on all sides and the other contained one face highly polished to couple with the SiPM and the other sides were ground to a 250 grit matte finish. The study used two different matte crystals and one polished crystal applied separately to the same SiPM to be as consistent as possible. All testing used identical settings and PTFE tape wrapping technique for the reflector producing the spectra found in Figure 5.8.

The crystals were exposed to a ^{60}Co source for initial comparison purposes. The polished crystals produced a relatively standard spectrum expected based on previous tests. The matte crystals produced a spectrum with the two peaks smeared over a wide energy range depending on where they interacted in the crystal. The gamma rays interacting closest to the SiPM produce light that is almost immediately collected without losses from reflection. The responses from the two gamma rays interacting closest to the SiPM are denoted as A and B on Figure 5.8(bottom). However, the most probable interaction region of the crystal is in the end closest to the source. Although the same amount of light is produced regardless of where the gamma ray interacted assuming full energy deposition for discussion purposes, The light produced far from the SiPM reflects off the surfaces multiple times. The matter finish reduces the internal reflection of the crystals leading to less light collected by the SiPM , therefore registers as a lower energy shown as C and D. Events in A and C are the same 1.33–MeV gamma ray where B and D are the same 1.17–MeV gamma ray only acting at different ends of the crystal. The matte finish produces a means of determining the depth of interaction of a known gamma ray in the crystal, especially if SiPMs are mounted to each end of the crystal. However, determining the depth of interaction is not desired in this application. The matte finish destroys spectroscopic capabilities

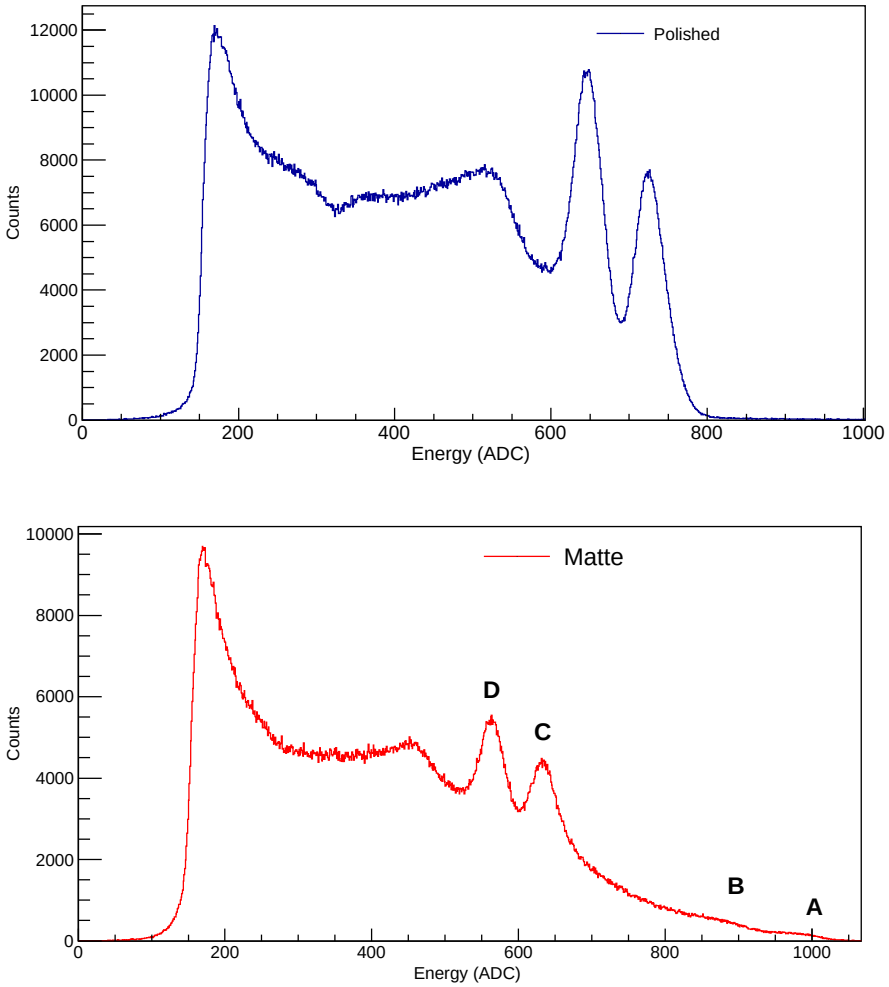

Figure 5.8: Evaluation of LYSO crystal surface finish using a ^{60}Co source where the polished crystal (top) produces an acceptable spectrum while the matte finished crystal (bottom) exhibits significant spectral degradation depending on the location of the gamma ray interaction. (A) illustrates the light output if the 1.33 MeV gamma ray interacts close to the SiPM while C shows the same gamma ray interacting close of the face farthest from the SiPM, which is the most probable, and suffers from reflection losses.

of the crystals in this case, thus polished crystals are required.

5.2 A New Prototype Array

A single sensor type, such as the J-series from SensL, could be employed to leverage both Cherenkov and scintillator based materials in an imaging array. The use of a single photon sensor reduces costs and complexity of the system by using the same custom

circuit board designs and readout electronics. The only variation from a LYSO based pixel to a Cherenkov based pixel is the voltage applied, 26.5 versus 28.5 V respectively. The Cherenkov sensors require slightly more voltage to increase the gain of the low light signal for processing. The most expensive piece of the assembled system would be the scintillator crystals due to the growth, cutting, and polishing processes. However, these could be intermixed in the array providing an image with high spatial resolution with some pixels containing high energy resolution capabilities.

5.2.1 Equipment Selection and Evaluation

An array was constructed on a breadboard consisting of five Cherenkov based pixels and five LYSO based pixels to continue evaluating the equipment on a larger scale. Two of the LYSO crystals were the matte finish and the other three were the mechanically polished crystals. The sensors in this array are SensL MicroFJ-SMTPA-60035 boards with pin outputs as seen in Figure 5.9.

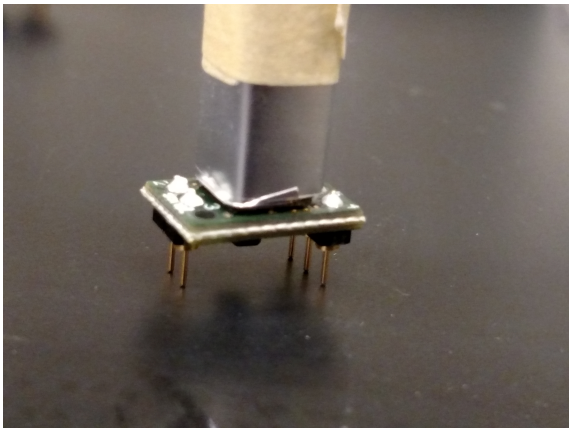

Figure 5.9: Photograph of SensL J-Series SiPM, MicroFJ-SMTPA-60035 board, coupled to a 6x6x50 mm LYSO crystal for assembly into a prototype evaluation array.

These are J-series SiPMs, 6x6 mm, mounted to evaluation boards without any active electronics or optimization. They are a convenient package for initial laboratory experiments because the pin outputs are designed to match the spacing of a standard breadboard. A total of ten pixels were arranged on the breadboard in two staggered rows of five, then

mounted in a light proof box as seen in Figure 5.10.

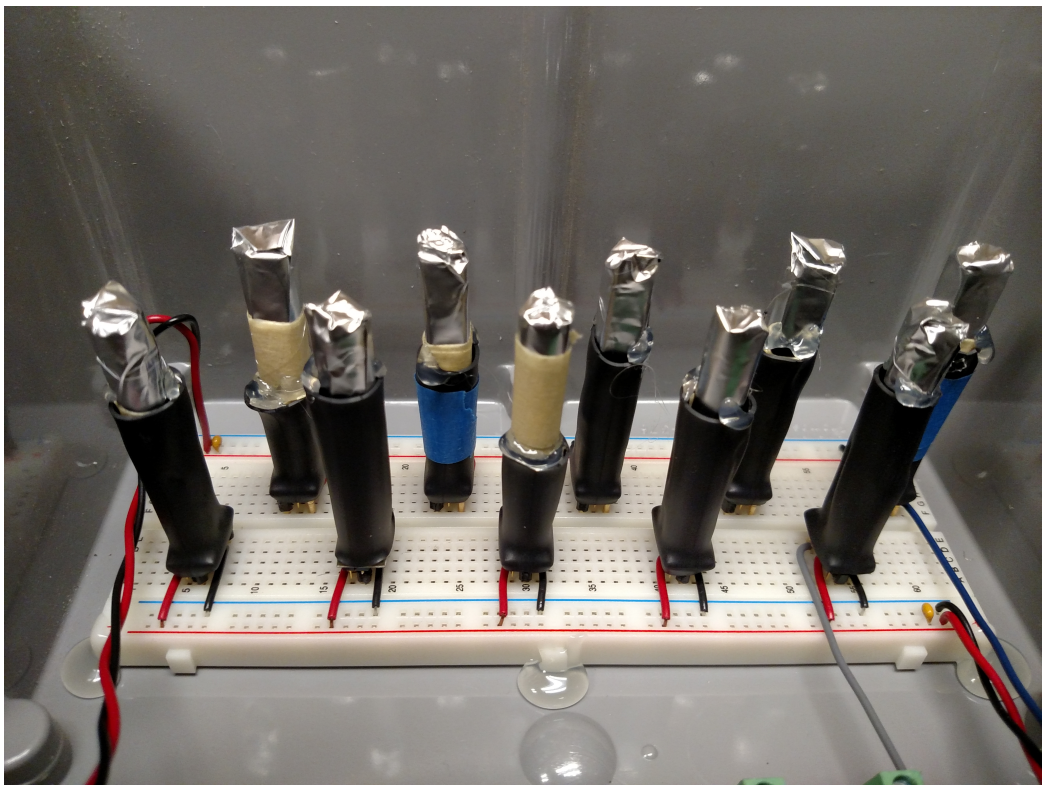

Figure 5.10: Assembled SiPM breadboard array of 5 LYSO and 5 Cherenkov crystals in a black box.

This array was constructed as a preliminary tool to evaluate the LYSO and Cherenkov based sensors with high energy photons in a convenient package. It is not intended to reflect the final design no is it optimized for noise, recovery timing, or energy resolution due to the materials used in assemble, mainly the breadboard which usually operates in the tens of MHz range. High energy, mixed field evaluation of this equipment was performed at Bates Engineering and Research Center in Middleton, Massachusetts with the accelerator driven ^{nat}B(d,nγ)^{12}C reaction source producing photons up to 15.1–MeV resulting in the spectrum found in Figure 5.11.

The LYSO crystal and J-series SiPM combination was able to operate across the entire desired energy range. The low energy gamma rays resulted in distinct peaks and with proper peak extraction could be used in ratio analysis. However, the circuit design was not

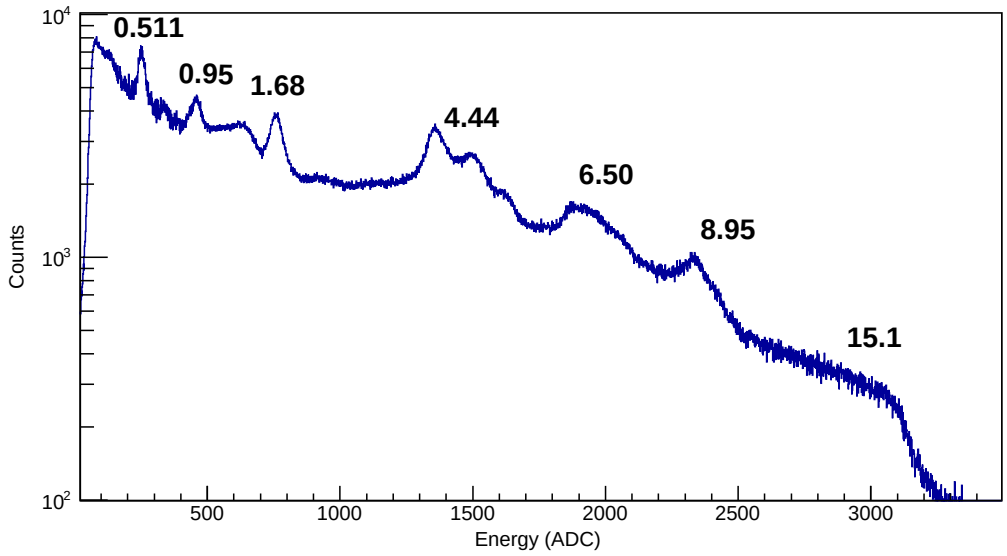

Figure 5.11: Full beams spectrum obtained from a J-Series SiPM with a 6x6 mm polished LYSO crystal assembled with non-optimized circuitry yet still capable of moderate energy resolution.

optimized resulting in noisy and long pulses which caused pulse pile up and a reduction in energy resolution, especially in the high energy range. The spectrum is not energy calibrated due to the lack of distinct photopeaks or other features in the high energy range. Another issue that needs to be addressed in the circuit design is the non-linearity in the high energy region. Even with these issues, the resulting spectrum has more energy resolution that the previous Cherenkov array so similar analysis should be possible.

Optimization of the electronics and board design is being handled by an expert in high frequency electrical engineering to produce the next generation prototype array that will be evaluated as an imaging array. These designs should minimize the series resistance of the output of each SiPM to minimize recovery time. Currently this is done with a termination resistor, however a transimpedence amplifier (TIA) could be applied instead. The TIA directly amplifies the photocurrent removing the series resistance effects, thus minimizing the recovery time. Applying a high bandwidth op-amp should produce the fastest recovery time according to conversations with SensL application engineers.

5.2.2 Conceptual Array Configuration

An array using both Cherenkov and LYSO could provide a significant improvement in spatial resolution and material discrimination at the same time. All pixels would be used towards the basic transmission image, but they could be used differently in the Z_{eff} images. The Cherenkov based detectors have already been shown to provide coarse material identification, the addition of LYSO crystals contain enough energy resolution to apply multiple ratios presented in section 4.6 of this thesis. The next array may be vertically stacked or staggered as seen in Figure 5.12.

This array of 6x6–mm SiPMs can be tightly tiled together to create a vertical column of sensors at some spacing, referred to as "A.2". This can be as small as 1–mm depending on the level of crosstalk. The crystal on each pixel are a series of LYSO, (L), and quartz Cherenkov, (C), crystals. The high-Z of the LYSO crystals will result in mostly pair production events with a high probability of 511–keV gamma rays escaping the crystal. One way this crosstalk is minimized is by separating the LYSO crystals with Cherenkov crystals which will attenuate the 511–keV gamma rays without registering an event as those gamma rays are below the Cherenkov threshold. The dominant interaction in the Cherenkv crystals, even at the high energies, is Compton Scattering which is highly forward peaked. The simulations will show an optimal separation, A.2, to reduce the cross talk events while maximizing the spatial resolution. This concept yields the ability to use the raw number of counts from the Cherenkov crystals and the energy resolution from the LYSO crystals in an advance image reconstruction algorithm that uses the data from the neighboring pixels to infer more information about each pixel. One such example could be to average the energy integrated peaks from two LYSO crystals and scale the product to the counts received in the Cherenkov crystal between them. This would effectively make each pixel in the array capable of multi-ratio analysis from spectroscopic measurements while reducing the overall cost of the system.

Another potential layout is shown on the right in Figure 5.12 where the array is broken

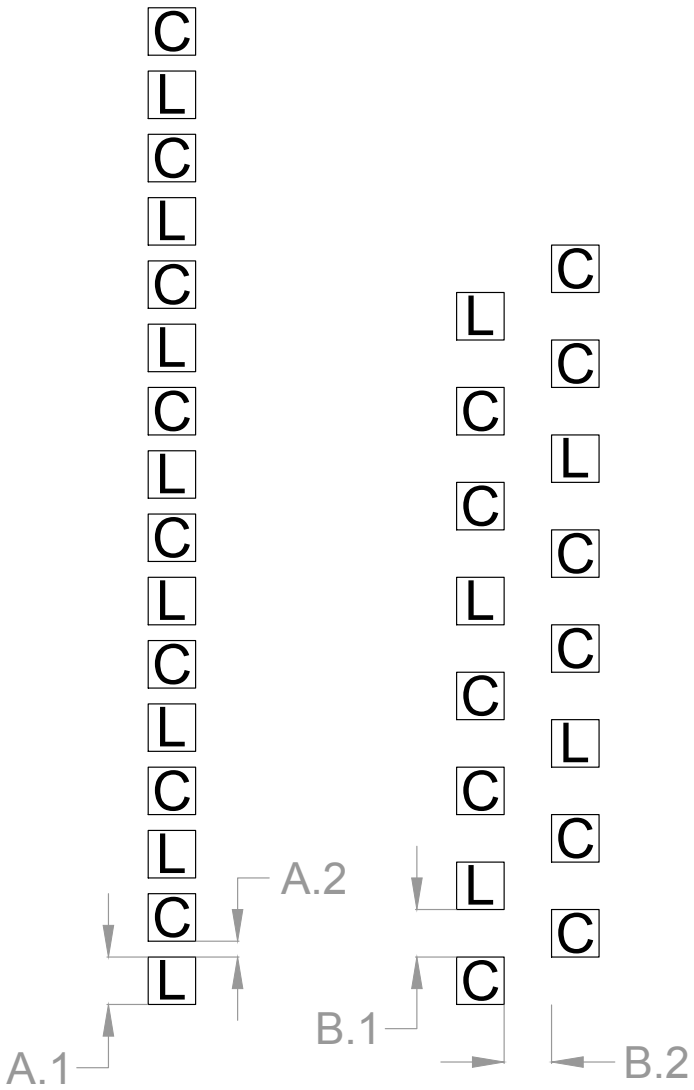

Figure 5.12: Two conceptual array design currently under investigation for image quality and crosstalk optimization. "L" and "C" denote the possible location of LYSO and Cherenkov crystals respectively.

down in to multiple columns. This would allow for greater spatial resolution in the vertical direction as dimension B.1 could be less than 6 mm. In this concept, the LYSO crystal is essentially surrounded by Cherenkov crystals in the effort to reduce crosstalk. Similar algorithms could be used to infer spectroscopic information from surrounding pixels as the object is translated horizontally. This concept uses less LYSO crystals, the most expensive

component of this system, yet provides better spatial resolution with less crosstalk.

The exact layout of the custom designed arrays and PCB boards are yet to be determined as simulations are currently under way to optimize the configuration for both spatial resolution and crosstalk. These simulated designs will also have to play into the next generation image reconstruction algorithms. These issues are beyond the original scope of this thesis and will be left to future work.

5.3 Future Work

The new prototype array is to be designed and constructed for larger scale imaging experiment. Simulations are currently under way to evaluate the optimal sensor and crystal combination layout. These simulations will determine the exact spacing of the intermixed crystals to minimize cross talk while maximizing spatial resolution.

Upon completion of the simulations, the final layout will be given to an electrical design firm that specializes in these types of applications. This will result in a final product that is properly designed optimized for active interrogation applications. Initial design meetings with the electrical engineer and a manufacturing contractor have already occurred and completion of the array construction is anticipated in the coming year.

The extended energy resolution capabilities of this array could be exploited by a custom data acquisition and analysis system. The new algorithms should communicate directly with the digitizer and perform on-the-fly analysis in the effort to reduce scanning time. One way this could be accomplished is to leverage all the available ratios for material discrimination to quickly clear a container.

CHAPTER 6
CONCLUSIONS AND FUTURE WORK

Detection of shielded special nuclear material hidden inside cargo containers is a complex task not easily achieved with today's state of the art scanning systems. The focus of this research has been the investigation and design of potential components for a novel, proof of concept active interrogation system to detect SNM. The main results are the descriptions, characterizations, and performance of experimental components for the first active interrogation system based on low energy nuclear reaction driven sources and Cherenkov detectors. The complete high resolution gamma ray spectrum resulting from the ^{nat}B(d,nγ)^{12}C reaction using 3.02–MeV deuterons was obtained and the major peaks were identified in both energy and probable origins to validate the application of the source in active interrogation. These tools were combined with a custom transmission imaging technique to provide coarse material identification through Z_{eff} unfolding from differential attenuation of discrete energy photons.

The purpose of this concluding chapter is to summarize the key results of certain components and overall operation of the proof of concept active interrogation system. A brief summary of potential improvements and future work discussed throughout the thesis will also be presented here.

6.1 Summary of Research Objectives

- Investigate the application of available detector technologies for use in harsh active interrogation systems where some level spectroscopy is required. Select or design custom detectors and construct a prototype imaging array capable of operation in high flux environments.

- Identify and describe the gamma ray spectrum resulting from the accelerator driven ^{nat}B(d,nγ)^{12}C reaction using 3.02–MeV deuterons. Determine the exact gamma ray energies available and attempt to identify the origin or origins to validate their use for transmission imaging applications.

- Develop techniques and algorithms to provide high contrast, two-dimensional planar images while simultaneously performing spectroscopic analysis to provide coarse material identification from transmission of discrete energy photons.

- Explore ways to combine detector technologies in a compact and efficient imaging array with high spatial resolution while still providing material discrimination.

6.2 Summary of Key Results

6.2.1 Detectors for Active Interrogation Imaging

The evaluation of available detectors and data acquisition in Chapter 2 resulted in the selection of equipment employed for active interrogation applications through the remainder of this thesis. One important result was a highly efficient, specially designed HPGe detector and preamplifier (TRP) combination capable of operation in high flux, high energy environments which proved crucial in characterizing the proposed active interrogation source.

The second key result from this chapter was the design of an imaging array based on custom Cherenkov detectors to provide an ultra fast, radiation hard detection system capable of crude spectroscopy. The inherent low energy rejection capabilities of Cherenkov detectors proved crucial to reduce unnecessary detection overheads from undesired low energy radiation and crosstalk effects. This imaging array was later applied along side the proposed low energy nuclear reaction source and imaging techniques in the proof of

concept experiments.

6.2.2 Low Energy Nuclear Reaction Source Characterization

The investigation presented in Chapter 3 of the ^{nat}B(d,nγ)^{12}C reaction using 3.02 MeV deuterons included computational modeling and experimental measurements. It is generally known that the actual gamma ray spectrum of the reaction can not be modeled due to the lack of cross sections and available nuclear data, however it can be a powerful tool in exploring nuclear reaction taking place to aide in understanding of experimental measurements.

This source was measured for the first time with high energy resolution using a custom modified HPGe detector and combined with a rigorous energy calibration technique to ensure high fidelity. The energy of the peaks was identified and potential parent reactions were presented to determine the main observable peaks originate in the target and therefore can be used in transmission measurements.

6.2.3 Transmission Imaging With Material Discrimination

Transmission imaging techniques using discrete energy photons were developed to produce high contrast, two dimensional images of areal density and coarse material identification from the same set of data in Chapter 4. An array of eight 25–mm diameter detectors were deployed to distinguish artifacts as small as 6.6 mm in diameter at a distance of approximately 9 meters from the source to the detectors. The high-rate Cherenkov detectors are suitable for transmission measurements and their crude spectroscopy does not present an obstacle to coarse material identification via differential transmission.

The proposed method is not unique to just one type of source or detector, it can be applied to any monoenergietic or quasi-monoenergetic source, for example Inverse Compton, and detectors with at least crude spectroscopic capabilities. Higher resolution's detectors, such as LYSO or LaBr, can potentially improve material identification through multi-ratio

differential attenuation measurements.

6.2.4 Next Generation Imaging Array

The evaluation of silicon photomultipliers, SiPMs, in Chapter 5 resulted in the identification of a room temperature semiconductor photon sensing device capable of Cherenkov spectroscopy. This work also showed the potential use of advanced sctinillators, such as LYSO, in a mixed detector array that will be constructed to perform high spatial resolution imaging as well as enhanced material identification.

The studies conducted identified the Cherenkov and LYSO materials as well as the J-series SiPM from SensL as the most promising technologies to combine for the mixed array. One key result of the component evaluation is the need for properly designed, high speed electrical circuitry for optimal recovery time and energy resolution results. Efforts are underway with such a design firm and manufacturing contractor to produce the proposed system.

6.3 Future Work

Investigation into the reactions and products of the source will continue in attempts to validate the life time and relative population of the nuclear states. This work will also try to fill in some of the gaps in the tabulated nuclear data in the hopes of creating simulation tools capable of recreating the correct gamma ray spectrum. Other nuclear reaction should be explored in this level of detail to evaluate them for potential use in active interrogation applications in the hopes of reducing dose to the cargo while improving material identification.

Completion and construction of the next generation imaging array will open the door to more advanced algorithms for improved material identification. This array should be tested with any active interrogation sources available in both transmission and imaging experiments.

One of the most cost prohibitive aspects of this type of system is the read out electronics. The detection industry in general would significantly benefit from smaller, low power, and less expensive enhancements in digital data acquisition and readout electronics.

6.4 Concluding Remarks

In conclusion, this research demonstrated a novel, proof of concept imaging application that employs a source of photons based on low-energy nuclear reactions. The high energy of the produced photons enables multi-energy transmission radiography as a method to discriminate between materials based on atomic number. Cherenkov detectors are low-cost,radiation hard, and inexpensive providing opportunities for practical large-coverage imaging.

This approach to active interrogation is highly flexible and applicable to a variety of sources — other nuclear reactions, Inverse Compton, etc — to generate highly penetrating, discrete energy photons. This source in particular is robust, producing both neutrons and gamma rays dependent on the target purity and design as well as the deuteron beam energy. The research presented here can be integrated with other efforts [9, 10] to offer significant advances in detection of shielded special nuclear materials.

Appendices

APPENDIX A

SIMULATED REACTIONS AND PRODUCTS

Table A.1: Particles generated and kinetic energy range as calculated by Geant4 at the time of emission from the 3.02–MeV deuteron – natural boron reaction.

Particle	# generated	Avg. Energy	Energy Range
B10	136787094	611.61 keV	(0.0088203 eV → 20.545 MeV)
B11	604350962	635.07 keV	(0.001779 eV → 22.289 MeV)
B12	49847695	636.23 keV	(159.43 eV → 10.236 MeV)
B13	30	1.5505 MeV	(746.57 keV → 2.9111 MeV)
B9	6491	1.1522 MeV	(2.775 keV → 3.5134 MeV)
Be10	1454743	1.5951 MeV	(70.28 eV → 12.991 MeV)
Be11	166477	1.3199 MeV	(256.54 keV → 3.8079 MeV)
Be7	700985	596.25 keV	(67.268 eV → 11.295 MeV)
Be8	416910	4.0917 MeV	(661.48 eV → 12.535 MeV)
Be9	92533057	3.5496 MeV	(121.81 eV → 19.993 MeV)
C10	42599	946.02 keV	(70.393 keV → 4.4406 MeV)
C11	79448571	749.43 keV	(5.0246 eV → 15.736 MeV)
C12	276883481	961.08 keV	(75.23 eV → 22.132 MeV)
C13	5955596	1.7847 MeV	(129.86 eV → 14.691 MeV)
C14	4629642	1.5769 MeV	(7.5423 keV → 15.097 MeV)
F17	38	3.2024 MeV	(1.2878 MeV → 5.1615 MeV)
F18	1585	2.9744 MeV	(707.93 keV → 12.709 MeV)
F19	1030	3.514 MeV	(679.29 keV → 11.943 MeV)
F20	264	5.0434 MeV	(1.4391 MeV → 11.195 MeV)
F21	10	4.6676 MeV	(2.5671 MeV → 8.4115 MeV)
He3	62598	3.9784 MeV	(36.39 keV → 14.749 MeV)
He5	1	2.7041 MeV	(2.7041 MeV → 2.7041 MeV)
He6	7905	2.5989 MeV	(28.845 keV → 15.411 MeV)
Li6	36723	4.4297 MeV	(254.21 eV → 22.014 MeV)
Li7	27321778	1.6881 MeV	(65.774 eV → 17.2 MeV)
Li8	1805439	2.2823 MeV	(148.97 eV → 8.6065 MeV)
N13	1029112	1.633 MeV	(10.873 keV → 13.244 MeV)
N14	23603981	1.5851 MeV	(18.464 keV → 15.28 MeV)
N15	29183	3.1398 MeV	(4.1515 keV → 14.997 MeV)
N16	1785	3.0523 MeV	(45.118 keV → 13.391 MeV)
N17	372	2.6044 MeV	(197.83 keV → 7.7641 MeV)

Table A.2: Cont. Particles generated and kinetic energy range as calculated by Geant4 at the time of emission.

Particle	# generated	Avg. Energy	Energy Range
N18	61	2.375 MeV	(578.64 keV → 5.4384 MeV)
Na21	1	4.4476 MeV	(4.4476 MeV → 4.4476 MeV)
Na22	31	6.0178 MeV	(3.7018 MeV → 10.524 MeV)
Na23	7	7.8335 MeV	(5.4599 MeV → 11.398 MeV)
Ne19	8	4.4614 MeV	(2.1865 MeV → 6.3697 MeV)
Ne20	1221	4.9901 MeV	(2.0169 MeV → 9.8235 MeV)
Ne21	388	5.2403 MeV	(1.8404 MeV → 9.9792 MeV)
Ne22	7	5.7414 MeV	(4.1832 MeV → 7.788 MeV)
O15	3271	2.8454 MeV	(145.02 keV → 13.759 MeV)
O16	17846	2.6047 MeV	(71.161 keV → 16.613 MeV)
O17	21082	2.8315 MeV	(121.98 keV → 16.175 MeV)
O18	392	3.6393 MeV	(211.78 keV → 12.462 MeV)
O19	185	2.7229 MeV	(932.1 keV → 5.4379 MeV)
alpha	1237318494	2.6844 MeV	(1.1289 eV → 38.425 MeV)
deuteron	85955933	2.2339 MeV	(1.0901 keV → 25.033 MeV)
gamma	747492461	2.8186 MeV	(1.5804 eV → 27.843 MeV)
neutron	785452267	6.4249 MeV	(3.6538 eV → 30.857 MeV)
proton	146715423	4.863 MeV	(177.12 eV → 26.038 MeV)
triton	5604196	2.5717 MeV	(3.4416 eV → 31.807 MeV)

Table A.3: Nuclear reactions and abundance as calculated by Geant4. Q-value based on mass balance only.

Reaction	# generated	Q-value
neutron + B11 → neutron + B11	355219386	94.259 eV
deuteron + B11 → neutron + 3 alpha	347638812	6.4586 MeV
deuteron + B11 → N gamma + neutron + C12	261268333	13.732 MeV
deuteron + B11 → alpha + Be9	91126897	8.0316 MeV
neutron + B10 → neutron + B10	79175770	97.863 eV
deuteron + B10 → N gamma + proton + B11	73022701	9.2298 MeV
deuteron + B10 → N gamma + neutron + C11	69835122	6.4646 MeV
deuteron + B11 → deuteron + B11	52454684	1.637e-06 eV
proton + B11 → proton + B11	45163689	-1.7438e-07 eV
neutron + B11 → N gamma + neutron + B11	37153128	-198.13 eV
deuteron + B11 → N gamma + proton + B12	35668716	1.146 MeV
alpha + B11 → alpha + B11	27530597	0.00060369 eV
deuteron + B10 → deuteron + B10	23158094	1.0105e-06 eV
alpha + B11 → neutron + N14	15403855	157.23 keV
deuteron + B11 → proton + B12	14169791	1.146 MeV
proton + B10 → proton + B10	12236237	1.1156e-07 eV
deuteron + B11 → neutron + C12	12113243	13.732 MeV
neutron + B11 → N gamma + neutron + alpha + Li7	11486000	-6.4845 MeV
deuteron + B10 → proton + B11	10090989	9.2298 MeV
deuteron + B10 → neutron + C11	9422196	6.4646 MeV
neutron + B10 → N gamma + alpha + Li7	8623301	2.7894 MeV
neutron + B10 → N gamma + neutron + B10	8555635	-119.87 eV
deuteron + B10 → 3 alpha	8228324	17.913 MeV
alpha + B11 → N gamma + neutron + N14	8191605	157.23 keV
deuteron + B10 → N gamma + deuteron + B10	6776816	1.6833e-06 eV
neutron + B10 → alpha + Li7	6036336	2.7883 MeV
alpha + B11 → proton + C14	4394904	783.57 keV
alpha + B10 → N gamma + proton + C13	4289836	4.0613 MeV
alpha + B10 → alpha + B10	4193119	0.00067569 eV
alpha + B11 → N gamma + alpha + B11	3099872	0.0012785 eV
neutron + B10 → 2 alpha + triton	2576347	2.9128 MeV
alpha + B10 → N gamma + alpha + B10	1734613	0.0010483 eV
neutron + B10 → N gamma + 2 alpha + triton	1711015	323.04 keV
alpha + B10 → deuteron + C12	1638669	1.3393 MeV
neutron + B11 → N gamma + alpha + Li8	1321562	-6.1603 MeV
alpha + B10 → proton + C13	1179203	4.0613 MeV
deuteron + B10 → proton + alpha + Li7	1149873	565.14 keV
alpha + B10 → neutron + N13	1028250	1.058 MeV
proton + B11 → N gamma + 3 alpha	802024	8.6481 MeV
neutron + B10 → N gamma + proton + Be10	750913	224.89 keV

Table A.4: Cont. Nuclear reactions and abundance as calculated by Geant4. Q-value based on mass balance only.

Reaction	# generated	Q-value
alpha + B11 → triton + C12	734021	-3.8575 MeV
alpha + B10 → N gamma + deuteron + C12	679811	1.3393 MeV
deuteron + B10 → neutron + alpha + Be7	661732	-1.0793 MeV
neutron + B11 → N gamma + 2 neutron + B10	651180	-10.065 MeV
proton + B11 → N gamma + proton + B11	528609	-35.594 keV
neutron + B10 → N gamma + deuteron + Be9	505944	-4.3644 MeV
neutron + B11 → alpha + Li8	483855	-6.7505 MeV
neutron + B10 → proton + Be10	459494	226.35 keV
neutron + B11 → N gamma + triton + Be9	371858	-9.5625 MeV
proton + B10 → N gamma + proton + B10	294600	-35.849 keV
neutron + B10 → deuteron + Be9	289164	-4.3619 MeV
alpha + B11 → deuteron + C13	269450	-5.1685 MeV
proton + B11 → N gamma + alpha + Be8	262092	8.5547 MeV
alpha + B11 → N gamma + proton + C14	230098	783.57 keV
proton + B11 → N gamma + neutron + C11	186950	-2.801 MeV
triton + B11 → N gamma + alpha + Be10	133098	8.5866 MeV
neutron + B11 → proton + Be11	111176	-10.746 MeV
neutron + B11 → triton + Be9	107280	-9.5593 MeV
alpha + B10 → proton + neutron + C12	105929	-885.07 keV
triton + B11 → neutron + alpha + Be9	105459	1.7743 MeV
alpha + B11 → N gamma + deuteron + C13	94594	-5.1685 MeV
triton + B11 → 2 neutron + C12	85685	7.4748 MeV
proton + B11 → alpha + Be8	82926	4.3763 MeV
Li7 + B11 → 2 neutron + alpha + C12	82924	5.0084 MeV
triton + B11 → N gamma + neutron + C13	74862	12.421 MeV
triton + B10 → neutron + 3 alpha	64044	11.655 MeV
alpha + B11 → N gamma + triton + C12	61866	-3.8575 MeV
neutron + B11 → proton + neutron + Be10	61797	-11.122 MeV
triton + B11 → N gamma + 2 neutron + C12	58815	7.4748 MeV
neutron + B11 → N gamma + proton + Be11	55301	-10.653 MeV
proton + B10 → N gamma + He3 + Be8	40917	-568.52 keV
proton + B10 → N gamma + neutron + C10	40375	-4.4668 MeV
neutron + B11 → N gamma + proton + neutron + Be10	35541	-11.224 MeV
proton + B10 → N gamma + alpha + Be7	33815	1.1093 MeV
alpha + B10 → 2 alpha + Li6	33394	-4.4605 MeV
triton + B10 → N gamma + deuteron + B11	29621	5.1968 MeV
triton + B11 → triton + B11	23638	-4.3915e-07 eV
proton + B10 → N gamma + proton + deuteron + Be8	21928	-6.0623 MeV
Li7 + B11 → N gamma + neutron + alpha + C13	20232	9.9547 MeV

Table A.5: Cont. Nuclear reactions and abundance as calculated by Geant4. Q-value based on mass balance only.

Reaction	# generated	Q-value
proton + B11 → 3 alpha	17348	8.6328 MeV
Li7 + B11 → N gamma + 2 neutron + O16	14951	12.169 MeV
alpha + B11 → 2 alpha + Li7	12983	-8.6646 MeV
alpha + B10 → N gamma + proton + neutron + C12	12363	-885.07 keV
triton + B10 → N gamma + neutron + C12	12087	18.929 MeV
alpha + B10 → proton + alpha + Be9	11950	-6.5856 MeV
Li7 + B11 → N gamma + neutron + O17	11387	16.312 MeV
triton + B11 → alpha + Be10	10820	8.5866 MeV
triton + B11 → neutron + C13	10534	12.421 MeV
Li7 + B10 → N gamma + neutron + alpha + C12	10112	16.462 MeV
deuteron + B10 → N gamma + proton + alpha + Li7	9070	565.14 keV
proton + B10 → N gamma + 2 alpha + He3	8497	-476.29 keV
Li8 + B11 → N gamma + 2 neutron + O17	8032	14.28 MeV
deuteron + B11 → N gamma + deuteron + B11	7883	6.9605e-06 eV
Li7 + B11 → neutron + alpha + C13	7521	9.9547 MeV
triton + B11 → 2 alpha + He6	7475	1.1736 MeV
proton + B10 → He3 + Be8	7402	-4.4714 MeV
Li7 + B10 → N gamma + proton + neutron + N15	6927	11.496 MeV
alpha + B10 → proton + neutron + 3 alpha	6829	-8.1587 MeV
He3 + B11 → He3 + B11	5752	0.0020809 eV
alpha + B11 → proton + neutron + C13	5262	-7.3929 MeV
Be9 + B11 → N gamma + neutron + alpha + N15	5207	9.4175 MeV
triton + B11 → 2 neutron + 3 alpha	5080	201.2 keV
Li7 + B10 → neutron + alpha + C12	4576	16.462 MeV
triton + B10 → alpha + Be9	4434	13.228 MeV
proton + B10 → N gamma + 2 proton + Be9	4422	-6.6218 MeV
triton + B10 → deuteron + B11	4256	5.1968 MeV
proton + B10 → alpha + Be7	4097	-3.5028 MeV
Li7 + B10 → neutron + 4 alpha	3809	9.1889 MeV
triton + B10 → proton + neutron + B11	3763	2.9724 MeV
triton + B10 → N gamma + proton + B12	3675	6.3428 MeV
Be8 + B11 → N gamma + alpha + N15	3612	11.083 MeV
triton + B10 → triton + B10	3436	-4.3675e-07 eV
alpha + B10 → 3 alpha + deuteron	3363	-5.9343 MeV
triton + B11 → N gamma + triton + B11	3260	-7.4929e-07 eV
Li7 + B11 → N gamma + triton + N15	3231	8.5241 MeV
deuteron + B11 → proton + neutron + B11	3150	-2.2244 MeV
alpha + B11 → N gamma + 2 alpha + Li7	3057	-8.6646 MeV
proton + B10 → N gamma + deuteron + B9	2648	-6.2462 MeV

Table A.6: Cont. Nuclear reactions and abundance as calculated by Geant4. Q-value based on mass balance only.

Reaction	# generated	Q-value
triton + B11 → N gamma + deuteron + B12	2515	-2.887 MeV
Li7 + B11 → neutron + deuteron + N15	2473	2.2667 MeV
Li7 + B10 → 2 alpha + Be9	2469	10.762 MeV
He3 + B11 → N gamma + deuteron + C12	2458	10.463 MeV
deuteron + B10 → He3 + Be9	2398	-1.0916 MeV
Li7 + B11 → N gamma + 2 neutron + alpha + C12	2377	5.0084 MeV
Be8 + B11 → N gamma + neutron + alpha + N14	2349	249.53 keV
alpha + B10 → He3 + B11	2264	-9.1232 MeV
proton + B10 → neutron + C10	2220	-7.3958 MeV
Li7 + B10 → N gamma + 2 neutron + O15	2166	7.9594 MeV
Li8 + B11 → N gamma + 3 neutron + O16	2103	10.137 MeV
proton + B11 → neutron + C11	1987	-2.9205 MeV
proton + B10 → N gamma + proton + neutron + B9	1936	-8.4718 MeV
deuteron + B10 → proton + 2 alpha + triton	1915	-1.9013 MeV
Be9 + B11 → neutron + alpha + N15	1771	9.4175 MeV
Li8 + B11 → N gamma + neutron + alpha + C14	1764	16.098 MeV
B10 + B11 → neutron + 2 alpha + C12	1735	7.7979 MeV
Li8 + B11 → 3 neutron + alpha + C12	1622	2.9757 MeV
Li7 + B10 → neutron + deuteron + N14	1548	2.8875 MeV
Li7 + B10 → proton + neutron + N15	1548	11.496 MeV
He3 + B10 → He3 + B10	1533	0.004057 eV
Li8 + B10 → 2 neutron + alpha + C12	1500	14.43 MeV
proton + B10 → deuteron + B9	1481	-7.0276 MeV
triton + B11 → deuteron + B12	1352	-2.887 MeV
deuteron + B10 → N gamma + neutron + alpha + Be7	1319	-1.0793 MeV
triton + B10 → N gamma + triton + B10	1316	-6.0176e-07 eV
Li7 + B11 → 2 alpha + Be10	1305	6.1201 MeV
deuteron + B11 → triton + B10	1300	-5.1968 MeV
proton + B10 → proton + deuteron + Be8	1271	-6.1366 MeV
B11 + B11 → N gamma + 2 neutron + Ne20	1190	8.2329 MeV
alpha + B10 → N gamma + 2 alpha + Li6	1181	-4.4605 MeV
Li7 + B11 → N gamma + 2 alpha + Be10	1130	6.1201 MeV
Be9 + B10 → N gamma + neutron + alpha + N14	1114	10.038 MeV
triton + B10 → 2 neutron + C11	1065	207.27 keV
B11 + B11 → N gamma + neutron + alpha + O17	1026	7.6477 MeV
Li7 + B11 → proton + 2 neutron + N15	976	42.35 keV
triton + B10 → proton + B12	963	6.3428 MeV
Li7 + B11 → N gamma + proton + neutron + N16	937	2.5315 MeV
Li7 + B11 → N gamma + alpha + C14	928	18.131 MeV

Table A.7: Cont. Nuclear reactions and abundance as calculated by Geant4. Q-value based on mass balance only.

Reaction	# generated	Q-value
Be9 + B11 → N gamma + 2 neutron + F18	897	2.9975 MeV
neutron + B10 → N gamma + B11	864	13.938 MeV
Be8 + B11 → neutron + alpha + N14	837	249.53 keV
Li8 + B10 → N gamma + 2 neutron + alpha + C12	796	14.43 MeV
Li6 + B11 → N gamma + neutron + alpha + C12	793	12.258 MeV
Li7 + B10 → 2 neutron + O15	793	7.9594 MeV
Li8 + B11 → 2 neutron + alpha + C13	755	7.922 MeV
deuteron + B10 → proton + neutron + B10	745	-2.2244 MeV
Be8 + B10 → proton + alpha + C13	706	4.1535 MeV
He3 + B10 → proton + 3 alpha	700	12.419 MeV
triton + B10 → N gamma + proton + neutron + B11	690	2.9724 MeV
Li7 + B10 → N gamma + deuteron + N15	686	13.721 MeV
Be8 + B10 → N gamma + alpha + N14	676	11.704 MeV
He3 + B11 → 3 alpha + deuteron	651	3.1889 MeV
alpha + B11 → 2 neutron + N13	642	-10.396 MeV
Li7 + B10 → alpha + deuteron + B11	628	2.7303 MeV
alpha + B11 → neutron + alpha + B10	618	-11.454 MeV
Be9 + B11 → N gamma + neutron + F19	603	13.43 MeV
Be8 + B11 → N gamma + neutron + F18	593	4.6629 MeV
triton + B10 → neutron + C12	585	18.929 MeV
Li7 + B10 → N gamma + triton + N14	563	9.1449 MeV
Li7 + B10 → proton + triton + C13	543	1.5948 MeV
Be8 + B11 → proton + alpha + C14	520	875.87 keV
Li8 + B11 → neutron + triton + N15	470	6.4915 MeV
Li8 + B11 → N gamma + 2 neutron + alpha + C13	462	7.922 MeV
B11 + B10 → neutron + 2 alpha + C12	449	7.7979 MeV
Li6 + B11 → neutron + alpha + C12	440	12.258 MeV
proton + B10 → N gamma + proton + alpha + Li6	433	-4.4961 MeV
proton + B10 → proton + neutron + B9	414	-9.0055 MeV
He3 + B11 → proton + neutron + C12	402	8.2382 MeV
alpha + B11 → neutron + deuteron + C12	391	-10.115 MeV
Li7 + B11 → N gamma + deuteron + N16	390	4.7558 MeV
triton + B10 → Li6 + Li7	387	-1.994 MeV
B11 + B11 → N gamma + neutron + Ne21	382	14.994 MeV
He3 + B11 → N gamma + alpha + B10	368	9.1232 MeV
proton + B10 → 2 alpha + He3	363	-490.11 keV
Li7 + B10 → proton + deuteron + C14	360	3.5139 MeV
deuteron + B11 → N gamma + triton + B10	357	-5.1968 MeV
gamma + B11 → N gamma + B11	355	-36.175 keV

Table A.8: Cont. Nuclear reactions and abundance as calculated by Geant4. Q-value based on mass balance only.

Reaction	# generated	Q-value
He3 + B10 → N gamma + deuteron + C11	349	3.195 MeV
Li8 + B11 → neutron + alpha + C14	342	16.098 MeV
B10 + B11 → N gamma + neutron + alpha + O16	329	14.959 MeV
Li7 + B11 → proton + triton + C14	326	-1.6829 MeV
proton + B11 → N gamma + deuteron + B10	318	-9.2667 MeV
He3 + B11 → N gamma + proton + neutron + C12	313	8.2382 MeV
Be9 + B10 → 2 alpha + B11	296	9.8811 MeV
alpha + B11 → N gamma + neutron + alpha + B10	296	-11.454 MeV
deuteron + B10 → 2 Li6	287	-2.9866 MeV
He3 + B11 → proton + alpha + Be9	286	2.5376 MeV
Li7 + B11 → neutron + triton + N14	280	-2.3092 MeV
Li8 + B10 → N gamma + neutron + alpha + C13	265	19.376 MeV
He3 + B11 → alpha + B10	264	9.1232 MeV
Be9 + B10 → neutron + alpha + N14	261	10.038 MeV
Li7 + B10 → N gamma + neutron + deuteron + N14	261	2.8875 MeV
neutron + B11 → N gamma + B12	258	3.2506 MeV
Li6 + B11 → N gamma + proton + neutron + N15	248	7.2923 MeV
Be9 + B11 → N gamma + C13 + Li7	247	1.9823 MeV
He3 + B11 → proton + neutron + 3 alpha	228	964.55 keV
Li8 + B11 → N gamma + neutron + triton + N15	228	6.4915 MeV
proton + B10 → N gamma + 2 proton + neutron + Be8	228	-8.2821 MeV
Li8 + B10 → proton + 2 neutron + N15	224	9.4639 MeV
He3 + B11 → N gamma + proton + C13	220	13.184 MeV
B10 + B11 → N gamma + proton + neutron + F19	215	6.8443 MeV
Li7 + B10 → N gamma + proton + alpha + B12	213	3.8763 MeV
Be9 + B11 → N gamma + alpha + N16	210	11.907 MeV
proton + B10 → proton +	207	-2.0376e-07 eV
deuteron + B11 → 2 neutron + C11	206	-4.9895 MeV
Li8 + B11 → N gamma + neutron + O18	204	22.324 MeV
alpha + B11 → N gamma + proton + neutron + C13	204	-7.3929 MeV
He3 + B11 → 2 alpha + Li6	198	4.6628 MeV
triton + B10 → He3 + Be10	187	-536.66 keV
Be9 + B11 → N gamma + proton + O19	185	9.3907 MeV
proton + B11 → N gamma + proton + neutron + B10	185	-11.489 MeV
Li7 + B11 → N gamma + proton + N17	181	8.4151 MeV
Li8 + B10 → N gamma + 2 alpha + Be10	180	15.542 MeV
Be9 + B11 → N gamma + Li6 + C14	179	2.9087 MeV
Li7 + B11 → N gamma + neutron + deuteron + N15	179	2.2667 MeV
B10 + B10 → N gamma + proton + alpha + N15	177	14.286 MeV
Li8 + B10 → N gamma + neutron + deuteron + N15	177	11.688 MeV

Table A.9: Cont. Nuclear reactions and abundance as calculated by Geant4. Q-value based on mass balance only.

Reaction	# generated	Q-value
Be8 + B10 → N gamma + proton + O17	171	10.511 MeV
Be9 + B10 → N gamma + alpha + N15	168	20.872 MeV
Li8 + B10 → neutron + 2 alpha + Be9	163	8.7293 MeV
B10 + B10 → N gamma + 2 alpha + C12	159	19.252 MeV
He6 + B11 → N gamma + 2 neutron + N15	159	10.018 MeV
Li8 + B11 → N gamma + proton + neutron + N17	155	6.3825 MeV
Li6 + B11 → 2 alpha + Be9	153	6.5578 MeV
Li7 + B11 → N gamma + He6 + C12	148	5.9807 MeV
B10 + B11 → N gamma + alpha + O17	140	19.102 MeV
Li6 + B11 → neutron + 4 alpha	138	4.9847 MeV
Li6 + B11 → proton + neutron + N15	138	7.2923 MeV
triton + B10 → N gamma + 2 neutron + C11	137	207.27 keV
Be8 + B10 → N gamma + proton + neutron + O16	129	6.3681 MeV
triton + B11 → neutron + deuteron + B11	128	-6.2574 MeV
triton + B10 → N gamma + Li6 + Li7	127	-1.994 MeV
Be9 + B10 → N gamma + 2 alpha + B11	125	9.8811 MeV
Be9 + B10 → proton + alpha + C14	124	10.665 MeV
proton + B10 → C11	123	-1.2338 MeV
Li7 + B10 → proton + alpha + B12	122	3.8763 MeV
B11 + B11 → N gamma + proton + neutron + F20	121	1.9915 MeV
deuteron + B11 → N gamma + proton + neutron + B11	121	-2.2244 MeV
Li7 + B10 → N gamma + alpha + C13	120	21.409 MeV
triton + B10 → alpha + deuteron + Li7	120	-3.4678 MeV
Li8 + B11 → neutron + He6 + C12	117	3.9481 MeV
B11 + B11 → N gamma + 2 neutron + alpha + O16	115	3.5046 MeV
He3 + B10 → N gamma + proton + C12	114	19.692 MeV
Li7 + B10 → neutron + He3 + C13	114	831.45 keV
Be10 + B11 → N gamma + 2 neutron + F19	112	6.6176 MeV
Be9 + B10 → N gamma + proton + neutron + O17	112	8.8459 MeV
He3 + B10 → deuteron + C11	112	3.195 MeV
Be8 + B10 → neutron + alpha + N13	102	1.1503 MeV
Li6 + B10 → N gamma + proton + alpha + B11	101	7.7559 MeV
B11 + B10 → N gamma + neutron + alpha + O16	97	14.959 MeV
deuteron + B10 → neutron + 2 alpha + He3	97	-2.6647 MeV
B10 + B11 → N gamma + neutron + 2 alpha + C12	94	7.7979 MeV
deuteron + B10 → N gamma + proton + neutron + B10	92	-2.2244 MeV
B10 + B10 → 2 alpha + C12	88	19.252 MeV
Li8 + B10 → alpha + triton + B11	88	6.955 MeV
Li7 + B10 → neutron + triton + N13	87	-1.4085 MeV

Table A.10: Cont. Nuclear reactions and abundance as calculated by Geant4. Q-value based on mass balance only.

Reaction	# generated	Q-value
Li8 + B10 → N gamma + proton + 2 neutron + N15	85	9.4639 MeV
Li8 + B11 → N gamma + C13 + He6	82	8.8944 MeV
B11 + B11 → N gamma + alpha + O18	80	15.692 MeV
Li8 + B10 → neutron + alpha + C13	77	19.376 MeV
Be8 + B10 → alpha + deuteron + C12	75	1.4316 MeV
Li8 + B11 → N gamma + neutron + deuteron + N16	75	2.7232 MeV
Be9 + B11 → N gamma + 2 neutron + alpha + N14	73	-1.4158 MeV
Be9 + B11 → N gamma + triton + O17	71	5.8735 MeV
Li6 + B10 → N gamma + deuteron + N14	71	10.138 MeV
Li6 + B10 → N gamma + neutron + alpha + C11	70	4.9908 MeV
Li8 + B10 → neutron + triton + N14	69	7.1123 MeV
Li6 + B11 → 2 neutron + O15	68	3.7553 MeV
proton + B10 → 2 proton + Be9	66	-7.0094 MeV
alpha + B10 → triton + C11	65	-11.125 MeV
alpha + B11 → 3 alpha + triton	65	-11.131 MeV
Be9 + B10 → alpha + triton + C12	64	6.0236 MeV
Be9 + B10 → N gamma + deuteron + O17	62	11.07 MeV
Li8 + B11 → N gamma + proton + N18	61	9.2107 MeV
Li6 + B11 → N gamma + deuteron + N15	60	9.5167 MeV
Li8 + B10 → neutron + deuteron + N15	60	11.688 MeV
proton + B10 → N gamma + C11	60	8.6524 MeV
B10 + B10 → N gamma + alpha + deuteron + N14	57	5.6771 MeV
B10 + B11 → N gamma + proton + F20	57	13.446 MeV
alpha + B11 → N gamma + neutron + deuteron + C12	57	-10.115 MeV
Be8 + B11 → N gamma + proton + O18	56	7.1011 MeV
Li8 + B10 → 2 neutron + 4 alpha	55	7.1562 MeV
deuteron + B11 → Li6 + Li7	55	-7.1908 MeV
B11 + B11 → N gamma + deuteron + F20	53	4.2159 MeV
He6 + B11 → 2 neutron + N15	53	10.018 MeV
Li8 + B10 → N gamma + 2 neutron + O16	53	21.591 MeV
B10 + B11 → proton + neutron + alpha + N15	52	2.8319 MeV
B10 + B10 → N gamma + neutron + alpha + O15	51	10.749 MeV
Li6 + B10 → proton + alpha + B11	51	7.7559 MeV
Li8 + B10 → N gamma + neutron + triton + N14	50	7.1123 MeV
B11 + B10 → N gamma + proton + neutron + F19	49	6.8443 MeV
alpha + B11 → proton + alpha + Be10	49	-11.227 MeV
proton + B10 → 2 proton + neutron + Be8	49	-8.2978 MeV
proton + B11 → proton + neutron + B10	49	-11.499 MeV
triton + B10 → N gamma + He3 + Be10	49	-536.66 keV

Table A.11: Cont. Nuclear reactions and abundance as calculated by Geant4. Q-value based on mass balance only.

Reaction	# generated	Q-value
alpha + B11 → Li6 + Be9	48	-14.342 MeV
deuteron + B11 → He3 + Be10	48	-5.7334 MeV
gamma + B10 → N gamma + B10	48	-39.393 keV
Be8 + B10 → proton + neutron + alpha + C12	47	-792.77 keV
triton + B11 → 2 Li7	47	-6.1982 MeV
Li6 + B11 → N gamma + 2 neutron + O15	46	3.7553 MeV
He3 + B11 → deuteron + C12	44	10.463 MeV
Li8 + B10 → 3 neutron + O15	44	5.9268 MeV
B10 + B11 → N gamma + 2 alpha + C13	43	12.744 MeV
Li7 + B10 → proton + neutron + alpha + B11	43	505.94 keV
Li8 + B11 → neutron + 2 alpha + Be10	43	4.0875 MeV
Li8 + B10 → N gamma + triton + N15	42	17.946 MeV
Li6 + B11 → N gamma + triton + N14	41	4.9408 MeV
B10 + B11 → N gamma + alpha + deuteron + N15	40	5.0562 MeV
B10 + B11 → N gamma + proton + alpha + N16	40	5.321 MeV
Li6 + B10 → 4 alpha	40	16.439 MeV
Li6 + B10 → N gamma + proton + N15	40	18.746 MeV
He3 + B10 → 2 proton + B11	38	3.7357 MeV
Li7 + B11 → 3 alpha + He6	38	-1.2929 MeV
He3 + B11 → proton + C13	37	13.184 MeV
Li8 + B10 → 2 alpha + Be10	37	15.542 MeV
alpha + B10 → N gamma + He3 + B11	36	-9.1232 MeV
Be10 + B11 → N gamma + neutron + alpha + N16	34	5.0943 MeV
Li6 + B10 → neutron + alpha + C11	34	4.9908 MeV
Li6 + B11 → neutron + deuteron + N14	34	-1.3166 MeV
Li8 + B11 → N gamma + triton + N16	34	8.9806 MeV
Be9 + B10 → proton + neutron + alpha + C13	33	2.4882 MeV
C12 + B11 → N gamma + neutron + alpha + F18	33	-2.703 MeV
Be8 + B11 → 2 alpha + B11	32	92.297 keV
Li8 + B10 → N gamma + neutron + O17	32	25.734 MeV
Li8 + B11 → N gamma + deuteron + N17	32	8.6068 MeV
B10 + B11 → N gamma + Li6 + N15	31	6.5301 MeV
Be7 + B11 → proton + alpha + C13	31	11.599 MeV
Li7 + B11 → 3 neutron + O15	31	-3.4947 MeV
Be8 + B10 → N gamma + neutron + F17	30	6.9677 MeV
Be8 + B10 → N gamma + proton + alpha + C13	30	4.1535 MeV
Li7 + B10 → N gamma + alpha + deuteron + B11	30	2.7303 MeV
triton + B11 → N gamma + proton + B13	30	-233.3 keV
B10 + B10 → N gamma + proton + neutron + alpha + N14	29	3.4527 MeV

Table A.12: Cont. Nuclear reactions and abundance as calculated by Geant4. Q-value based on mass balance only.

Reaction	# generated	Q-value
B10 + B11 → N gamma + deuteron + F19	29	9.0687 MeV
B11 + B10 → N gamma + alpha + O17	29	19.102 MeV
Be7 + B11 → proton + neutron + alpha + C12	28	6.6528 MeV
Li6 + B10 → N gamma + He3 + C13	28	8.0814 MeV
B10 + B10 → 5 alpha	27	11.978 MeV
B10 + B10 → N gamma + proton + neutron + F18	27	7.866 MeV
B10 + B10 → proton + alpha + N15	27	14.286 MeV
Be9 + B11 → N gamma + proton + neutron + O18	27	5.4358 MeV
Li7 + B10 → proton + 2 neutron + N14	27	663.17 keV
C12 + B11 → N gamma + neutron + Na22	25	5.7763 MeV
alpha + B10 → N gamma + triton + C11	25	-11.125 MeV
B11 + B11 → 2 neutron + 2 alpha + C12	24	-3.6563 MeV
Li6 + B10 → N gamma + proton + neutron + N14	24	7.9132 MeV
Li8 + B10 → proton + triton + C14	24	7.7386 MeV
Be9 + B10 → N gamma + neutron + deuteron + O16	23	6.9271 MeV
neutron + B11 → N gamma + neutron + triton + Be8	23	-11.256 MeV
triton + B11 → proton + neutron + B12	23	-5.1114 MeV
Be7 + B11 → N gamma + proton + alpha + C13	22	11.599 MeV
He3 + B10 → proton + neutron + C11	22	970.62 keV
He3 + B11 → triton + C11	22	-2.0018 MeV
Li6 + B10 → N gamma + neutron + O15	22	15.209 MeV
B10 + B10 → neutron + alpha + O15	21	10.749 MeV
B10 + B10 → proton + neutron + alpha + N14	21	3.4527 MeV
Be10 + B11 → N gamma + neutron + F20	21	13.219 MeV
He3 + B10 → N gamma + He3 + B10	21	0.011747 eV
He3 + B11 → N gamma + 2 alpha + Li6	21	4.6628 MeV
proton + B11 → deuteron + B10	21	-9.2926 MeV
B10 + B11 → N gamma + N14 + Li7	20	2.9467 MeV
He3 + B11 → neutron + N13	20	10.181 MeV
triton + B11 → N gamma + proton + neutron + B12	20	-5.1114 MeV
Be7 + B11 → N gamma + alpha + N14	19	19.149 MeV
Li7 + B10 → N gamma + neutron + O16	19	23.623 MeV
Li7 + B11 → neutron + 2 alpha + Be9	19	-692.2 keV
Li8 + B10 → 3 alpha + He6	19	8.1286 MeV
Li8 + B10 → N gamma + alpha + triton + B11	19	6.955 MeV
triton + B11 → N gamma + 2 Li7	19	-6.1982 MeV
Li8 + B11 → 2 neutron + deuteron + N15	18	234.09 keV
deuteron + B10 → alpha + deuteron + Li6	18	-4.4605 MeV
neutron + B10 → N gamma + proton + 2 neutron + Be8	18	-8.2792 MeV
proton + B11 → N gamma + proton + triton + Be8	18	-11.256 MeV

Table A.13: Cont. Nuclear reactions and abundance as calculated by Geant4. Q-value based on mass balance only.

Reaction	# generated	Q-value
B10 + B11 → N gamma + neutron + Ne20	17	19.687 MeV
Be9 + B10 → N gamma + proton + alpha + C14	17	10.665 MeV
triton + B10 → proton + alpha + Li8	17	-3.6596 MeV
Li7 + B10 → deuteron + triton + C12	16	-1.1272 MeV
Li8 + B10 → N gamma + 3 neutron + O15	16	5.9268 MeV
Li8 + B11 → N gamma + proton + 2 neutron + N16	16	498.83 keV
B11 + B10 → N gamma + neutron + 2 alpha + C12	15	7.7979 MeV
Be7 + B11 → 2 alpha + B10	15	7.5379 MeV
Be9 + B10 → N gamma + neutron + F18	15	14.452 MeV
Be9 + B11 → N gamma + deuteron + O18	15	7.6602 MeV
alpha + B11 → N gamma + proton + alpha + Be10	15	-11.227 MeV
deuteron + B11 → N gamma + 2 neutron + C11	15	-4.9895 MeV
Li8 + B10 → N gamma + proton + neutron + N16	14	11.953 MeV
proton + B11 → N gamma + 2 proton + Be10	14	-11.265 MeV
B10 + B10 → alpha + deuteron + N14	13	5.6771 MeV
B11 + B10 → N gamma + proton + alpha + N16	13	5.321 MeV
Be10 + B10 → N gamma + neutron + alpha + N15	13	14.059 MeV
Be7 + B11 → alpha + deuteron + C12	13	8.8772 MeV
Be9 + B10 → alpha + deuteron + C13	13	4.7126 MeV
He6 + B10 → N gamma + neutron + alpha + B11	13	10.482 MeV
Li6 + B11 → N gamma + alpha + C13	13	17.205 MeV
Li8 + B10 → N gamma + alpha + deuteron + B12	13	4.068 MeV
deuteron + B11 → N gamma + Li6 + Li7	13	-7.1908 MeV
Be10 + B11 → 2 neutron + alpha + N15	12	2.6052 MeV
He3 + B10 → proton + C12	12	19.692 MeV
Li6 + B10 → proton + neutron + N14	12	7.9132 MeV
Li7 + B10 → N gamma + proton + N16	12	13.986 MeV
B11 + B10 → N gamma + proton + F20	11	13.446 MeV
Be7 + B10 → proton + 4 alpha	11	10.833 MeV
Be8 + B11 → N gamma + deuteron + O17	11	1.2815 MeV
C12 + B10 → N gamma + 2 alpha + N14	11	4.3378 MeV
Li8 + B10 → N gamma + Li7 + B11	11	9.4215 MeV
alpha + B11 → alpha + deuteron + Be9	11	-15.815 MeV
neutron + B10 → N gamma + neutron + deuteron + Be8	11	-6.0611 MeV
B10 + B11 → N gamma + alpha + triton + N14	10	480.29 keV
B11 + B10 → N gamma + Li6 + N15	10	6.5301 MeV
B11 + B11 → N gamma + proton + F21	10	10.093 MeV
Li6 + B10 → Li6 + B10	10	-5.457e-07 eV
Li6 + B10 → N gamma + alpha + C12	10	23.712 MeV
Li6 + B11 → proton + triton + C13	10	-2.6094 MeV

Table A.14: Cont. Nuclear reactions and abundance as calculated by Geant4. Q-value based on mass balance only.

Reaction	# generated	Q-value
Li7 + B10 → N gamma + proton + triton + C13	10	1.5948 MeV
Li8 + B10 → 2 neutron + deuteron + N14	10	854.92 keV
triton + B10 → N gamma + alpha + deuteron + Li7	10	-3.4678 MeV
B11 + B10 → N gamma + 2 alpha + C13	9	12.744 MeV
B11 + B10 → proton + neutron + alpha + N15	9	2.8319 MeV
Be9 + B11 → N gamma + N14 + He6	9	-443.46 keV
Li7 + B10 → N gamma + Li6 + B11	9	4.2041 MeV
Li7 + B11 → alpha + triton + B11	9	-2.4665 MeV
deuteron + B10 → 2 proton + Be10	9	-1.9977 MeV
gamma + B10 → N gamma + deuteron + Be8	9	-6.0762 MeV
B10 + B11 → N gamma + proton + neutron + alpha + N15	8	2.8319 MeV
B10 + B11 → N gamma + triton + F18	8	4.8936 MeV
Be7 + B10 → N gamma + proton + alpha + C12	8	18.107 MeV
Be7 + B11 → N gamma + 2 alpha + B10	8	7.5379 MeV
neutron + B10 → N gamma + neutron + 2 alpha + deuteron	8	-5.9777 MeV
B11 + B10 → N gamma + neutron + Ne20	7	19.687 MeV
B11 + B11 → N gamma + triton + F19	7	3.8719 MeV
Be7 + B10 → N gamma + proton + neutron + O15	7	9.6038 MeV
Be9 + B10 → N gamma + 2 neutron + F17	7	5.3023 MeV
Be9 + B10 → neutron + alpha + deuteron + C12	7	-233.75 keV
C12 + B10 → N gamma + proton + neutron + Ne20	7	3.7305 MeV
C12 + B11 → N gamma + proton + Ne22	7	9.4018 MeV
He3 + B10 → N gamma + 2 proton + B11	7	3.7357 MeV
He6 + B11 → N gamma + neutron + alpha + B12	7	2.398 MeV
Li6 + B10 → proton + 2 alpha + Li7	7	-908.7 keV
gamma + B10 → N gamma + proton + Be9	7	-6.6113 MeV
neutron + B10 → N gamma + proton + neutron + Be9	7	-6.6223 MeV
neutron + B11 → 2 neutron + B10	7	-13.567 MeV
neutron + B11 → N gamma + deuteron + Be10	7	-9.0501 MeV
neutron + B11 → N gamma + neutron + deuteron + Be9	7	-15.859 MeV
B10 + B10 → N gamma + He3 + O17	6	9.9786 MeV
Be7 + B11 → N gamma + alpha + deuteron + C12	6	8.8772 MeV
Be8 + B10 → N gamma + deuteron + O16	6	8.5925 MeV
Be9 + B10 → N gamma + proton + O18	6	16.89 MeV
C12 + B11 → N gamma + alpha + F19	6	7.7294 MeV
C13 + B11 → N gamma + 2 neutron + Na22	6	829.98 keV
He6 + B10 → neutron + alpha + B11	6	10.482 MeV
Li6 + B10 → Be7 + Be9	6	-980.08 keV
Li6 + B10 → deuteron + N14	6	10.138 MeV
Li6 + B10 → neutron + He3 + C12	6	3.1351 MeV

Table A.15: Cont. Nuclear reactions and abundance as calculated by Geant4. Q-value based on mass balance only.

Reaction	# generated	Q-value
Li6 + B11 → proton + deuteron + C14	6	-690.27 keV
Li8 + B10 → N gamma + deuteron + N16	6	14.177 MeV
neutron + B11 → N gamma + neutron + 2 alpha + triton	6	-11.16 MeV
proton + B11 → N gamma + triton + B9	6	-11.446 MeV
B10 + B11 → 2 neutron + alpha + O15	5	-705.22 keV
B10 + B11 → N gamma + 2 neutron + Ne19	5	2.8224 MeV
B11 + B10 → N gamma + N14 + Li7	5	2.9467 MeV
B11 + B10 → N gamma + deuteron + F19	5	9.0687 MeV
B11 + B11 → N gamma + He6 + O16	5	4.477 MeV
Be7 + B10 → N gamma + 2 proton + N15	5	13.141 MeV
Be7 + B11 → neutron + alpha + N13	5	8.5958 MeV
Be8 + B10 → 2 alpha + B10	5	92.297 keV
He6 + B10 → N gamma + 2 neutron + N14	5	10.639 MeV
He6 + B10 → N gamma + neutron + N15	5	21.472 MeV
He6 + B11 → neutron + alpha + B12	5	2.398 MeV
Li6 + B10 → He3 + C13	5	8.0814 MeV
Li6 + B10 → N gamma + 2 proton + C14	5	8.5395 MeV
Li6 + B10 → N gamma + Li6 + B10	5	1.0743e-06 eV
Li6 + B10 → proton + triton + C12	5	3.8985 MeV
Li6 + B11 → alpha + deuteron + B11	5	-1.4738 MeV
Li7 + B10 → 2 neutron + alpha + C11	5	-2.2592 MeV
Li7 + B10 → 2 proton + neutron + C14	5	1.2895 MeV
Li8 + B10 → deuteron + triton + C13	5	1.7865 MeV
Li8 + B10 → proton + neutron + deuteron + C14	5	1.4813 MeV
alpha + B11 → proton + 2 neutron + C12	5	-12.339 MeV
deuteron + B10 → N gamma + 2 Li6	5	-2.9866 MeV
gamma + B10 → B10	5	-7.3553 MeV
neutron + B10 → proton + 2 neutron + Be8	5	-10.052 MeV
triton + B11 → N gamma + neutron + deuteron + B11	5	-6.2574 MeV
B11 + B10 → N gamma + alpha + deuteron + N15	4	5.0562 MeV
Be9 + B11 → 2 alpha + B12	4	1.7973 MeV
C12 + B11 → N gamma + proton + neutron + Ne21	4	-962.43 keV
Li6 + B10 → alpha + C12	4	23.712 MeV
Li7 + B10 → N gamma + He3 + C14	4	9.0079 MeV
Li8 + B10 → 2 deuteron + C14	4	3.7056 MeV
Li8 + B10 → alpha + deuteron + B12	4	4.068 MeV
alpha + B10 → N gamma + Be7 + Li7	4	-16.202 MeV
deuteron + B11 → N gamma + He3 + Be10	4	-5.7334 MeV
neutron + B11 → neutron + triton + Be8	4	-15.574 MeV

Table A.16: Cont. Nuclear reactions and abundance as calculated by Geant4. Q-value based on mass balance only.

Reaction	# generated	Q-value
proton + B10 → proton + alpha + Li6	4	-5.1034 MeV
proton + B11 → N gamma + proton + alpha + Li7	4	-8.693 MeV
B10 + B10 → N gamma + proton + triton + O16	3	6.5988 MeV
B10 + B11 → N gamma + neutron + deuteron + F18	3	-1.3637 MeV
B11 + B11 → N gamma + 2 alpha + C14	3	9.4665 MeV
Be10 + B10 → N gamma + 2 neutron + F18	3	7.6394 MeV
Be10 + B10 → N gamma + 2 neutron + alpha + N14	3	3.226 MeV
Be10 + B10 → neutron + alpha + N15	3	14.059 MeV
Be7 + B10 → proton + alpha + C12	3	18.107 MeV
Be9 + B11 → N gamma + 2 alpha + B12	3	1.7973 MeV
Be9 + B11 → proton + neutron + alpha + C14	3	-789.49 keV
C14 + B11 → N gamma + 2 neutron + Na23	3	5.0723 MeV
He3 + B10 → N gamma + proton + neutron + C11	3	970.62 keV
He6 + B10 → N gamma + deuteron + C14	3	13.49 MeV
Li6 + B10 → N gamma + neutron + He3 + C12	3	3.1351 MeV
Li6 + B10 → N gamma + proton + deuteron + C13	3	2.5874 MeV
Li6 + B10 → triton + N13	3	5.8415 MeV
Li8 + B10 → N gamma + alpha + C14	3	27.553 MeV
alpha + B11 → He3 + B12	3	-17.207 MeV
alpha + B11 → N gamma + He3 + B12	3	-17.207 MeV
alpha + B11 → neutron + 2 alpha + Li6	3	-15.915 MeV
deuteron + B10 → 2 neutron + C10	3	-6.655 MeV
gamma + B10 → deuteron + Be8	3	-6.0916 MeV
neutron + B11 → N gamma + proton + 2 neutron + Be9	3	-18.074 MeV
B10 + B10 → 2 proton + alpha + C14	2	4.079 MeV
B10 + B10 → N gamma + alpha + O16	2	26.413 MeV
B10 + B10 → N gamma + deuteron + F18	2	10.09 MeV
B10 + B10 → N gamma + proton + F19	2	18.298 MeV
B11 + B10 → N gamma + 2 neutron + Ne19	2	2.8224 MeV
B11 + B10 → N gamma + alpha + triton + N14	2	480.29 keV
B11 + B10 → N gamma + triton + F18	2	4.8936 MeV
Be10 + B10 → 2 neutron + alpha + N14	2	3.226 MeV
Be10 + B10 → N gamma + C13 + Li7	2	6.6241 MeV
Be10 + B10 → neutron + 2 alpha + B11	2	3.0688 MeV
Be10 + B11 → N gamma + alpha + N17	2	10.978 MeV
Be7 + B10 → proton + deuteron + N14	2	4.532 MeV
Be7 + B11 → N gamma + deuteron + O16	2	16.038 MeV
Be7 + B11 → N gamma + proton + O17	2	17.957 MeV
Be7 + B11 → N gamma + proton + neutron + O16	2	13.814 MeV

Table A.17: Cont. Nuclear reactions and abundance as calculated by Geant4. Q-value based on mass balance only.

Reaction	# generated	Q-value
Be8 + B10 → N gamma + 2 alpha + B10	2	92.297 keV
Be9 + B10 → N gamma + alpha + deuteron + C13	2	4.7126 MeV
Be9 + B10 → N gamma + triton + O16	2	13.184 MeV
C12 + B10 → N gamma + alpha + F18	2	8.7511 MeV
C12 + B10 → N gamma + proton + Ne21	2	10.492 MeV
C13 + B11 → N gamma + neutron + Na23	2	13.249 MeV
He3 + B10 → Be7 + Li6	2	-2.8751 MeV
He3 + B10 → N gamma + Be7 + Li6	2	-2.8751 MeV
He3 + B11 → N gamma + He3 + B11	2	0.023629 eV
He6 + B10 → N gamma + alpha + B12	2	13.852 MeV
He6 + B10 → N gamma + proton + neutron + C14	2	11.265 MeV
He6 + B11 → N gamma + neutron + N16	2	12.507 MeV
He6 + B11 → neutron + deuteron + C14	2	2.0356 MeV
Li6 + B10 → 2 proton + C14	2	8.5395 MeV
Li6 + B10 → N gamma + proton + 2 alpha + Li7	2	-908.7 keV
Li6 + B10 → proton + N15	2	18.746 MeV
Li6 + B11 → N gamma + neutron + O16	2	19.419 MeV
Li6 + B11 → N gamma + proton + alpha + B12	2	-327.85 keV
Li7 + B10 → N gamma + neutron + He3 + C13	2	831.45 keV
Li7 + B10 → N gamma + proton + deuteron + C14	2	3.5139 MeV
Li7 + B11 → N gamma + O18	2	24.356 MeV
Li7 + B11 → N gamma + neutron + triton + N14	2	-2.3092 MeV
Li8 + B10 → 2 triton + C12	2	3.0976 MeV
Li8 + B10 → N gamma + He6 + C12	2	15.402 MeV
Li8 + B10 → N gamma + proton + N17	2	17.837 MeV
Li8 + B10 → N gamma + proton + triton + C14	2	7.7386 MeV
alpha + B10 → proton + deuteron + B11	2	-14.617 MeV
alpha + B11 → N gamma + proton + 2 neutron + C12	2	-12.339 MeV
deuteron + B11 → N gamma + Be7 + He6	2	-11.561 MeV
deuteron + B11 → alpha + deuteron + Li7	2	-8.6646 MeV
deuteron + B11 → alpha + triton + Li6	2	-9.6572 MeV
gamma + B10 → N gamma + neutron + B9	2	-8.4649 MeV
neutron + B10 → N gamma + 2 neutron + B9	2	-8.4592 MeV
neutron + B10 → N gamma + proton + 2 neutron + 2 alpha	2	-8.1944 MeV
neutron + B10 → N gamma + proton + alpha + He6	2	-7.2146 MeV
neutron + B10 → neutron + deuteron + Be8	2	-10.523 MeV
neutron + B11 → neutron + 2 alpha + triton	2	-11.184 MeV
neutron + B11 → neutron + alpha + Li7	2	-8.5133 MeV
proton + B11 → N gamma + He3 + Be9	2	-10.355 MeV

Table A.18: Cont. Nuclear reactions and abundance as calculated by Geant4. Q-value based on mass balance only.

Reaction	# generated	Q-value
triton + B10 → 2 alpha + deuteron + triton	2	-5.9343 MeV
triton + B10 → Be7 + He6	2	-6.3643 MeV
triton + B10 → neutron + deuteron + B10	2	-6.2574 MeV
triton + B10 → proton + neutron + alpha + Li7	2	-5.6922 MeV
B10 + B10 → N gamma + neutron + He3 + O16	1	5.8355 MeV
B10 + B10 → N gamma + neutron + Ne19	1	14.276 MeV
B10 + B10 → N gamma + proton + deuteron + O17	1	4.4846 MeV
B10 + B10 → alpha + He3 + C13	1	3.621 MeV
B10 + B10 → alpha + triton + N13	1	1.381 MeV
B10 + B10 → neutron + 2 alpha + C11	1	530.32 keV
B10 + B10 → neutron + alpha + He3 + C12	1	-1.3254 MeV
B10 + B10 → proton + 2 alpha + B11	1	3.2955 MeV
B10 + B11 → N gamma + He3 + O18	1	6.5685 MeV
B11 + B10 → N gamma + proton + neutron + alpha + N15	1	2.8319 MeV
B11 + B11 → alpha + He6 + C12	1	-2.6839 MeV
Be10 + B10 → N gamma + C12 + Li8	1	3.7104 MeV
Be10 + B10 → N gamma + Li6 + C14	1	7.5505 MeV
Be10 + B10 → N gamma + N14 + He6	1	4.1984 MeV
Be10 + B10 → N gamma + neutron + F19	1	18.072 MeV
Be10 + B10 → N gamma + proton + neutron + O18	1	10.078 MeV
Be10 + B10 → neutron + Li7 + C12	1	1.6778 MeV
Be10 + B10 → neutron + alpha + triton + C12	1	-788.7 keV
Be7 + B10 → N gamma + deuteron + O15	1	11.828 MeV
Be7 + B10 → alpha + deuteron + C11	1	1.6096 MeV
Be7 + B10 → proton + He3 + C13	1	2.4759 MeV
Be7 + B11 → 2 proton + neutron + N15	1	1.6868 MeV
Be7 + B11 → N gamma + He3 + N15	1	9.4052 MeV
Be7 + B11 → N gamma + neutron + F17	1	14.413 MeV
Be7 + B11 → proton + deuteron + N15	1	3.9112 MeV
Be8 + B11 → N gamma + triton + O16	1	3.3957 MeV
Be9 + B10 → 2 neutron + alpha + N13	1	-515.09 keV
Be9 + B10 → 3 alpha + Li7	1	1.2165 MeV
Be9 + B10 → N gamma + He3 + N16	1	2.7834 MeV
Be9 + B10 → N gamma + alpha + triton + C12	1	6.0236 MeV
Be9 + B10 → N gamma + proton + 2 neutron + O16	1	4.7027 MeV
Be9 + B11 → 2 neutron + alpha + N14	1	-1.4158 MeV
Be9 + B11 → alpha + deuteron + C14	1	1.4349 MeV
Be9 + B11 → alpha + triton + C13	1	-484.21 keV
C12 + B10 → N gamma + neutron + Na21	1	6.1608 MeV

APPENDIX B

LIST POTENTIAL GAMMA RAYS AND STATES

Search parameters:
6495 <=E(γ1)<= 6510

Level and Gamma Information

More detailed information can be obtained by clicking on each NUCLEAR NAME

Nucleus	E_{level}(keV)	Jπ	$T_{1/2}$	E_γ(keV)	I_γ	γ mult.	γ mix. ratio	γ conv. coeff.
15O	11748 *3*	5/2+	99 keV *5*	6505 *3*	89 *13*	[M1]		
19F	6496.7 *14*	3/2+		6496.7	38 *2*	M1		
22NA	8436 *2*	(1 TO 3)-	5.4 keV *15*	6498	3			
23NA	6947.40 *6*	(3/2)+	< 28 fs	6506.41 *16*	61 *10*			
23NA	9487.75 *22*	3/2		6504.7 *8*	6.9			
23NA	10346.11 *19*	5/2+	8 eV	6497.0 *7*	2.4			
23NA	10353.84 *18*	3/2+	210 eV	6504.7 *7*	88			
29SI	6496.23 *21*	1/2+ TO 5/2+	< 24 fs	6496	80 *8*			
30SI	8734 *3*	(0+ TO 3+)		6498	47 *12*			
30SI	11783.7 *24*	(4,5+)	< 35 fs	6502	20 *4*			
30P	7178 *3*	1-	15 keV	6502.0 *5*	23.2 *17*	D		
30P	7207.5 *5*	(0+)	50 eV	6498.8 *6*	8.1 *13*			
31P	6496.1 *13*	3/2-		6496.1	100 *7*			
31P	8729.1 *9*	3/2		6495.3	7.5	D+Q	-0.20 *7*	
31P	8730.5 *9*	3/2(+)		6496.7	14.9	D+Q	-0.01 *13*	
31P	8738.0 *9*	3/2+	20 eV *5*	6504.2	22.2	D+Q	-0.8 *4*	
31P	9925 *1*	3/2		6509	38.5			
32P	6581.93 *6*	(0+ TO 3+)		6503.16 *7*	100 *5*			
32S	10778.8 *10*	2+	0.62 keV *7*	6496.2	38.9 *7*			
32S	10783.8 *10*		0.75 keV *8*	6501.2	7.2 *4*			
32S	10791.3 *10*	1	0.17 keV *2*	6508.7	15.4 *9*			
34S	9801.89 *10*	(1,2+)		6496.62 *23*	100 *13*			
35CL	8269.6 *4*	5/2+	0.005 keV *3*	6505.8	19 *10*			
37CL	10207.8 *4*	3/2		6499.4	46	D(+Q)	-0.009 *12*	
37CL	10212.4 *4*			6504.0	17			
37CL	10217.7 *4*			6509.3	63			
36AR	8472.0 *10*	(3-,4-,5-)	30 fs *7*	6501.0	<3.1			
36AR	10675.9 *10*	5		6497.0	<5			
38AR	6495.8 *3*	(2-,3,4+)	11 fs *4*	6495.2	<7			
38AR	8668 *4*	2+		6500	100 *30*			
38AR	10988.0 *7*	(2,3-)	< 0.2 keV	6507.4	2.3			
38AR	11066.1 *7*	(1+,2,3-)	< 0.2 keV	6500.1	11.1			
38AR	11068 *10*	1-		6502	18			
38AR	11214.7 *7*	(1-,2+)	< 0.2 keV	6504.4	11.4			
38AR	11373.6 *8*	(0-:4+)	< 0.2 keV	6496.0	100			
39K	6501 *2*	(3/2,5/2)+	59 fs *21*	6499 *2*				
44CA	6507.1 *5*	1	4.8 fs	6506.6 *5*	100			
44TI	8960 *3*	2+		6505	22 *2*			
48TI	7483 *5*	LE 4		6500	100			
49V	8912.2 *21*	(5/2)		6504	5			
52CR	6495.5 *5*	1	0.131 eV *9*	6495.1 *5*	100			
53MN	8784.1 *3*	(3/2-,5/2,7/2-)		6510	14			
53MN	9193.3 *3*	9/2+		6507	7			
53MN	9416.0 *3*	(3/2-)		6503	10			
55MN	9248.7 *3*			6496 *1*	19			
55MN	9531.54 *23*			6495 *1*	7			
55MN	9861.3 *5*			6510 *2*	24			
55MN	9942.05 *23*			6510 *1*	36			
57FE	7646.7 *7*	1/2-		6507.0 *10*	<1.0			
58FE	10044.31 *19*	1-		6506.0 *7*	58 *7*			
58CO	8610.0 *23*			6505	41 *5*			
61CU	6505.6 *5*	3/2		6505.1		D+Q	0.51 *6*	

Figure B.1: 6.5 MeV energies page 1/2.

61CU	8447.1 *5*	9/2+		6504	21	
63CU	8564.94 *22*	1/2-		6504	35	
75GE	6505.60 *5*	1/2+		6505.40 *11*	26.1 *14*	
71AS	7018.3 *15*			6508 *5*	32	
77SE	7418.868 *16*	1/2+		6507.02 *11*	2.70 *16*	
86RB	8651.0 *10*	2-,3-		6503.2 *7*	16 *4*	
124SN	6503.4 *6*	1	1.26 fs *20*	6503.2 *6*		D
133SB	6498.1 *3*			6497.9 *3*	100	
133SB	6505.6 *3*			6505.4 *3*	100	
141PR	7630.9 *10*	5/2+	0.090 eV *+40-10*	6502 *4*	17.7 *2*	
144ND	7817.4 *5*	(3-)		6502.68		
205TL	7646.15 *14*	1/2-		6505.1 *4*	6.2	
206PB	7311.2 *7*	1-		6509		
206PB	7975.7 *10*	1		6509		
208PB	6505.6 *22*	1	≤ 1.0 fs	6505.6 *22*		

Figure B.2: 6.5 MeV energies page 2/2.

Search parameters:
8945 <=E(γ1)<= 8955

Level and Gamma Information

More detailed information can be obtained by clicking on each NUCLEAR NAME

Nucleus	E_{level}(keV)	Jπ	$T_{1/2}$	E_γ(keV)	I_γ	γ mult.	γ mix. ratio	γ conv. coeff.
23NA	9396.39 *8*	7/2-		8954.5 *3*	25	E1+M2	+2.6 *7*	
27AL	8952 *1*	(5/2,9/2+)		8950.4 *11*	100			
30SI	8953.4 *5*	(1,2+)		8951.9 *5*	100 *6*			
31P	10212 *3*	(3/2,5/2+)		8945	100			
35CL	8955.0 *7*	3/2+	0.075 keV *15*	8953.8		(D+Q)	-0.39 *5*	
38AR	11123.0 *7*	3-		8954.2	100	D+Q	+0.11 *4*	
45SC	8961.2	1/2-	60 eV *10*	8948	100	[E1]		
45SC	8965.3	1/2-	31 eV *7*	8952	100	[E1]		
44TI	8954 *3*	1-		8953	8 *2*			
49V	9037.6 *21*	(5/2)		8946	100			
49V	9044.5 *21*	(7/2-)		8952	69			
53MN	8945.0 *3*	5/2,7/2-		8945	9			
53MN	8952.9 *3*	(5/2-,7/2-)		8953	62			
92MO	8955.5 *6*	1(-)		8955.0 *6*	100	(E1)		

Figure B.3: 8.95 MeV energies.

REFERENCES

[1] U. S. Customs and B. Protection, Cargo security and examinations, 2014.

[2] S. Fetter, V. A. Frolov, M. Miller, R. Mozley, O. Prilutsky, S. Rodionov, and R. Z. Sagdeev, "Detecting nuclear warheads," Science I& Global Security, vol. 1, no. 3-4, pp. 225–253, 1990.

[3] R. T. Kouzes, "Detecting nuclear warheads," Science I& Global Security, vol. 1, no. 3-4, pp. 225–253, 1990.

[4] R. C. Runkle, L. E. Smith, and A. J. Peurrung, "The photon haystack and emerging radiation detection technology," J. Appl. Phys., vol. 106, no. 4, 041101, 2009.

[5] R. C. Runkle, D. L. Chichester, and S. J. Thompson, "Rattling nucleons: new developments in active interrogation of special nuclear material," Nucl. Instrum. Meth. A, vol. 663, pp. 75–95, 2012.

[6] T. Taddeucci and R. Sheffield, "Neutron and gamma-ray production with low-energy beams," Los Alamos National Laboratory, Tech. Rep. LA-UR-07-2724, 2007.

[7] P. B. Rose, A. S. Erickson, M. Mayer, J. Nattress, and I. Jovanovic, "Uncovering special nuclear materials by low-energy nuclear reaction imaging," Sci. Rep., vol. 6, p. 24 388, 2016.

[8] R. C. Lanza, A. Erickson, J. Fisher, et al., "Nuclear reaction based monoenergetic gamma ray radiography system for detection of nuclear materials," in Nuclear Science Symposium and Medical Imaging Conference (NSS/MIC), 2014.

[9] J. Nattress, M. Mayer, A. Foster, A. B. Meddeb, C. Trivelpiece, Z. Ounaies, and I. Jovanovic, "Capture-gated spectroscopic measurements of monoenergetic neutrons with a composite scintillation detector," IEEE Trans. Nucl. Sci., vol. 63, no. 2, pp. 1227–1235, 2016.

[10] M. Mayer, J. Nattress, and I. Jovanovic, "Detection of special nuclear material from delayed neutron emission induced by a dual-particle monoenergetic source," Appl. Phys. Lett., vol. 108, no. 26, p. 264 102, 2016. eprint: http://dx.doi.org/10.1063/1.4955051.

[11] K. Wilhelm, J. Nattress, and I. Jovanovic, "Development and operation of a 6lif:zns(ag)scintillating plastic capture-gated detector," Nucl. Instrum. Meth. A, vol. 842, pp. 54 –61, 2017.

[12] P. E. Vanier, L. Forman, and D. R. Norman, "Thermal neutron imaging in an active interrogation environment," AIP Conf. Proc., vol. 1099, no. 1, pp. 583–586, 2009.

[13] Nai(tl) and polyscin nai(tl) sodium iodide.

[14] Saint-Gobain, Prelude 420 lyso, Online; accessed 18-December-2016.

[15] ——, Bgo bismuth germanate, Online; accessed 18-December-2016.

[16] ——, Csi(tl) thallium activated cesium iodide, Online; accessed 18-December-2016.

[17] ——, Brillance 380 lanthanum bromide labr3(ce), Online; accessed 18-December-2016.

[18] ——, Nai(tl) and polyscin nai(tl) sodium iodide, Online; accessed 18-December-2016.

[19] E. Technology, Neutron/gamma psd ej-301, ej-309, Online; accessed 18-December-2016.

[20] Saint-Gobain, Cdwo4 cadmium tungstate, Online; accessed 18-December-2016.

[21] E. Technology, Pulse shape discrimination ej-299-33a, ej-299-34, Online; accessed 18-December-2016.

[22] H. Kim, G. Cho, and H. Kim, "Characteristics of a stilbene scintillation crystal in a neutron spectrometer," Radiation Measurements, vol. 58, pp. 133 –137, 2013.

[23] X-ray imaging products: security detector datasheet.

[24] C. L. Melcher, R. A. Manente, and J. S. Schweitzer, "Applicability of barium fluoride and cadmium tungstate scintillators for well logging," IEEE Trans. Nucl. Sci, vol. 36, no. 1, pp. 1188–1192, 1989.

[25] P. Rose Jr and A. Erickson, "Calibration of cherenkov detectors for monoenergetic photon imaging in active interrogation applications," Nucl. Instrum. Meth. A, vol. 799, pp. 99–104, 2015.

[26] P. B. Rose Jr., "Cherenkov detectors for transmission studies of monoenergetic high-energy photons in active interrogation applications," Master's thesis, Georgia Institute of Technology, http://hdl.handle.net/1853/54464, 2015.

[27] P. Cherenkov, "Vidimoe svechenie chistykh zhidkostei pod deistviem gamma-radiatsii," Dokl. Akad. Nauk SSSR, vol. 2, p. 451, 1934.

[28] ——, "Visible radiation produced by electrons moving in a medium with velocities exceeding that of light," Phys. Rev, vol. 52, pp. 378–379, 1937.

[29] B. Sowerby, "Cerenkov detectors for low-energy gamma rays," Nucl. Instrum. Meth., vol. 97, pp. 145–149, 1971.

[30] M. Berger, J. Hubbell, S. Seltzer, J. Chang, J. Coursey, R. Sukumar, D. Zucker, and K. Olsen, "Xcom: photon cross section database (version 1.5).," National Institute of Standards and Technology, Gaithersburg, MD., Tech. Rep., 2010.

[31] Momentive, Ge-214 high purity quartz data sheet, Online; accessed 18-December-2016.

[32] Schott, N-sf57 data sheet 847238.353, Online; accessed 18-December-2016.

[33] P. Baesso, D. Cussans, C. Thomay, and J. Velthuis, "Toward a rpc-based muon tomography system for cargo containers.," Journal of Instrumentation, vol. 9, no. 10, p. C10041, 2014.

[34] B. J. Quiter, S. G. Prussin, B. Pohl, J. Hall, J. Trebes, G. Stone, and M.-A. Descalle, "A method for high-resolution x-ray imaging of intermodal cargo containers for fissionable materials," J. Appl. Phys., vol. 103, no. 6, 064910, 2008.

[35] H. Yang and D. K. Wehe, "Detection of concealed special nuclear material using nuclear resonance fluorescence technique," in 2009 IEEE NSS, 2009, pp. 898–903.

[36] M. Johnson, C. Hagmann, J. Hall, D. McNabb, J. Kelley, C. Huibregtse, R. G. Kwan E. and, and A. Tonchev, "Searching for illicit materials using nuclear resonance fluorescence stimulated by narrow-band photon sources," Nucl. Instrum. Methods. B, vol. 285, pp. 72 –85, 2012.

[37] S. Banerjee, S. Chen, N. Powers, D. Haden, C. Liu, G. Golovin, J. Zhang, B. Zhao, S. Clarke, S. Pozzi, J. Silano, H. Karwowski, and D. Umstadter, "Compact source of narrowband and tunable x-rays for radiography," Nucl. Instrum. Methods. B, vol. 350, pp. 106 –111, 2015.

[38] S. Chen, N. D. Powers, I. Ghebregziabher, C. M. Maharjan, C. Liu, G. Golovin, S. Banerjee, J. Zhang, N. Cunningham, A. Moorti, S. Clarke, S. Pozzi, and

D. P. Umstadter, "Mev-energy x rays from inverse compton scattering with laser-wakefield accelerated electrons," Phys. Rev. Lett., vol. 110, p. 155 003, 15 2013.

[39] T. J. T. Kwan, R. E. Morgado, T.-S. F. Wang, B. Vodolaga, V Terekhin, L. M. Onischenko, S. B. Vorozhtsov, E. V. Samsonov, A. S. Vorozhtsov, Y. G. Alenitsky, E. E. Perpelkin, A. A. Glazov, D. L. Novikov, V. Parkhomchuk, V. Reva, V. Vostrikov, V. A. Mashinin, S. N. Fedotov, and S. A. Minayev, "The development of enabling technologies for producing active interrogation beams," Review of Scientific Instruments, vol. 81, no. 10, 103304, 2010.

[40] A. J. Antolak, B. L. Doyle, K. N. Leung, et al., "Active interrogation using low-energy nuclear reactions," in SPIE: Penetrating Radiation Systems and Applications VII, vol. 5923, 2005, pp. 1–9.

[41] R. W. Kavanagh and C. A. Barnes, "Boron plus deuteron reactions," Phys. Rev., vol. 112, pp. 503–511, 2 1958.

[42] H.-M. Kuan, P. R. Almond, G. Din, and T. Bonner, "The 15.1 mev gamma-ray excitation functions of the reactions b10(he3,p15.1)c12, b11(d,n15.1)cr12 and c13(he3,15.1)c12," Nuclear Physics, vol. 60, no. 3, pp. 509 –517, 1964.

[43] R. Finlay, C. Brient, D. Carter, A. Marcinkowski, S. Mellema, G. Randers-Pehrson, and J. Rapaport, "The ohio university beam swinger facility," Nucl. Instrum. Meth., vol. 198, no. 2, pp. 197 –206, 1982.

[44] R. Hamm, "Test report - factory acceptance tests," AccSys Technology Inc, Tech. Rep. PO C1877, 2005.

[45] S. Agostinelli, "Geant4–a simulation toolkit," Nucl. Instrum. Meth. A, vol. 506, pp. 250–303, 2003.

[46] J Allison et al., "Geant4 developments and applications," in IEEE Trans. Nucl. Sci., vol. 53, 2006, pp. 270–278.

[47] National nuclear data center.

[48] G. Fehrenbacher, R. Meckbach, and H. G. Paretzke, "Fast neutron detection with germanium detectors: computation of response functions for the 692 keV inelastic scattering peak," Nucl. Instrum. Meth. A, vol. 372, pp. 239–245, 1996.

[49] Nuclear data center at kaeri.

[50] J. L. Black, H. M. Kuan, W. Gruhle, M. Suffert, and G. L. Latshaw, "Reactions ^{12}C(α, n) ^{15}O and ^{12}C(α, p) ^{15}N," Nucl. Phys. A, vol. 115, pp. 683–696, 1968.

[51] R. D. Swift, "Mobile x-ray backscatter imaging system for inspection of vehicles," vol. 2936, 1997, pp. 124–132.

[52] S Kolkoori, N Wrobel, K Osterloh, U Zscherpel, and U Ewert, "Novel x-ray backscatter technique for detection of dangerous materials: application to aviation and port security," Journal of Instrumentation, vol. 8, no. 09, P09017, 2013.

[53] L. J. Schultz, G. S. Blanpied, K. N. Borozdin, A. M. Fraser, N. W. Hengartner, A. V. Klimenko, C. L. Morris, C. Orum, and M. J. Sossong, "Statistical reconstruction for cosmic ray muon tomography," IEEE Tran. Image Proc., vol. 16, no. 8, pp. 1985–1993, 2007.

[54] J. Hall, S. Asztalos, P. Biltoft, J. Church, M.-A. Descalle, T. Luu, D. Manatt, G. Mauger, E. Norman, D. Petersen, J. Pruet, S. Prussin, and D. Slaughter, "The nuclear car wash: neutron interrogation of cargo containers to detect hidden {snm}," Nucl. Instrum. Meth. B, vol. 261, no. 12, pp. 337 –340, 2007.

[55] P. B. Rose and A. S. Erickson, "Cherenkov detectors for spatial imaging applications using discrete-energy photons," J. Appl. Phys., vol. 120, no. 6, 064903, 2016.

[56] S. V. Naydenov, V. D. Ryzhikov, and C. F. Smith, "Direct reconstruction of the effective atomic number of materials by the method of multi energy radiography," Nucl. Instrum. Meth., vol. B215, pp. 552–560, 2004. arXiv: physics/0310118.

[57] G. F. Knoll, Radiation detection and measurement, 3rd ed. Wiley, 21010, ISBN: 9780470131480.

[58] D. Herbert, N. DAscenzo, N. Belcari, A. D. Guerra, F. Morsani, and V. Saveliev, "Study of sipm as a potential photodetector for scintillator readout," Nucl. Instrum. Meth. A, vol. 567, no. 1, pp. 356 –359, 2006.

[59] A. Fienberg, L. Alonzi, A. Anastasi, R. Bjorkquist, D. Cauz, R. Fatemi, C. Ferrari, A. Fioretti, A. Frankenthal, C. Gabbanini, L. Gibbons, K. Giovanetti, S. Goadhouse, W. Gohn, T. Gorringe, D. Hertzog, M. Iacovacci, P. Kammel, J. Kaspar, B. Kiburg, L. Li, S. Mastroianni, G. Pauletta, D. Peterson, D. Poani, M. Smith, D. Sweigart, V. Tishchenko, G. Venanzoni, T. V. Wechel, K. Wall, P. Winter, and K. Yai, "Studies of an array of pbf2 cherenkov crystals with large-area sipm readout," Nucl. Instrum. Meth. A, vol. 783, pp. 12 –21, 2015.

[60] S. Korpar, R. Dolenec, P. Krian, R. Pestotnik, and A. Stanovnik, "Study of {tof} {pet} using cherenkov light," Nucl. Instrum. Meth. A, vol. 654, no. 1, pp. 532 –538, 2011.

[61] S. Light, J-series high pde and timing resolution, tsv package datasheet, Online; accessed 18-December-2016.

[62] C. Bircher and Y. Shao, "Investigation of crystal surface finish and geometry on single {lyso} scintillator detector performance for depth-of-interaction measurement with silicon photomultipliers," Nucl. Instrum. Meth. A, vol. 693, pp. 236 –243, 2012.

[63] P. Fan, T. Ma, Q. Wei, R. Yao, Y. Liu, and S. Wang, "Choice of crystal surface finishing for a dual-ended readout depth-of-interaction (doi) detector," Phys. Med. Bio., vol. 61, no. 3, p. 1041, 2016.

[64] R. Slates, A. Chatziioannou, B. Fehlberg, T. Lee, and S. Cherry, "Chemical polishing of lso crystals to increase light output," IEEE Trans. Nucl. Sci., vol. 47, no. 3, pp. 1018–1023, 2000.